

74375

PB 180 677

TECHNICAL SUPPORT PACKAGE FOR TECH BRIEF 68-10534  
IMPROVED THERMAL TREATMENT OF ALUMINUM  
ALLOY 7075

National Aeronautics and Space Administration  
Washington, D. C.

# AMPTIAC

20000711 201

Reproduced From  
Best Available Copy

DEPARTMENT OF COMMERCE

TECHNICAL INFORMATION CLEARINGHOUSE

FOR SCIENCE AND TECHNOLOGY



# REPORT selection aids

*Pinpointing R & D reports for industry*

**Clearinghouse, Springfield, Va. 22151**

**U.S. GOVERNMENT RESEARCH AND DEVELOPMENT REPORTS (USGRDR)**--SEMI-MONTHLY JOURNAL ANNOUNCING R&D REPORTS. ANNUAL SUBSCRIPTION \$30.00 (\$37.50 FOREIGN MAILING). SINGLE COPY \$3.00.

**U.S. GOVERNMENT RESEARCH AND DEVELOPMENT REPORTS INDEX**--SEMI-MONTHLY INDEX TO U.S. GOVERNMENT RESEARCH AND DEVELOPMENT REPORTS. ANNUAL SUBSCRIPTION \$22.00 (\$27.50 FOREIGN MAILING). SINGLE COPY \$3.00.

**FAST ANNOUNCEMENT SERVICE**--SUMMARIES OF SELECTED R&D REPORTS COMPILED AND MAILED BY SUBJECT CATEGORIES. ANNUAL SUBSCRIPTION \$5.00, TWO YEARS: \$9.00, AND THREE YEARS: \$12.00. WRITE FOR AN APPLICATION FORM.

**DOCUMENT PRICES**--ALMOST ALL OF THE DOCUMENTS IN THE CLEARINGHOUSE COLLECTION ARE PRICED AT \$3.00 FOR PAPER COPIES AND 65 CENTS FOR COPIES IN MICROFICHE.

**COUPONS**--THE CLEARINGHOUSE PREPAID DOCUMENT COUPON SALES SYSTEM FOR PURCHASING PAPER COPIES AND MICROFICHE PROVIDES FASTER, MORE EFFICIENT SERVICE ON DOCUMENT REQUESTS. THE PREPAID COUPON IS A TABULATING CARD WITH A FACE VALUE OF THE PURCHASE PRICE OF A CLEARINGHOUSE DOCUMENT (\$3.00 PAPER COPY OR 65 CENTS MICROFICHE). IT IS YOUR METHOD OF PAYMENT, ORDER FORM, SHIPPING LABEL, AND RECEIPT OF SALE.

COUPONS FOR PAPER COPY (HC) DOCUMENTS ARE AVAILABLE AT \$3.00 EACH OR IN BOOKS OF 10 COUPONS FOR \$30.00. COUPONS FOR MICROFICHE COPIES OF CLEARINGHOUSE DOCUMENTS ARE AVAILABLE IN BOOKS OF 50 COUPONS FOR \$32.50. WRITE FOR A COUPON ORDER FORM.

PB 180677

TECHNOLOGY UTILIZATION

## TECHNICAL SUPPORT PACKAGE

for

TECH BRIEF 68-10534  
IMPROVED THERMAL TREATMENT OF  
ALUMINUM ALLOY 7075

NASA

## TECHNICAL SUPPORT PACKAGE

for

TECH BRIEF 68-10534  
IMPROVED THERMAL TREATMENT OF  
ALUMINUM ALLOY 7075

NASA

*Technology Utilization Division*  
OFFICE OF TECHNOLOGY UTILIZATION  
NATIONAL AERONAUTICS AND SPACE ADMINISTRATION  
Washington, D.C.

**DISTRIBUTION STATEMENT A**  
Approved for Public Release  
Distribution Unlimited

Reproduced by the  
CLEARINGHOUSE  
for Federal Scientific & Technical  
Information Springfield Va. 22151

NOTICE: This document was prepared under the sponsorship of the National Aeronautics and Space Administration. Neither the United States Government nor any person acting on behalf of the United States Government assumes any liability resulting from the use of the information contained in this document, or warrants that such use will be free from privately owned rights.

#### ABSTRACT

The mechanism of the stress corrosion cracking of high strength aluminum alloys has been investigated using electrochemical, mechanical, and electron microscopic techniques. Corrosion and stress corrosion experiments have been carried out in 1M NaCl buffered to pH 4.7 at 30°C, using the commercial alloys 7075 and 2219 and also relevant pure materials. The feasibility of detecting stress corrosion damage in fabricated aluminum alloy parts by nondestructive testing techniques has been investigated using ultrasonic surface waves (Rayleigh waves).

Although the importance of metallurgical treatment on the susceptibility of aluminum alloys to stress corrosion is well-known, the underlying reasons for this sensitivity are not completely understood. This relationship has been explored for both pure and commercial alloys using electron microscopy and mechanical tests.

True stress-true strain curves were obtained for the alloys 2219-T851 and -T37 and 7075-T6(51) and -T73. Measurements were made at two different strain rates to determine the activation volume for dislocation movement. It was concluded that for 7075-T6 dislocations are more highly entangled in the highly susceptible short transverse direction than in the rolling direction. For 7075-T73 (nonsusceptible) and for both tempers of 2219, the dislocations were relatively unentangled. The results for 7075 are consistent with our stress corrosion data in suggesting that the mechanical properties of this material, as a function of heat treatment, mainly determine its sensitivity to stress corrosion. For 2219, the role of dislocation movements is less important and this is reflected in its lack of sensitivity to precorrosion.

With pure alloys, electron microscopy has been used to study their age-hardening process and to examine the mode of mechanical deformation and of corrosive attack. For Al-4Cu, preferential corrosive intergranular attack occurs in all tempers, susceptible and nonsusceptible. This attack proceeds by dissolution of the Cu-depleted zone parallel with the boundary;

Technology Utilization Office • Marshall Space Flight Center  
Huntsville, Alabama 35812  
Phone 205-876-1514

*For Further Information Contact*

*For sale by the Clearinghouse for Federal Scientific and Technical Information  
Springfield, Virginia 22151 - CFSI 1 price \$2.00*

the  $\text{CuAl}_2$  particles are left behind. In Al-7.5 Zn - 2.4 Mg, the particles of  $\text{MgZn}_2$  are attacked first but since they are never continuously linked, no specifically grain boundary attack is evident. These results show that in neither case can the Dix theory of stress corrosion be applied.

Deformation of foils in the electron microscope indicates that age-hardened Al-Zn-Mg tends to cleave along grain boundaries, whereas age-hardened Al-Cu tears across the grains. These results emphasize the above conclusions on these alloy systems, based on the deformation of the commercial alloys. The conclusions are expanded in that for Al-Zn-Mg (7075), it is the local, grain boundary mechanical properties which are critically important.

The corrosion of Al, Al-Cu,  $\text{CuAl}_2$ , Al-Zn-Mg and  $\text{MgZn}_2$  has been studied in pH 4.7 solutions of  $\text{Cl}^-$  and  $\text{SO}_4^{=}$ . The polarization phenomena for the alloys and the mode of attack on them have been characterized.

In the Al-Cu system, the corrosion is determined both by the composition and by the heat treatment. The effect of Cu in general is to make dissolution harder. However, 2219-T37 is much less generally corrosion than 2219-T851 in  $\text{Cl}^-$  solutions, although their compositions are identical. The nonsusceptible -T851 temper showed only general attack, but the stress corrosion susceptible -T37 temper experienced intergranular attack. Similar effects were found for pure Al-4Cu alloys in that the heavily overaged material was more corrosion than less precipitated tempers. All Al-Cu materials corrode more easily in  $\text{Cl}^-$  than in  $\text{SO}_4^{=}$ , in line with their ease of stress corrosion in these alloys.

Observations support the Dix theory of stress corrosion in these alloys. For the pure ternary (Al-7.5 Zn-2.4 Mg), the ease of corrosion in  $\text{Cl}^-$  solutions decreases as we proceed from the solutionized to the maximum susceptibility to the overaged tempers. In all three forms, the dissolution occurs much more readily than that of 7075. In addition, in the overaged condition, a secondary passivation effect is observed at about -680 mV vs. NHE. In  $\text{SO}_4^{=}$  solutions, the overaged form of the

pure ternary is much more readily attacked than the solutionized form and both are more readily attacked than 7075 or pure Al. It is shown that the differences between the pure ternary and 7075 result from the presence of Cu in the latter. An explanation of the effects of aging and of Cu on the corrosion of pure ternary is presented. This involves the effects of incorporation of Mg and/or Zn and/or Cu in  $\text{Cl}^-$ -formed  $\text{Al}_2\text{O}_3$  films and  $\text{SO}_4^{=}$ -formed films.

In this alloy system, there are no significant differences in macroscopic mode of attack with temper; i. e. there is no evidence for preferential intergranular attack in stress corrosion susceptible tempers. Also, the ease of corrosion of MgZn is similar in  $\text{Cl}^-$  and  $\text{SO}_4^{=}$ , although SCC of the alloys occurs much more readily in the former. The Dix theory of SCC does not then appear applicable to this alloy system.

The stress corrosion of 7075, 2219 and appropriate pure alloys in pH 4.7  $\text{Cl}^-$  and  $\text{SO}_4^{=}$  solutions has been studied under galvanostatic forced corrosion conditions at 30°C.

Low currents are somewhat more efficient in causing stress corrosion than large currents. It is suggested that the galvanostatic method of testing could be used as an accelerated and reproducible stress corrosion test.

The failure time in stress corrosion is strongly influenced by mass transport in solution. This must be controlled by appropriate stirring conditions.

The mode of failure is quite different for Al-Zn-Mg and Al-Cu. For Al-Zn-Mg, failure is catastrophic. That is, the load decreases only slightly with time during constant strain stress corrosion and then suddenly drops to zero as a single crack propagates across the specimen.

For Al-Cu, the load falls in a step-wise manner during test. Experiments with large-grained Al-4Cu show that this is due to a single crack advancing periodically from grain boundary intersection to grain boundary intersection. The necessity for continuous loading throughout this periodic

failure process shows that the process is not a periodic electrochemical-mechanical (PEM) phenomenon. Rather, it is a periodic electrochemical-mechanical, mechanical (PEMM) phenomenon.

It is shown that stress must be continuously applied for failure in 2219. Most of the attack on 7075 does not require presence of stress, however. These phenomena were investigated by exploring the effects of pure corrosion on subsequent stress corrosion life. Such experiments led to the definition of a precorrosion susceptibility index (PSI):

$$\text{PSI} = \frac{d}{d - d(\text{time to failure after precorrosion})}$$

$d$  (time of precorrosion)

Where the PSI is zero, as in 2219-T37, precorrosion has no effect on subsequent stress corrosion. Where the PSI is one, as it is initially for 7075-T6(51), the failure process occurs equally efficiently in absence as in presence of stress.

These experiments yield the following information on the failure of Al-Zn-Mg:

(1) Greater than 80% of the normal time to failure has nothing to do with "stress corrosion" but is a pure corrosion effect. A true stress corrosion effect only accounts for 20% of the normal life in normal stress corrosion tests. Conclusions on the stress corrosion mechanism of 7075, based on normal times to failure, are not likely to be generally valid.

(2) Two stages are involved in crack propagation. The first is the longest and is purely electrochemical. The second involves the combined effects of chemical and stress factors. But even here new interrupted load experiments show that the stress need not be continuously applied.

(3) Overaging of 7075-T6 leads to enhanced "stress corrosion" life. In fact, it turns out that all of this improvement results from improvement in precorrosion susceptibility and that the pure stress corrosion life is shorter for overaged alloys. A new heat treatment procedure

is suggested which retains the strength of 7075-T6 but improves its over-all stress corrosion resistance by two orders of magnitude.

(4) Precathodization leads to subsequent protection in stress corrosion, probably due to solution pH fluctuations.

(5) Total failure time is longer in  $\text{SO}_4^{=}$  than in  $\text{Cl}^-$  solutions. It is not clear whether this results from a change in the precorrosion characteristics or a modification of the true stress corrosion process.

The effect of the stress level on the failure time of 7075 is much larger than that for 2219. This is consistent with the greater importance of dislocation motions and purely mechanical properties in the former case.

The feasibility of using ultrasonic surface waves for the non-destructive detection of (incipient) stress corrosion damage in fabricated aluminum alloy parts was investigated. Four MHz Rayleigh waves were generated on 7075 and 2219 surfaces. Studies were made of the surface attenuation of waves and of reflections from microcracks. Results for simulated defects, general corrosion and stress corrosion are reported. Stress corrosion cracks are uniquely detectable compared with artificial surface defects or with general corrosive attack. This unique detectability arises from the following observations:

(1) Reflections from microcracks are readily found with only small amounts of SCC, not at all with general galvanic corrosion (GGC) and only in special circumstances with artificial flaws. SCC microcracks can be distinguished from others by the unusual anisotropic character of their reflection coefficients.

(2) In attenuation, only SCC leads to significantly lower attenuation in circumstances where gross surface damage is not plainly visible.

For 7075, detection of SCC is more ready after a given period at higher stress levels. In all cases, detection is easier when the stress on the sample is maintained. For 7075 there is an incubation period before damage can be detected ultrasonically, but this is short and is less significant for SCC carried out at lower stress levels. Attenuation

increases monotonically for this alloy but apparently in a step-wise manner for 2219. There is only an insignificant incubation period for 2219.

Some experiments on the reproducible coupling of Rayleigh wave reflectors to the surface are reported.

## CONTENTS

	<u>Page No.</u>
ABSTRACT	i
LIST OF ILLUSTRATIONS	ix
SECTION A	
INTRODUCTION	1
SECTION B	
METALLURGICAL CHARACTERIZATION OF ALUMINUM ALLOYS	2
I. INTRODUCTION	2
II. REVIEW OF PREVIOUS WORK	2
A. General	2
B. Mechanical Tests	2
C. Electron Microscopy	3
D. Dissolution Mechanism	10
E. Scanning Electron Microscopy	10
III. PRESENT WORK	12
Summary	19
SECTION C	
CORROSION AND STRESS CORROSION OF ALUMINUM ALLOYS	22
I. INTRODUCTION	22
II. POLARIZATION CURVES	22
III. MODE OF CORROSION ATTACK	32
IV. SUMMARY OF CORROSION CHARACTERISTICS - RELATION TO STRESS CORROSION SUSCEPTIBILITY	37

## CONTENTS (Cont.)

	<u>Page No.</u>	<u>Figure No.</u>	<u>Page No.</u>	
<u>LIST OF ILLUSTRATIONS</u>				
			<u>Page No.</u>	
		<u>SECTION B</u>		
V.	STRESS CORROSION	44	B. 1	True stress - true plastic strain curves for 7075-T6 and 7075-T73.
A.	Introduction	44	B. 2	True stress - true plastic strain curves for 2219-T851 and 2219-T37.
B.	Review of Previous Work	44	B. 3	Electron micrographs of thin foils after corrosion. (a) Al-7.5 Zn-2.4 Mg. 37,000 X. (b) Al-4Cu. 100,000 X.
1.	Conditions	44	B. 4	Electron micrographs showing effect of precipitates on oxide formation. (a) In matrix. 37,000 X. (b) Along grain boundary. 14,000.
2.	Charge Required for Failure	45	B. 5	Deformation in vacuum of aged foils. (a) Al-7.5 Zn-2.4 Mg. (b) Al-4Cu.
3.	Stirring Rate	46	B. 6	Electron micrograph of aged Al-4Cu after dissolution. 250,000 X.
4.	Relaxation Rate	48	B. 7	Fracture surfaces of Al-7.5 Mg-2.4 Zn (a) aged 24 hours at 100°C (b) aged 72 hours at 100°C (c) aged 16 hours at 150°C. 1600 X.
5.	Failure Modes	48	B. 8	(a) Grain boundary in Al-7.5 Zn-2.4 Mg aged 72 hours at 100°C. 37,000 X. (b) Same grain boundary as in B. 1(a) but after corrosion in buffered 1M NaCl for 3 hours. 37,000 X.
6.	Precorrosion Susceptibility Studies	48	B. 9	(a) Corrosion patterns developed on Al-4Cu. 100,000 X. (b) Further evidence for specific pattern attack. 37,000 X.
7.	Effects of Heat-Treatment	55	B. 10	Geometry of corrosion pits in Al-Mg-Zn. 7,500 X.
C.	Present Work	57	B. 11	(a) Localized arrays of dislocations in Al-7.5 Zn-2.4 Mg. 37,000 X. (b) Stress relief at the head of a dislocation pile-up resulting from grain boundary cracking. 37,000 X.
<u>SECTION D</u>				
NONDESTRUCTIVE TESTING TECHNIQUES FOR THE DETECTION OF SURFACE FLAWS				
1.	INTRODUCTION	71		
2.	SCC INVESTIGATION	71		
A.	General	71		
B.	Surface Attenuation	71		
C.	General Galvanic Corrosion (GGC)	79		
D.	SCC Tests at 90% and 60% of The Yield Strength	81		
E.	Determination of SCC Life (Time-to-Failure)	89		
F.	Anisotropy of Rayleigh Wave Echoes from SCC	93		
G.	Reflectors and Detection of SCC in Finished Parts	95		
III.	INVESTIGATIONS OF SIMULATED DEFECTS WITH SURFACE RAYLEIGH WAVES	97		
IV.	SUMMARY	105		

LIST OF ILLUSTRATIONS (Cont.)

<u>Figure No.</u>	<u>Page No.</u>	<u>Figure No.</u>	<u>Page No.</u>
<u>SECTION C</u>			
C. 1	25	C. 12	51
Anodic current-voltage curves for Ternary system in pH 4.7 1.0M NaCl.		Typical load vs. time graphs for 7075-T6 and 2219-T37 during stress corrosion tests.	
C. 2	26	C. 13	54
Anodic Polarization curves for Al-Cu system in pH 4.7 1.0M NaCl.		Normalized time-to-failure vs. precorrosion time for 7075-T6 and 2219-T37.	
C. 3	27	C. 14	56
Anodic polarization curves for Ternary systems in pH 4.7 1.0M Na <sub>2</sub> SO <sub>4</sub> .		Normalized time-to-failure vs. precorrosion time for reheat-treated 7075-T6.	
C. 4	28	C. 15	58
Cathodic polarization curves for binary and Ternary systems in pH 4.7 1.0M NaCl.		Yield strength versus overaging treatment.	
C. 5	34	C. 16	59
Photomicrographs of (a) solutionized and (b) maximum susceptibility Al-4Cu alloys following anodic polarization at +50 mv to the respective open circuit potentials in pH 4.7 1.0M NaCl.		Time to failure versus overaging time for 7075.	
C. 6	35	C. 17	61
Photomicrographs of overaged Al-4Cu alloy following anodic polarization at +50 mv to the open circuit potential in pH 4.7 1.0M NaCl.		Normalized time-to-failure vs. precathodization time.	
C. 7	36	C. 18	63
i-t curves for pure Al-4Cu in pH 4.7 1.0M NaCl E applied = E open circuit + 50 mv.		Time-to-failure vs. Cl <sup>-</sup> concentration for 7075-T6. $j = 0.3 \text{ ma/cm}^2$ . Stress = 90% of yield stress. 1M Na <sub>2</sub> SO <sub>4</sub> .	
C. 8	38	C. 19	64
Photomicrographs of Ternary alloy (no Cu) in (a) solutionized and (b) overaged states following galvanostatic corrosion in pH 4.7 1.0M NaCl.		Time-to-failure vs. precorrosion time for 7075-T6.	
C. 9	39	C. 20	66
Photomicrographs of Ternary containing copper in (a) solutionized and (b) overaged status following galvanostatic corrosion in pH 4.7 1.0M NaCl.		Schematic load vs. time curves for (a) a standard precorrosion test and (b) an intermittent corrosion test.	
C. 10	47	<u>SECTION D</u>	
Time-to-failure versus stirring rate for 7075-T6 short transverse specimens. $j = 0.1 \text{ ma/cm}^2$ .		D. 1	74
C. 11	49	D. 2	75
Relaxation rate versus time during both cathodic protection and anodic corrosion.		Calibration curve relating the deflection of U-bend specimens to the applied stress on the outer fiber at the bend for 7075(T651). The curve illustrates the variability of plates A, B, and C.	
		Calibration curve relating the deflection of the U-bend specimens to the applied stress on the outer fiber at the bend for 2219(T37).	

LIST OF ILLUSTRATIONS (Cont.)

<u>Figure No.</u>	<u>SECTION D (Cont.)</u>	<u>Page No.</u>
D. 3	Ultrasonic attenuation due to GGC as a function of charge at 0.53 ma/cm <sup>2</sup> .	80
D. 4	Photomicrographs (300 X) of the surface condition of a 2219(T37) U-bend specimen illustrating the effect of GGC at 0.53 ma/cm <sup>2</sup> or 30 min and (b) 19.0 coul/cm <sup>2</sup> or 9.5 hours.	82
D. 5	Oscillograms illustrating the effect of GGC for 2219(T37) at 0.53 ma/cm <sup>2</sup> . (a) Reference oscillogram. (b) After 3.5 hours or 7.0 coulombs/cm <sup>2</sup> . (c) After 6.5 hours or 13.0 coulombs/cm <sup>2</sup> .	83
D. 6	Ultrasonic attenuation due to SCC and GGC as a function of charge at 0.52 ma/cm <sup>2</sup> .	84
D. 7	Ultrasonic attenuation due to SCC damage for 2219(T37) as a function of corrosion charge at 0.62 ma/cm <sup>2</sup> and 90% of the yield strength.	85
D. 8	Ultrasonic attenuation due to SCC damage for 2219(T37) as a function of corrosion charge at 0.57 ma/cm <sup>2</sup> and 60% of the yield strength.	86
D. 9	Oscillograms illustrating the effect of SCC for 2219(T37) at 60% of the yield strength and 0.53 ma/cm <sup>2</sup> . (a) Reference oscillogram. (b) After 0.1 coulomb/cm <sup>2</sup> at the stressed state.	88
D. 10	Determination of SCC life. Graph indicates the number of coulombs/cm <sup>2</sup> required for fracture of U-bend specimens as a function of current density.	91
D. 11	Anisotropy of Rayleigh wave echoes from SCC, GGC, and artificial defects as a function of probe angle.	94

LIST OF ILLUSTRATIONS (Cont.)

<u>Figure No.</u>	<u>SECTION D (Cont.)</u>	<u>Page No.</u>
D. 12	Effect of depth of artificial grooves on Rayleigh wave response.	98
D. 13	Reflection of Rayleigh waves from a groove as a function of the reciprocal of the depth.	99
D. 14	Effect of subsurface groove on Rayleigh wave response. The experimental procedure is also included.	101
D. 15	Effect of cylindrical holes with axes perpendicular to the surface on Rayleigh wave response as a function of hole diameter. The experimental procedure is also shown.	102
D. 16	Effect of cylindrical holes with axes perpendicular to the surface on Rayleigh waves as a function of hole depth. The experimental procedure is also shown.	103
D. 17	Effect of edge angle on Rayleigh waves. The experimental procedure is also shown.	104

SECTION A  
INTRODUCTION

The aims of this research program are to investigate the mechanism of stress corrosion cracking (SCC) of aluminum alloys and to examine non-destructive testing techniques for detecting SCC in fabricated parts.

For phase I (the mechanism study) we have concentrated on the commercial alloy systems 7075 and 2219, with ancillary work on pure alloys and phases. The approach has been to investigate in detail the physical and structural metallurgy of the materials and also their corrosion characteristics. This is being implemented by the following specific subprojects:

(1) Detailed studies of the corrosion of 2219 and 7075 and their relevant constituent phases, as well as appropriate pure alloys. Results are mainly presented in section C of this report, but some electron microscopy in this connection is described in section B.

(2) Correlation of microscopic metallurgy (physical structure, details of corrosion and deformation) with stress corrosion susceptibility. These studies have been done with pure alloys and are described in sections B and C.

(3) A quantitative study of the stress corrosion of commercial and pure alloys. These experiments are described in section C.

For phase II (the detection with nondestructive techniques of stress corrosion damage), studies have been made on 7075-T6 and 2219-T37. Four MHz Rayleigh waves have been used for this investigation. It has been shown that these waves are uniquely sensitive to stress corrosion, much more so than to other surface defects and to general corrosion. Results are presented in section D of this report.

For convenience of presentation, the figures are numbered consecutively within each section of this report, and the references are given as footnotes.

SECTION B

METALLURGICAL CHARACTERIZATION OF ALUMINUM ALLOYS

I. INTRODUCTION

A summary is given of the studies completed during the period June 1, 1967, to February 29, 1968. A detailed report of the work carried out during the quarter March 1, 1968, to May 31, 1968, is also presented.

II. REVIEW OF PREVIOUS WORK

A. General

Although the importance of metallurgical treatment and condition on the susceptibility of aluminum alloys is well-known, the underlying reasons for this sensitivity are not yet completely understood. It is the aim of the work in this section to provide metallurgical information which can be correlated with the results of stress corrosion tests. For commercial materials, the aim has been to correlate susceptibility with the dislocation structure determined from mechanical tests. For the high purity materials we have attempted to correlate attack with specific structures developed during aging and mechanical deformation.

B. Mechanical Tests

True-stress, true-strain curves were obtained for 2219-T851 and -T37, as well as for 7075-T6(51) and -T3. All mechanical tests have been made on standard tensile specimens cut from 1 1/2" thick plate. Specimens have been taken in both the short transverse and in the rolling directions. Two different strain rates,  $4.4 \times 10^{-3}$  and  $4.4 \times 10^{-2}$  inches per inch per minute were used. In order to insure high accuracy in the determination of strain, an extensometer

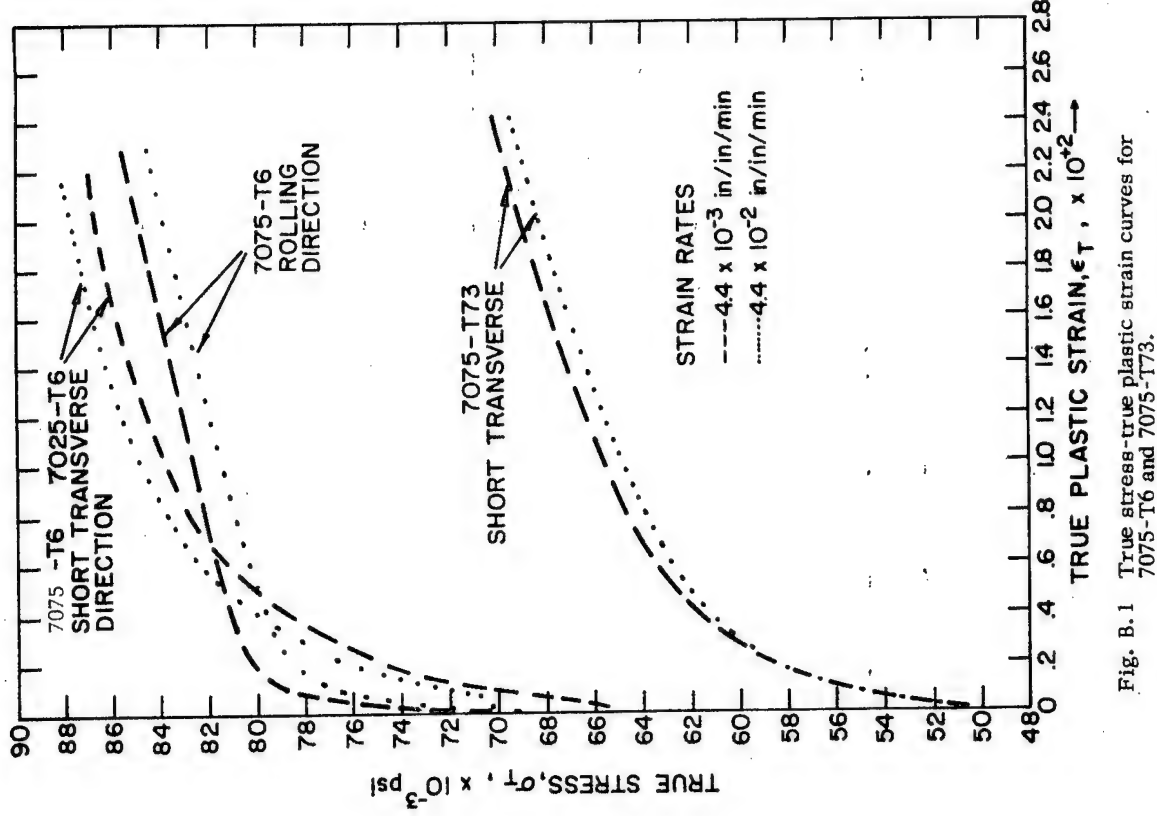


Fig. B.1 True stress-true plastic strain curves for 7075-T6 and 7075-T73.

was used rather than the cross-head position alone. The extensometer was calibrated using a micrometer to give an extension magnification of 500 to 1. The load was measured to  $\pm 0.5\%$ .

The results of these experiments are shown in Figs. B.1 and B.2, which show true-stress, true-strain curves for 7075-T6(51), 7075-T73, 2219-T851, and 2219-T37 short transverse specimens, as well as for 7075-T6(51), 2219-T851 and 2219-T37 rolling direction specimens. In each case these materials were tested at two different strain rates. From these data, noting the change in flow stress with change in strain rate, and remembering that for 7075 strain aging can occur, two conclusions can be drawn.

First, for 7075-T6(51), dislocations are more highly entangled in the short transverse than in the rolling direction. Second, for the -T73 temper of 7075 and for both tempers of 2219, the dislocations were found to be relatively unentangled.

The results for 7075 are in agreement with the known relative susceptibilities of the rolling and the short transverse directions. For 2219 these results would indicate that the mechanical state of this alloy is not as relevant to stress corrosion as it is for 7075. This conclusion is in agreement with results discussed in section C which show that the high purity analogue of 7075 tends to crack along grain boundaries even in the absence of a corroding medium, hence indicating the strong role played by purely mechanical considerations. The high purity analogue of 2219, on the other hand, shows no tendency towards such intergranular failure.

### C. Electron Microscopy

The electron microscopy investigation has focused on the detailed study of the mode of corrosion attack on foils of Al-7.5 Zn-2.4 Mg and Al-4Cu. Corrosion studies have been carried out in both buffered 1M NaCl and also 1M NaCl containing 1%  $H_2O_2$  by volume. These studies have led to several important conclusions concerning the manner in which attack occurs on these two alloys.

A major difference between the ternary and the binary alloys occurs in regard to the behavior of the precipitate particles. With Al-Zn-Mg, these precipitates are  $MgZn_2$ , while for Al-Cu they are  $CuAl_2$ . Our electrochemical measurements on the pure compounds, as described in the next section, show that  $MgZn_2$  is more active than the matrix, while  $CuAl_2$  is more noble. Hence, in the case of the ternary alloy the precipitate particles should dissolve preferentially in the binary alloy, however, the matrix will dissolve. These predictions have been verified by direct observation in the electron microscope where the preferential dissolution of the  $MgZn_2$  particles can be clearly seen. The stability of the  $CuAl_2$  particles is also evident from their continued existence even along grain boundaries which have cracked apart. Examples of photographs showing these results are given in Fig. B. 3.

Furthermore, the electron microscope investigation has shown the influence of precipitates on the effectiveness of the surface oxide layer in retarding corrosion. It was found that the oxide formed immediately above the grain boundary is very much less protective than that elsewhere on the alloy. That is, the oxide immediately above the grain boundary showed a strong tendency to fracture under circumstances when the oxide on other parts of the surface did not. This weakness of the oxide over the grain boundary is considered to be related to the grain boundary precipitates. This assumption is supported by the appearance of oxide over the matrix areas after corrosion. These areas showed symmetrically shaped patches, with symmetry corresponding to that of the particles in the matrix. These effects are shown in Fig. B. 4.

Deformation experiments in the mechanical stage of the microscope have illustrated the great difference in behavior between the ternary and the binary alloys. Figure B. 5 shows what happens when aged specimens of both alloys are strained in vacuum.

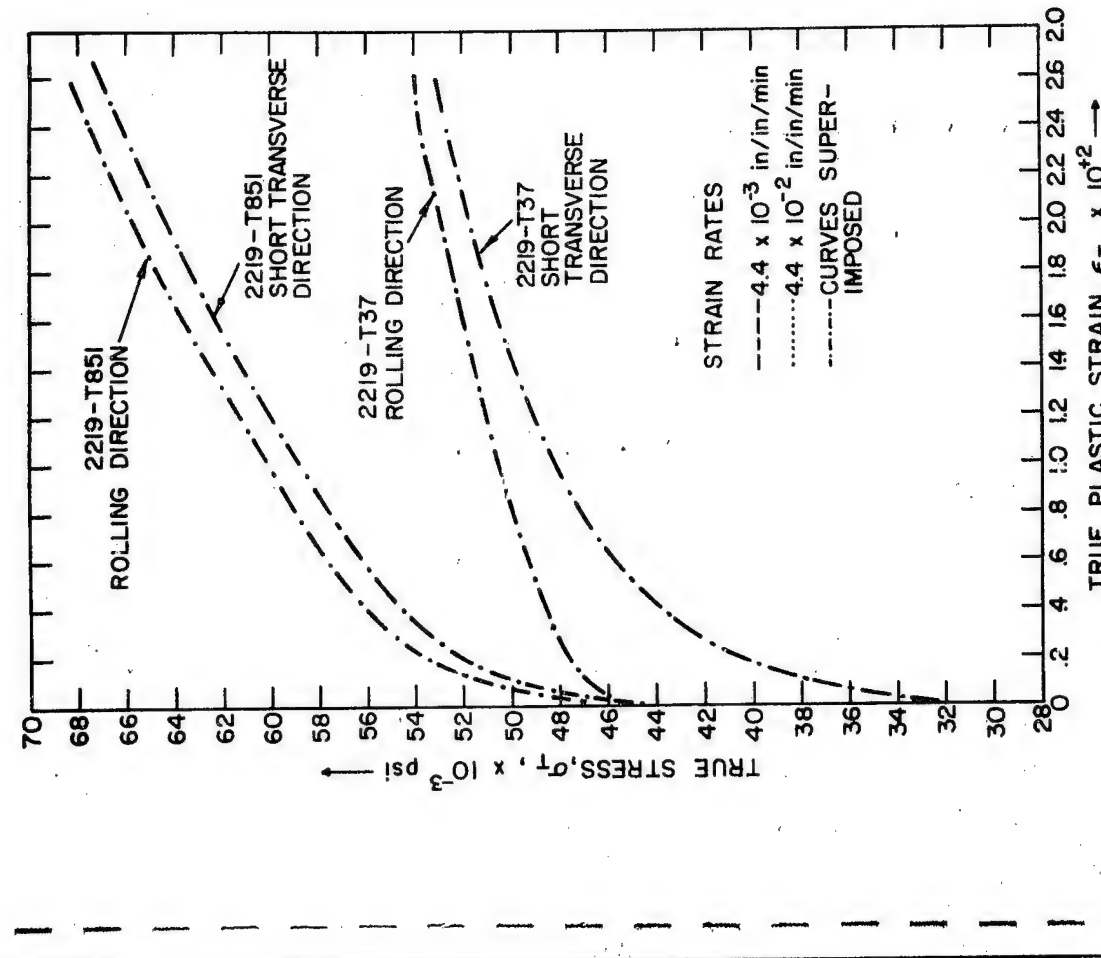


Fig. B.2 True stress-true plastic strain curves for 2219-T851 and 2219-T37.



(a)



(b)

Fig. B.3 Electron micrographs of thin foils after corrosion. (a) Al-7.5 Zn-2.4 Mg, 37,000X and (b) Al-4Cu, 100,000X.



(a)

Fig. B.4 Electron micrographs showing effect of precipitates on oxide formation: (a) in matrix, 37,000X and (b) along grain boundary, 14,000X.

The Al-Zn-Mg has, as can be seen, begun to fracture along grain boundaries. The Al-Cu, on the other hand, does not rupture along these boundaries.

#### D. Dissolution Mechanism

With regard to the actual mechanism of anodic dissolution, very high magnification (greater than 200,000 X) work on Al-Cu has given evidence of a tubular pitting mechanism as proposed by Pickering and Swann\*. In this mechanism, which was developed specifically for the case of an alloy consisting of one noble component and one much less noble component, the bottom of the pit is pure matrix material and is anodic to the noble metal rich cathode which has been formed around the mouth of the pit. Figure B. 6 is an electron micrograph showing such a structure. Further evidence for solute transport has been obtained by the detailed examination of grain boundary precipitate particles after particle dissolution. This examination has revealed a class of smaller precipitate particles which would not be expected to have been stable during the aging heat-treatment and must therefore have been formed during dissolution, most probably by a solution and redeposition mechanism.

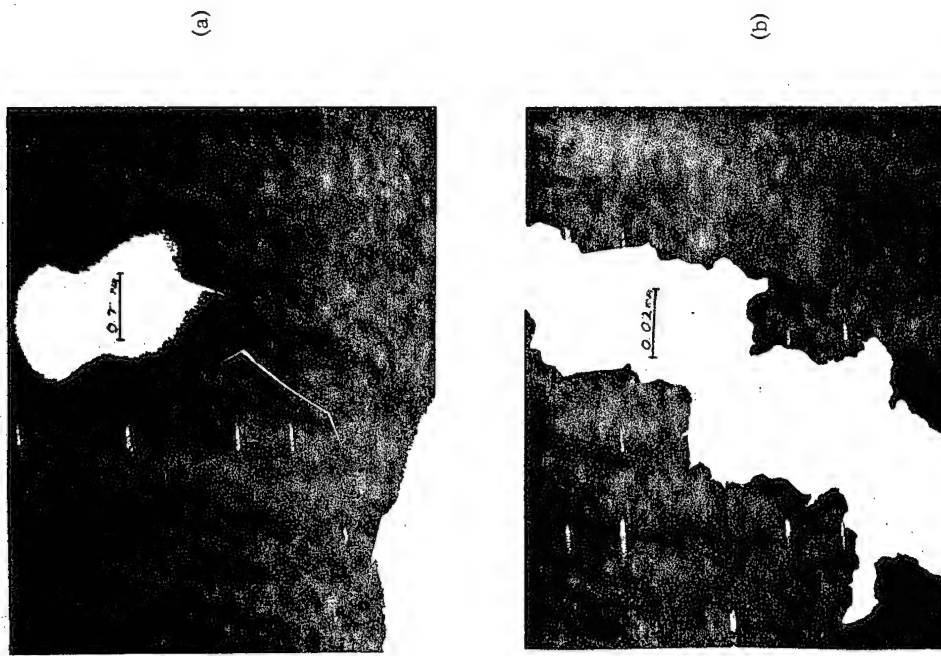


Fig. B. 5 Deformation in vacuum of aged foil:  
(a) Al-7.5Zn-2.4Mg and (b) Al-4Cu.

#### E. Scanning Electron Microscopy

A study using the scanning electron microscope was carried out on fracture surfaces of specimens of Al-7.5 Zn-2.4 Mg which were aged to bring them into the region of susceptibility by three varying degrees. These treatments were (1) heating for 24 hours at 100°C, (2) heating for 72 hours at 100°C, and (3) heating for 16 hours at 150°C.

In all cases the specimens were first put in the solutionized condition by heating at 480°C for 6 hours and were then water quenched. In this study photographs were obtained showing the change in marking

\*H. W. Pickering and P. R. Swann, *Corrosion* 19, 369t (1963).

form and type which occurred on going from treatment (1) to (2) to (3), Figs. B. 7 a, b, and c, respectively. In condition (2) in which the alloy is most susceptible, the striations were observed to be coarser than in either conditions (1) or (3). This finding is in agreement with the theories of Holl\* and of Speidel\*\* that maximum susceptibility should be associated with the appearance of planar arrays of dislocations.

These planar arrays would be expected to produce coarse striations on the fracture surface because they represent points of stress concentration when stress is applied to the sample and hence would perturb the advance of the crack front, i.e. at a dislocation pile-up. The crack would advance faster because of the higher stress concentration. Similarly, in between pile-ups, advance would be slower. These sudden changes in crack velocity would cause a concomitant change in plastic relaxation at the crack tip which would in turn lead to markings on the fracture surface.

### III. PRESENT WORK

The specimen of 2219-T37 supplied to us by MSFC, Huntsville, was analyzed for V, Ti, Cu, Mn, and Zr. The results of this analysis, together with the standard composition for 2219, is shown in Table B.I. From this table, it is evident that the material supplied lies within the standard composition ranges.



Fig. B. 6 Electron micrograph of aged Al-4Cu-after dissolution.  
250,000 X.

Our electron microscopy work continues to confirm that in the Al-Zn-Mg system, the  $MgZn_2$  precipitate particles dissolve first. Figure B. 8(a) shows a grain boundary in Al-7.5 Zn-2.4 Mg after solutionization at 480°C, followed by water quenching and aging for 89 hours at 199°C. This photograph is a very good example of the precipitate structure developed in this alloy, especially with regard to precipitates at the grain boundary. Figure B. 8(b) shows the appearance of the boundary after exposure for three hours in 1M NaCl

\* H. A. Holl, Corrosion 23, 173 (1967).

\*\* M. O. Speidel, Ohio State Conference on Stress Corrosion, Columbus, Ohio, September 11-15, 1967.

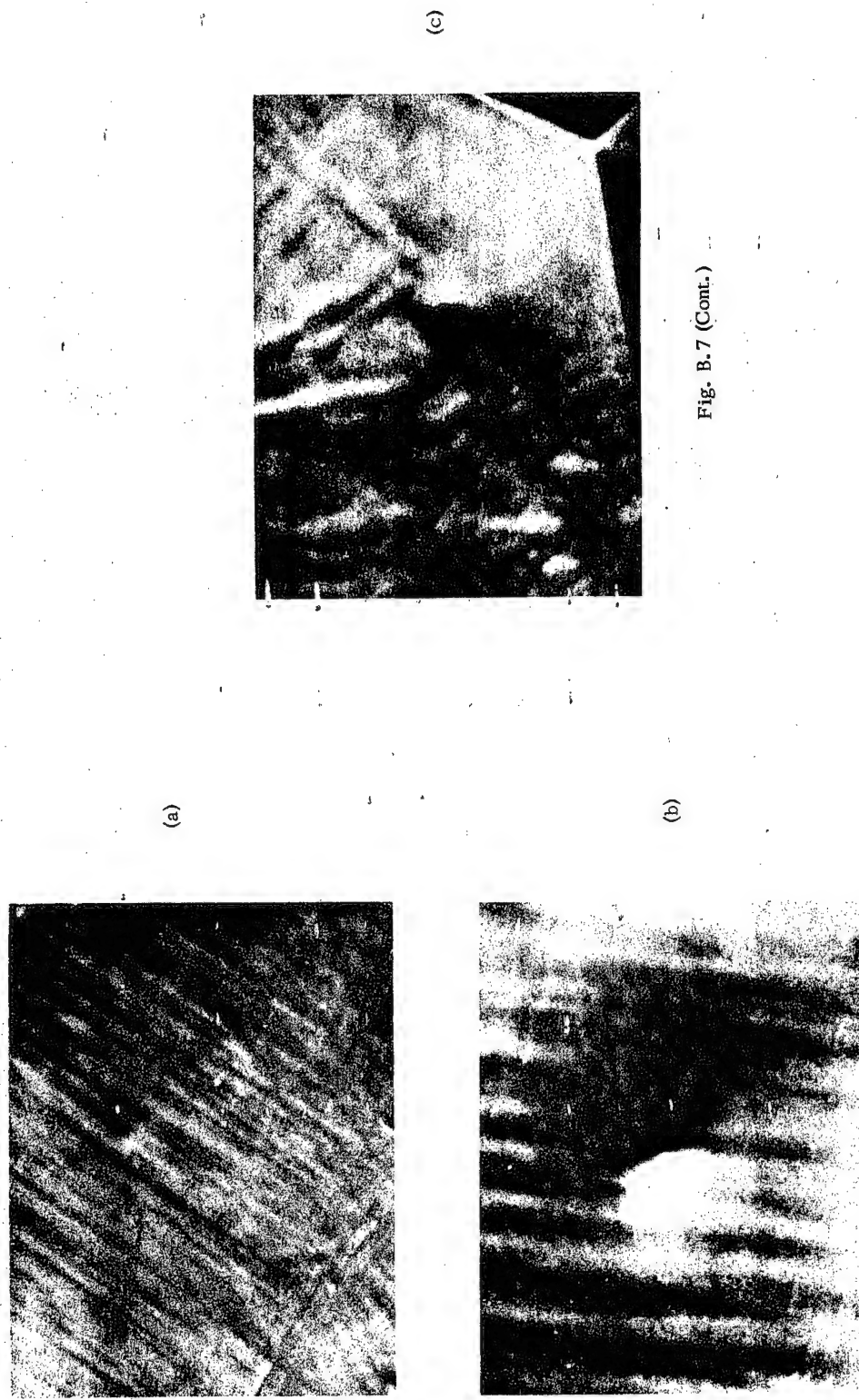


Fig. B.7. Fracture surfaces of Al-7.5 Mg-2.4 Zn (a) aged 24 hours at 100°C (b) aged 72 hours at 100°C (c) aged 16 hours at 150°C. 1600 X.

Fig. B.7 (Cont.)

buffered to pH 4.7. As can be seen, most of the precipitate particles have been leached out and a crack has developed along the boundary.

(a)



TABLE B.1

Analysis of 2217-T37 Sample From  
Marshall Space Flight Center

All Numbers in Weight Per Cent

Element	Cu	Mn	Ti	V	Zr
Standard 2219	5.8 - 6.8	.2 - .4	0.02-0.10	.05 - .15	.10 - .25
MSFC Specimen	6.12	.32	.021	.059	.17

(b)



Fig. B.8 (a) Grain boundary in Al-7.5 Zn-2.4 Mg aged 72 hours at 100°C, 37,000X and (b) same grain boundary as in Fig. B.1(a), but after corrosion in buffered 1M NaCl for 3 hours. 37,000X

Figure B.9(a) shows the square pattern of attack that has been repeatedly found in aged Al-4Cu. This photograph shows also a fine background pattern indicative of a solution and redeposition mechanism. The apparent association of these square areas with precipitates should also be noted. This relationship is also shown in the lower magnification photograph of Fig. B.9(b). If attack is allowed to continue, these localized areas of attack lead eventually to complete perforation, as shown in Fig. B.10. It should be noted in this figure that the diagonals of all the square pits are parallel, indicating the crystallographic nature of the attack.

Initial experiments have been carried out on deformed foils of Al-7.5-Zn2.4 Mg. These foils were prepared in the usual way by solutionization at 480°C, followed by water quenching and aging at 100°C for 72 hours. This treatment is designed to bring them to



(a)



(b)

Fig. B. 9 (a) Corrosion patterns developed on Al-4Cu. 100,000 X.  
(b) Further evidence for specific pattern attack. 37,000 X.

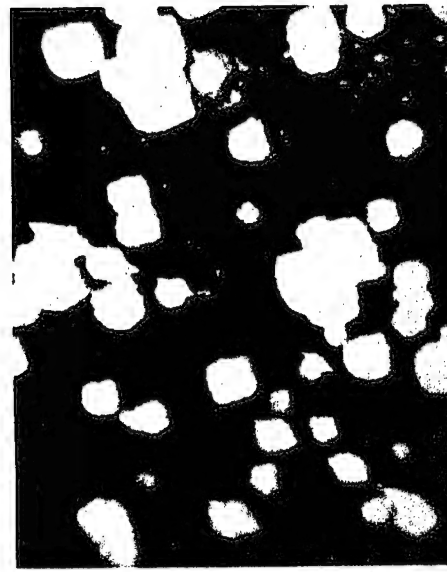


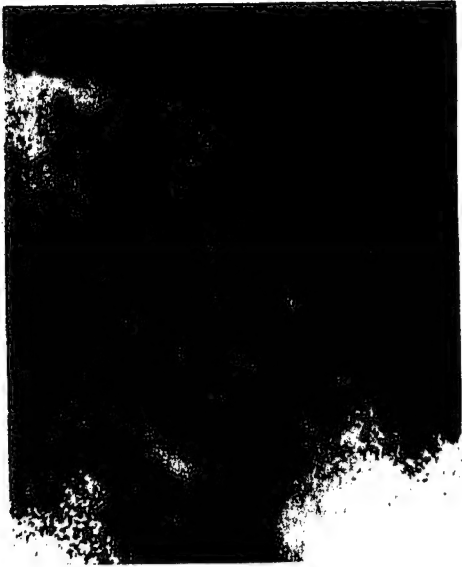
Fig. B. 10 Geometry of corrosion pits in Al-Mg-Zn, 7,500 X.

the susceptible state. After aging, the foils were deformed and examined in the electron microscope. Figure B. 11 shows the typical structure observed in such foils. In both Figs. B. 11(a) and B. 11(b) the dark bands lying at an angle to the grain boundary are localized dislocation pile-ups. In Fig. B. 11(b) the boundary has broken open and relieved the pile-up in the immediate vicinity of the boundary itself. These photographs confirm the hypothesis that such dislocation arrays do occur in susceptible ternary alloys. It is now planned to carry out observations of the way in which such dislocation arrays interact with the corrosion process. It is expected that such experiments will give added insight into the failure mechanisms of these alloys.

Summary. Our electron microscopy study has revealed several important facts about the corrosion and the failure processes which occur in Al-Cu and in Al-Zn-Mg.

First, we have shown that in Al-4Cu preferential attack at grain boundaries occurs in virtually all stages of hardening. Furthermore, at no stage of hardening is there a continuous grain boundary precipitate structure. The particles are always discrete. Thus, the suggestion by Thomas and Nutting \* that maximum susceptibility occurs when precipitates are present in continuous form is shown not to apply to the Al-Cu system. Conclusive evidence is given to support the proposal of Vermilyea \*\* that corrosion will occur most rapidly at defects where segregation has occurred (e. g. grain boundaries) and that oxide film ductility may be strongly influenced by precipitate particles.

It has also been demonstrated that the difference in the electrochemical stability of the two different precipitate phases,  $\text{CuAl}_2$  and  $\text{MgZn}_2$  controls the mode of attack in aged Al-4Cu and Al-7.5 Zn-2.4 Mg.



(a)



(b)

Fig. B. 11 (a) Localized arrays of dislocations in Al-7.5Zn-2.4Mg, 37,000 X. (b) Stress relief at the head of a dislocation pile-up resulting from grain boundary cracking, 37,000 X.

\* G. Thomas and J. Nutting, J. Inst. Metals 88, (1959-60).

\*\* D. A. Vermilyea, General Electric Research and Development Report No. 67-C-055.

Lastly, deformation studies of Al-4Cu and Al-7.5 Zn-2.4 Mg have demonstrated the relatively low grain boundary cleavage energy of the latter alloy, thus confirming the trend indicated by others\*.

Thus, from these studies a coherent picture is emerging of the way in which electrochemical and mechanical properties combine to give failure. It appears that in the ternary system, the mechanical properties are of overriding importance and are sensitized, as will appear in section C, by a pure corrosion attack. In the Al-Cu system, the mechanical properties are much less obviously important in determining stress corrosion susceptibility. However, even in the Al-Cu system, the results are not consistent with the Dix theory of stress corrosion\*\*.

## SECTION C

### CORROSION AND STRESS CORROSION OF ALUMINUM ALLOYS

#### I. INTRODUCTION

The main purpose of the corrosion portion of the over-all investigation of stress corrosion cracking in high strength aluminum alloys has been to characterize the electrochemical and corrosion behavior of all the materials involved in the systems of interest. This is considered to be of prime importance because stress corrosion is not a purely mechanical process but involves a complex interaction between mechanical and electrochemical factors. The initial stage, that involving formation of the critical crevice or notch from which the ultimate crack results, may be purely electrochemical. Indeed this is the case for 7075-T6. However, even when stress is required in the crack initiation phase, as in 2219-T37, the role of corrosion is essential and must be understood.

In marked contrast to the abundance of stress corrosion data on these systems in the literature, there is a very meager amount of reliable electrochemical data. It has, therefore, been deemed necessary to obtain this required data on all the components of the two systems of interest under well defined conditions. This has involved a variety of techniques: polarization curve determinations via the potentiostatic method, weight loss studies, and galvanostatic anodizations. These have been carried out at constant temperature (30°C), in an oxygen-free environment (hydrogen atmosphere), using high purity reagents.

In this section the results of the past contract year will be summarized. Some references to work obtained during the first year will be made when necessary.

#### II. POLARIZATION CURVES

The bulk of the work has involved determining the polarization behavior of the materials in both 1M NaCl and 1M Na<sub>2</sub>SO<sub>4</sub>, using the poten-

\* G. Blankenburgs and A. T. Thomas, Conf. on Electron Microscope in Metallurgy, Swansea, Wales, September 27-29, 1967.

\*\* E. H. Dix, Trans AIME 137, 11 (1940).

tiostatic method. In most cases, the cathodic as well as anodic polarization behavior has been characterized. Such measurements are complicated in the case of alloys because invariably one of the components is more active than the others. The preferential removal of this component simultaneously alters the composition of the material being investigated. This is the case in all of the materials studied, with the exception of the pure metals and the intermetallic phase MgZn<sub>2</sub>. In the latter, both Mg and Zn are very active and dissolve in the same ratio as present in the compound. In spite of difficulties associated with preferential removal of more active species from the alloy materials and hydrogen evolution during anodic polarization, reproducible data were obtainable. In all cases, polarization measurements commenced at the open circuit potential, and the applied potential adjusted in suitable increments—10 mv for anodic determinations in Cl<sup>-</sup>, 200 mv for anodic measurements in SO<sub>4</sub><sup>=</sup>, and 100 mv for cathodic measurements in Cl<sup>-</sup> and SO<sub>4</sub><sup>=</sup>. The open circuit potentials for these materials are included in Table C.1. The currents, especially in Cl<sup>-</sup>, were somewhat time dependent, but measurements were recorded within two minutes after each increment in potential, when most current levels were nearly steady.

The polarization data are summarized in Figs. C.1-C.4. The anodic curves for the Al-Cu system in pH 4.7 Cl<sup>-</sup> are presented in Fig. C.2; those for the Al-Zn-Mg system are shown in Fig. C.1. The anodic curves obtained in pH 4.7 SO<sub>4</sub><sup>=</sup> for both systems are given in Fig. C.3. Cathodic polarization curves for both systems in both media are to be seen in Fig. C.4.

It can be seen from Fig. C.2 that Al and Cu define the potential limits of the system—Al being the most active component and Cu the most noble. It is readily apparent that the position of the anodic curve for a given material is not related in a simple way to the quantity of copper present. The metallurgical state of the material seems to be of prime importance. This is easily seen by considering the relative positions of the -T851 and -T37 tempers of 2219 in Fig. C.2. Whereas

TABLE C.1  
Open Circuit Potentials in pH 4.7  
1.0M NaCl

Material	Open Circuit Potential (vs. NHE)
MgZn <sub>2</sub>	- 865 $\pm$ 5 mv
Al	- 680 $\pm$ 25
Pure Ternary: P.T.	
Solutionized, P.T. (S)	- 741 $\pm$ 1
Max. Susceptibility, P.T. (M.S.)	- 729 $\pm$ 3
Overaged, P.T. (O.A.)	- 722 $\pm$ 15
7075 -T651	- 570 $\pm$ 30
7075 -T73	- 528 $\pm$ 10
Ternary without Copper: T	
Solutionized, T (S)	- 760
Overaged, T (O.A.)	- 645
Ternary with Copper: T + Cu	
Solutionized, T + Cu (S)	- 586
Overaged, T + Cu (O.A.)	- 528
2219 -T851	- 485 $\pm$ 5
2219 -T37	- 410 $\pm$ 20
Pure Al-4Cu Alloy:	
Solutionized	- 440 $\pm$ 40
Max. Susceptibility	- 492 $\pm$ 2
Overaged	- 512 $\pm$ 12
CuAl <sub>2</sub>	- 395 $\pm$ 8

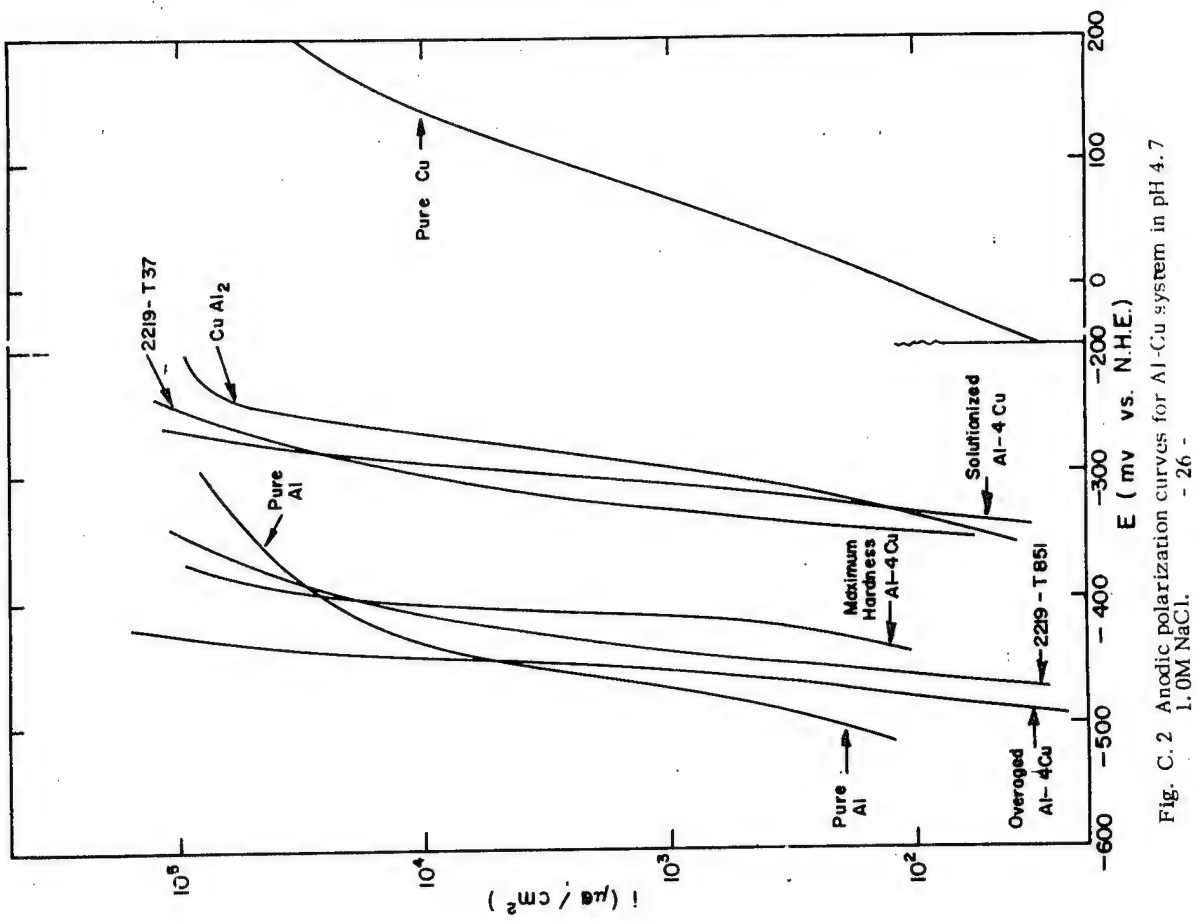


Fig. C.2 Anodic polarization curves for Al-Cu system in pH 4.7 1.0M NaCl

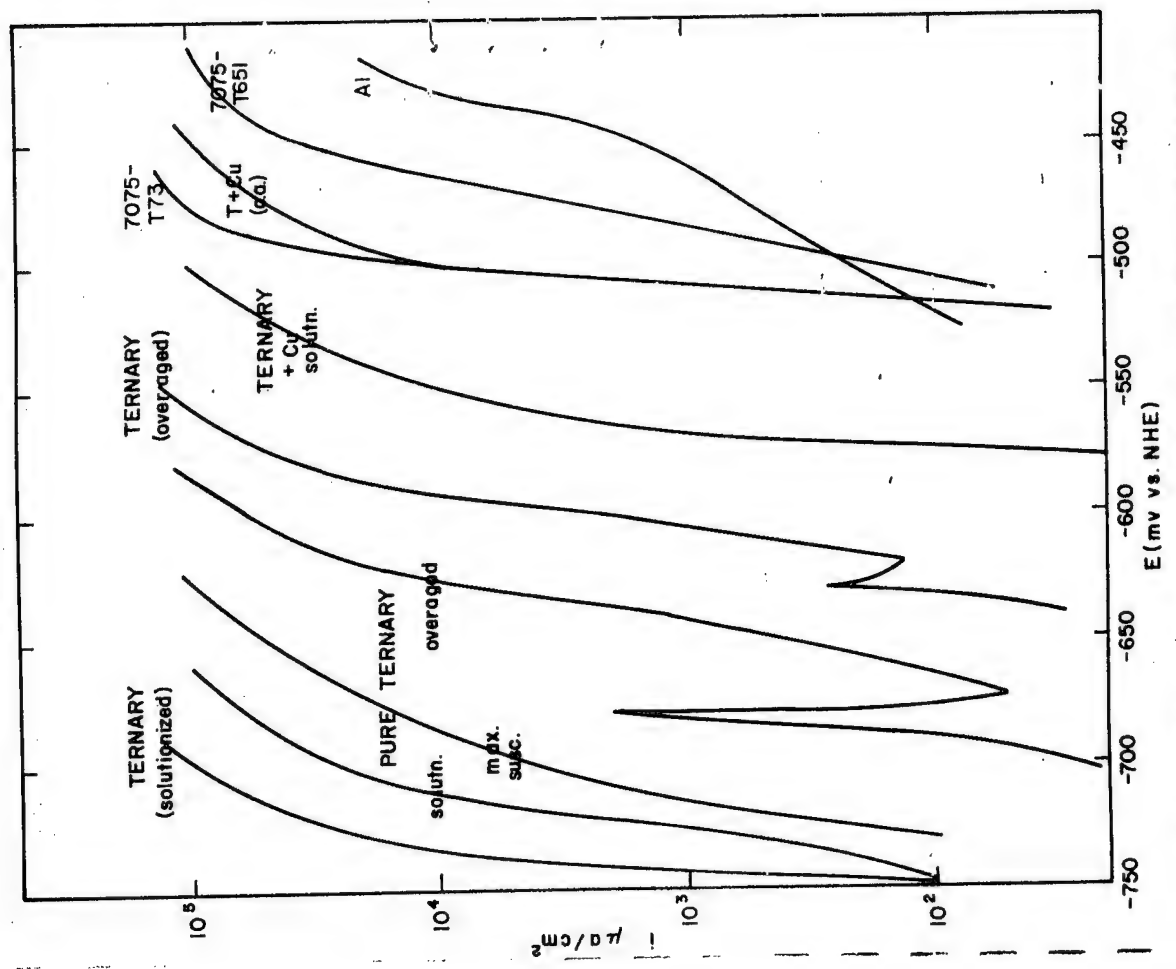


Fig. C.1 Anodic current-voltage curves for Ternary system in pH 4.7 1.0M NaCl

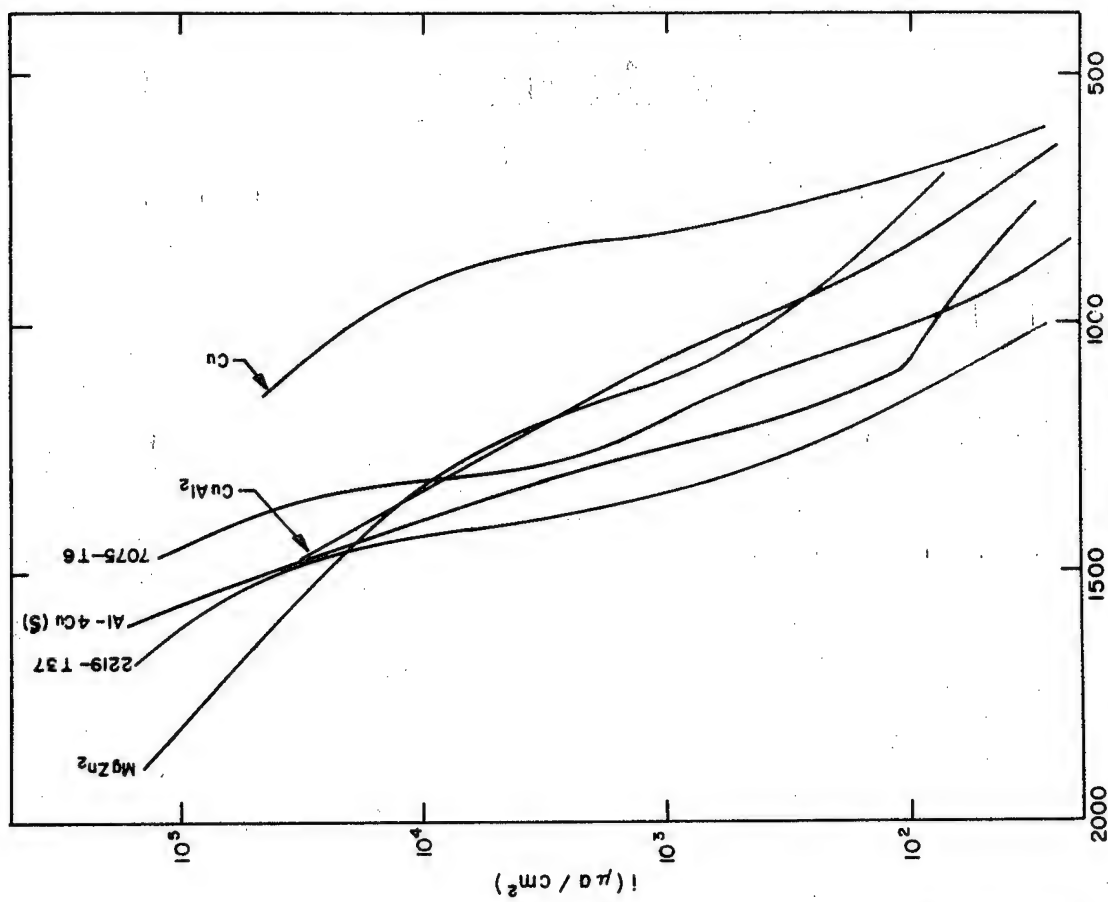


Fig. C.4 Cathodic polarization curves for binary and Ternary systems in pH 4.7 1.0M NaCl. - 28 -

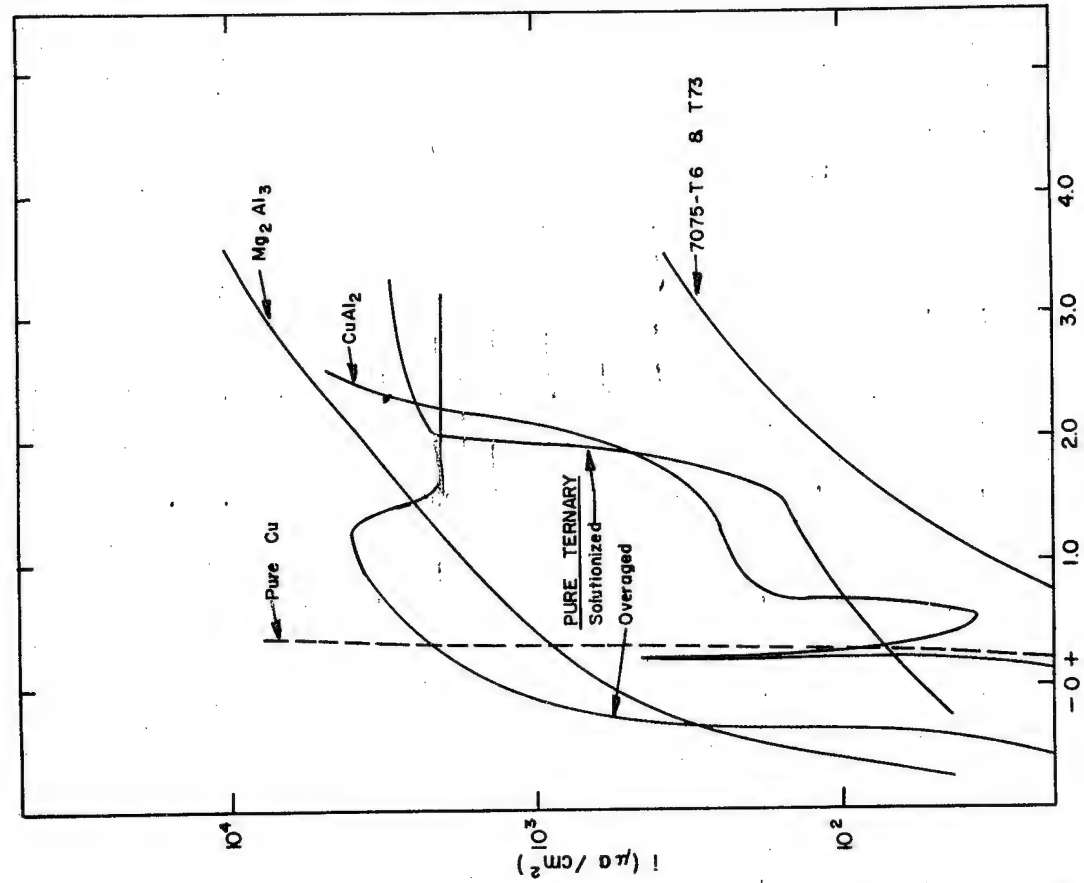


Fig. C.3 Anodic polarization curves for Ternary systems in pH 4.7 1.0M Na₂SO₄. - 27 -

they contain nearly identical amounts of Cu, the overaged -T851 is displaced ca. 100 mv more negative towards pure Al itself, whereas the -T37 temper lies very close to the curve for CuAl<sub>2</sub>. A similar trend can be seen in the curves for the pure binary alloy in the same figure. The overaged pure alloy curve is almost superimposed on that for pure Al, whereas that for the solutionized material occupies a position close to the CuAl<sub>2</sub> curve.

While it appears that Cu, homogeneously distributed through the Al matrix, exerts a pronounced effect on the anodic polarization curves, the magnitude of this effect is, again, not simply related to the amount of copper. This is brought out by the proximity of the curves for -T37 and CuAl<sub>2</sub>, even though the latter contains 14 times the quantity of copper. The considerably more noble position of the curve for pure Cu suggests that the maximum effects of composition on the polarization curves occur at low Cu levels.

In  $\text{SO}_4^{=}$ , there is essentially no difference between the anodic polarization behavior of either the commercial or pure binary alloy and pure Al. When present in larger amounts, copper does disrupt the passivating effect of the Al oxide to some degree. Thus in CuAl<sub>2</sub> the anodic polarization behavior differs markedly from that in Cl<sup>-</sup>. The sharp peak at ca +300 mv vs. NHE, which is very time dependent, is considered to be due to the dissolution of Cu. The removal of surface copper atoms during this anodization in  $\text{SO}_4^{=}$  evidently results in enrichment of the surface in Al. This Al is subsequently passivated at higher potentials, greatly retarding further Cu dissolution.

An extensive study of CuAl<sub>2</sub>, involving galvanostatic, potentiostatic, and linear voltage scan techniques had been carried out previously. These results were reported in the Fifth Quarterly Report (Figs. C. 1 to C. 10).

The anodic polarization curves for the ternary system in Fig. C. 1 reveal a marked dependence on both the nature of the secondary alloying constituents as well as the metallurgical state of the alloy. Two ternary systems, kindly supplied to us by Dr. D. O. Sprowls of Alcoa, have been

investigated. The first is a pure ternary alloy, containing Al, Zn, and Mg only, in the amounts indicated in Table C. II. This is referred to as the "pure ternary." The second consists of two alloys having compositions similar to that of 70/75, with the exception that one of them does not contain copper. This system is referred to as the "ternary," with or without copper. The limits of the system are defined by MgZn<sub>2</sub>, the most active component, and pure Cu, the most noble. Two tempers of 7075, -T73 and -T651, as well as two series of pure alloys, are included. The open circuit potentials for the series are consistent with the relative positions of the respective curves and have been listed in Table C. I. The compositions of the alloys are given in Table C. II.

It was found, as in the case of the binary Al-4Cu system, that solutionization shifts the polarization curve towards that of the minor alloying constituent. The curve for solutionized Al-4Cu is closer to that of Cu than is the curve for the overaged alloy. Likewise in the ternary system, the curves for the solutionized alloys lie closer to that for MgZn<sub>2</sub> than those for the corresponding overaged materials. The addition of Cu to the ternary drastically shifts the curves more noble, but does not alter their relative positions.

Characteristic of the overaged alloys not containing Cu is the presence of a secondary passivation phenomenon which appears to coincide with the formation of a thick white oxide film. The difference between the curve for the pure ternary and that for the ternary can be ascribed to either the trace alloying components (Cr, Ti, and Si) or, more likely, to the 0.01% copper. It was suggested in the previous discussion of the Al-4Cu system that the maximum change in curve position with Cu content occurs at low Cu concentrations. This would be supported by the observed difference between the pure ternary and ternary containing the 0.01% Cu. Not only does Cu (presumably) cause a shift in the polarization curves, but it also suppresses the secondary passivation effect. For the solutionized and maximum susceptibility forms of the ternary, addition of Cu has less effect and merely shifts the curves slightly in the noble direction.

The effect of Cu in suppressing the activating influence of Mg and Zn is demonstrated in sulfate media as well. Although the curves for the ternary with and without Cu are not available, the likely effect can be seen upon comparing the plots for 7075-T6 and -T73 with those for the pure ternary. In the case of the latter, heat treatment has a marked effect upon the subsequent anodic behavior, whereas no significant difference was found between the -T6 and -T73 tempers. In Fig. C, I, the effect of heat treatment on the curve separation decreases with increasing Cu content. On this basis, it would be expected that in  $\text{SO}_4^{2-}$  a detectable difference would be found between solutionized and overaged ternary containing Cu.

It can be seen from Fig. C, 4 that alloy composition has only a slight effect on the cathodic polarization behavior. In addition, the curves are almost independent of the nature of the anion. The hydrogen over-voltage is highest for pure Al, as evidenced by the very negative position of the curve, whereas it is lowest for pure Cu. With the exception of the Al curve, there are no distinguishing features. The sensitivity of the cathodic polarization behavior of aluminum to anion and to prior anodization was discussed in the first Annual Summary Report.

### III. MODE OF CORROSION ATTACK

The mode of attack in pH 4, 7, Cl<sup>-</sup> following corrosion at two current densities (constant charge) has been established for most of the materials. The two current densities employed were 21 ma/cm<sup>2</sup> for 50 or 100 sec. and 2.1 ma/cm<sup>2</sup> for 500 or 1000 sec. These experiments were done galvanostatically in order to have better control of the amount of attack than is readily possible in a potentiostatic experiment. The resulting photomicrographs for the 2219 and pure binary alloy systems were presented in the Fifth Quarterly Report (Figs. C, 14 to C, 20).

In the 2219 system, intergranular corrosion was conspicuous only in the -T37 temper and was accompanied by pitting. Following anodic polarization measurements, in which much larger amounts of

	Mg	Zn	Cu	Cr	Ti	Fe	Si	Mn	Zr	V	Pure Al-4 Cu
7075	2.5	5.6	1.6	0.25							
Pure Ternary	2.4	7.5									
Ternary + Copper	2.47	5.64	1.61	0.20	0.02	0.00	0.01				
Ternary (no copper)	2.49	5.68	0.01	0.19	0.02	0.00	0.01				
2219	6.2	0.21									
	0.32	0.023	0.059								

ALLOY COMPOSITIONS

TABLE C, II

charge were involved, -T37 specimens showed severe intergranular attack and much more extensive pitting. The -T851 alloy, on the other hand, showed no intergranular corrosion even on samples used for polarization curve determinations. Although the pit density was lower on the -T851 alloy than on the -T37, the discolored patches around the pits suggest considerable internal corrosion. The weight loss studies on 2219-T851 (First Annual Summary Report) clearly revealed that the bulk of the corrosion of this alloy occurs under the surface and extends both inwardly and laterally.

The lack of intergranular attack in the -T851 material, which is in an overaged condition, is not consistent with the results obtained on the pure binary alloys. The maximum susceptibility and overaged pure alloys both underwent visible grain boundary corrosion. It is difficult to say which of the two aged forms shows the greater grain boundary attack. The denuded zone is apparent in the maximum susceptibility form due to the much lower density of pits in this region adjacent to the grain boundaries. Neither this nor slip lines were visible in corroded overaged material. The denuded zone was far more conspicuous on specimens which had been corroded at constant potential during the current-time studies. Figures C. 5 and C. 6 are photomicrographs of the three pure binary alloys following corrosion in pH 4.7 Cl<sup>-</sup> at a potential 50 mv anodic to their respective open circuit potentials. The current-time plots can be seen in Fig. C. 7.

The corrosion morphology of the two 7075 tempers and the pure ternary system also were investigated by corroding them galvanostatically. The ternaries with and without Cu were not examined this way, but photomicrographs of these alloys after anodic polarization curve determinations are included here in this section.

The photomicrographs of 7075-T6 and -T73 following galvanostatic corrosion were presented in the Fifth Quarterly Report (Figs. C. 23 and C. 24). In either temper was there clear evidence of intergranular corrosion. Film formation was heavy on the -T6 temper, becoming heavier

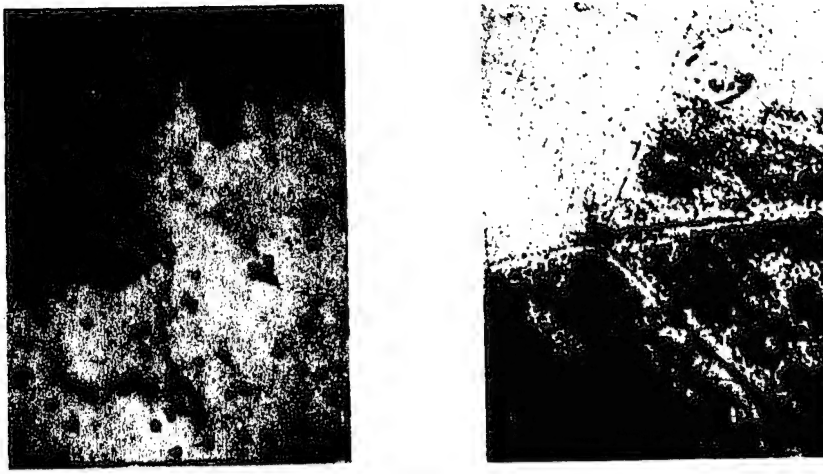


Fig. C. 5 Photomicrographs of (a) solutionized and (b) maximum susceptibility Al-4Cu alloys following anodic polarization at +50 mV to the respective open circuit potentials in pH 4.7 1.0M NaCl.

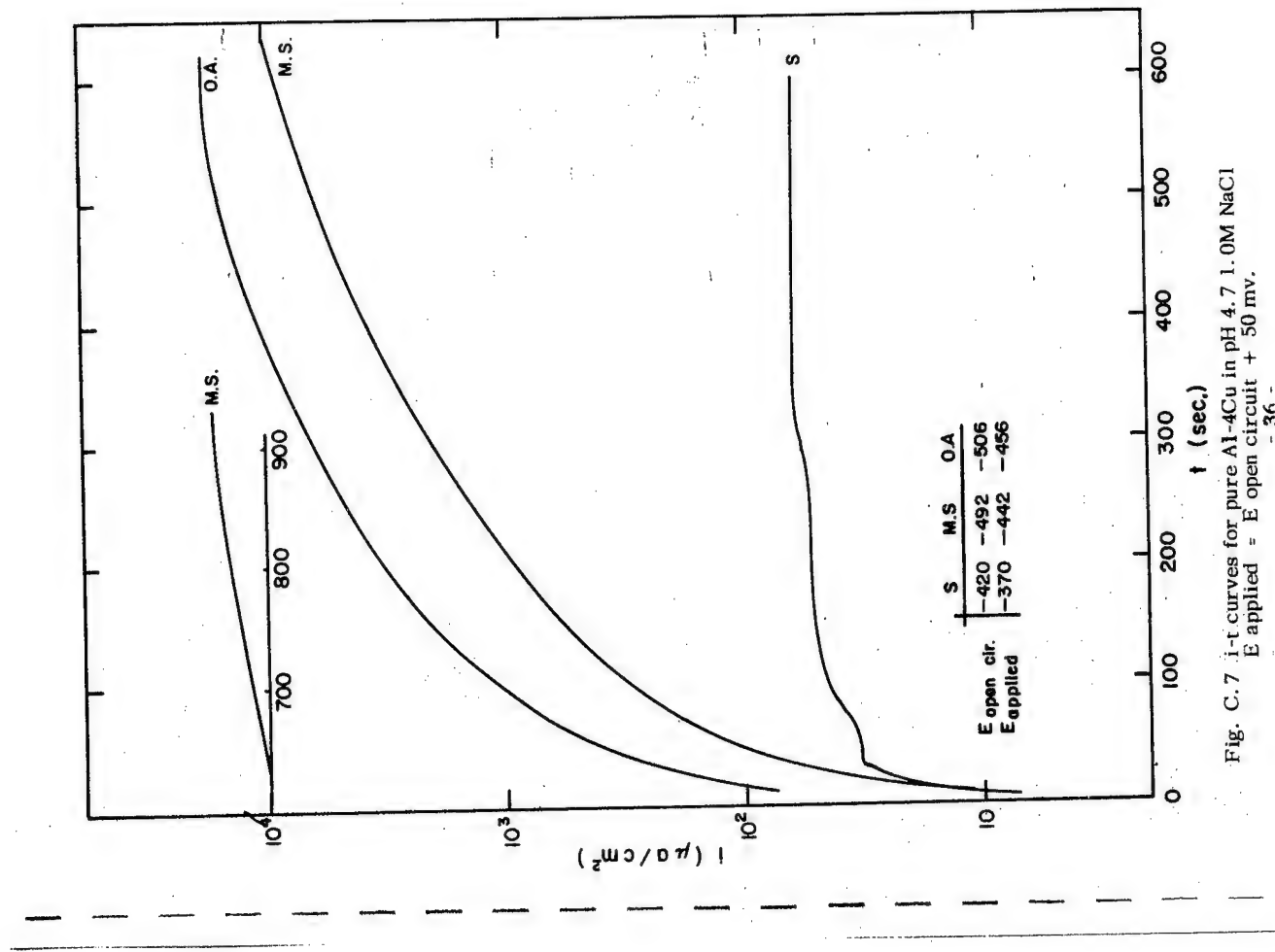


Fig. C.6 Photomicrographs of overaged Al-4Cu alloy following anodic polarization at + 50 mv to the open circuit potential in pH 4.7 1.0M NaCl.

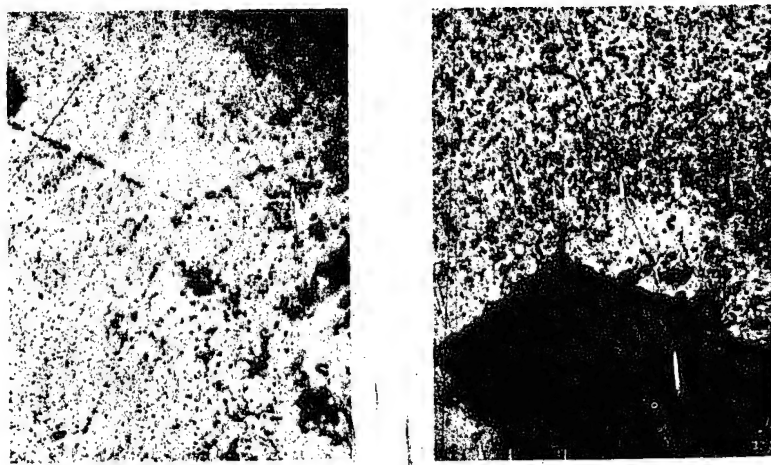


Fig. C.7  $i$ - $t$  curves for pure Al-4Cu in pH 4.7 1.0M NaCl  
 $E$  applied =  $E$  open circuit + 50 mv.

with increasing current density, but was almost entirely absent on the -T73. Although the film on the -T6 alloy tended to obscure surface features such as pits, it appears that pitting is more severe on the -T73 material.

The corresponding data on the pure alloy system was presented in the Sixth Quarterly Report (Figs. C. 5 - C. 9). Oxide formation was evident on all three forms of the pure alloy, but on the overaged form, grain boundaries could easily be seen. It is uncertain whether or not this involves preferred corrosion at the grains boundaries since it is only discontinuity in the oxide film which makes them visible (Fig. C. 8 and C. 9, Sixth Quarterly Report). Changes in the direction of striations in the film above the overaged material served to define the individual grains. Such was not the case with the maximum susceptibility form although, in this case, pits terminating at grain boundaries served to accentuate some of the grains (Fig. C. 6, Sixth Quarterly Report).

Entirely different modes of attack were observed in the ternary plus Cu. The ternary without Cu was similar to the pure ternary, as might be expected. This was especially the case in the solutionized condition (see Fig. C. 8). The ternary containing Cu showed a greater tendency to pit in the solutionized form and underwent intergranular corrosion (Fig. C. 9) when overaged.

#### IV. SUMMARY OF CORROSION CHARACTERISTICS - RELATION TO STRESS CORROSION SUSCEPTIBILITY

The heavy filming and secondary passivation phenomena observed only on alloys devoid of copper is particularly significant in regards to the nature of the effect of minor alloying constituents on the polarization and corrosion behavior of aluminum alloys. A further, more detailed discussion of this point is appropriate since it is intimately related to both the corrosion and stress corrosion behavior of aluminum alloys.

In the Fifth Quarterly Report, the effect of secondary alloyants such as Mg and Zn and Cu on the electrochemical behavior of the alloys



Fig. C. 8 Photomicrographs of Ternary alloy (no Cu) in (a) solutionized and (b) overaged states following galvanostatic corrosion in pH 4.7 1.0M NaCl.

was separated into a local oxide disruption effect and a general disruption effect. These will be discussed further in this section.

In summary, we have the following observations: Pure aluminum, which is covered by a protective film of aluminum oxide, dissolves transpassively in  $\text{Cl}^-$  because of interaction between the oxide and  $\text{Cl}^-$  ion. Since there is essentially no interaction between  $\text{SO}_4^{=}$  and aluminum oxide, the rate of dissolution is orders of magnitude lower in this medium. With Mg and Zn present, the dissolution rate is increased in both  $\text{SO}_4^{=}$  and  $\text{Cl}^-$ . With copper present, there is a trend in the opposite direction, i. e. the oxide is made more protective.

The over-all effect of alloying, when all three elements are present depends on the nature of the heat treatment. Indeed, the degree of change in the polarization and corrosion behavior from that of pure Al is more dependent on heat treatment than upon the quantity of Zn, Mg and/or Cu. There is strong evidence to suggest that extreme sensitivity to the quantity of Zn, Mg, and/or Cu occurs at very low alloying concentrations of these elements.

This behavior has been interpreted in terms of two distinct mechanisms. The first, which has been called the local disruption effect, pertains exclusively to the aged alloys where the bulk of the secondary alloys is present in the form of a second phase such as  $\text{CuAl}_2$  and  $\text{MgZn}_2$ . This hypothesis assumes that above such particles the alumina film will be either nonexistent or at least considerably weaker and more strained than above the Al-rich matrix. The oxide above the Al-rich matrix will be weakened in the vicinity of these particles. The degree of weakening will increase with the size of the particles and with their proximity to one another.

Where we have  $\text{MgZn}_2$  precipitates, which of course have no  $\text{Al}_2\text{O}_3$  film of their own, the result will be an enhancement in the over-all rate of dissolution of the alloy. This is especially true in  $\text{SO}_4^{=}$  since  $\text{MgZn}_2$ , unlike Al, dissolves with great ease in both  $\text{SO}_4^{=}$  and  $\text{Cl}^-$ . Experimentally, it is seen that the anodic current in  $\text{SO}_4^{=}$  for the overaged pure ternary is orders of magnitude greater than that for 70/75 and pure

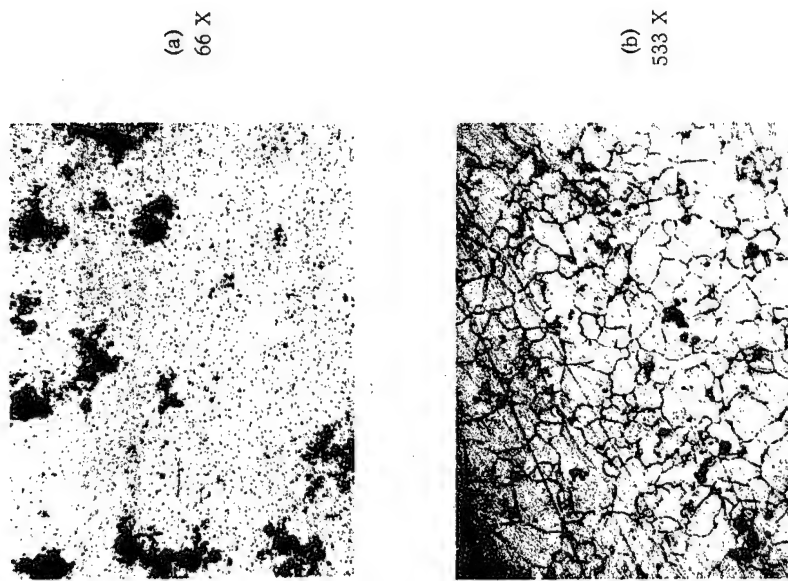


Fig. C.9 Photomicrographs of Ternary containing copper in (a) solutionized and (b) overaged states following galvanostatic corrosion in pH 4.7 1.0M NaCl.

Al and, initially, is also significantly greater than the anodic current for the solutionized pure ternary.

As seen from the polarization curves for  $\text{CuAl}_2$ , its dissolution rate is much lower in  $\text{SO}_4^{=}$  than in  $\text{Cl}^-$ , suggesting that a strong protective effect is exerted by the Al present. Thus, for the Al-Cu system, the local disruption effect would be expected to be of considerably less importance than for the Al-Zn-Mg system. Indeed, it is observed that the polarization behavior of the Al-Cu alloys does not differ significantly from that for pure Al in either  $\text{Cl}^-$  or  $\text{SO}_4^{=}$ .

The behavior of aged alloys containing all three alloyants — Mg, Zn, and Cu — seems at first glance to be at variance with the local disruption theory, but this need not necessarily be the case. These cases will be examined in terms of the general disruption effect.

The general disruption effect has been formulated to explain the changes produced in the polarization behavior of the solutionized alloys and also, to some extent, in aged forms of some of these materials. In general terms, it suggests that the secondary alloyants cause changes in the physical and chemical properties of the alumina film either through changes in ionic conductivity and/or in the structure of the oxide film as it forms in air after polishing and subsequently, in solution.

Referring to the anodic polarization curves obtained in  $\text{Cl}^-$  and  $\text{SO}_4^{=}$ , summarized in Figs. C. 1 and C. 2, it can be seen that the presence of Zn, Mg and Cu affect the corrodibility of Al to a degree seemingly out of proportion to the amounts present. In  $\text{Cl}^-$ , the potential difference between solutionized pure ternary and solutionized ternary plus copper amounts to more than 150 mv. In sulfate, the anodic current for solutionized pure ternary is orders of magnitude greater than the current for 7075 or pure aluminum.

In terms of the general disruption effect, copper modifies the oxide film above the solutionized alloys so as to increase its resistance to the passage of Al ions, whereas Mg and Zn have the reverse effect. When all three are present, the result depends on the metallurgical state,

probably grain size, and amounts of the elements.

It is certainly more difficult to characterize the exact nature of the general disruption effect. Is it due to a change in ionic conductivity, a change in the morphology of the film, or a varying combination of the two? There are difficulties associated with each theory. The ionic conductivity hypothesis is appealing, but has difficulties with regard to copper since at the potentials encountered in chloride media,  $\text{Cu(I)}$  or  $\text{Cu(II)}$  cannot exist.

Concerning the second alternative, while it is easy to visualize Cu, Mg and Zn atoms as altering the oxide nucleation and growth processes, it seems unlikely that the resulting polarization behavior could be so strongly affected, and in either direction at that. With regard to this hypothesis, however, it is significant to note again that heavy film-  
ing accompanying anodic dissolution in  $\text{Cl}^-$  is observed only on the copper-free alloys. Such an oxide is undoubtedly very porous, possessing none of the protective characteristics of the more compact invisible films formed in air and in  $\text{SO}_4^{=}$ . The 0.01% copper present in the "ternary without copper" is believed to be responsible for the partial suppression of the secondary passivation peak and filming. Thus, this second theory is somewhat more credible than the first, although changes in ionic conductivity must still be of considerable importance in the ternary system.

The main purpose of the corrosion investigation has been to relate the corrosion morphology to the stress corrosion susceptibility of the materials and to examine the Dix theory\* in the light of these results. Briefly, Dix's theory of stress corrosion cracking is purely electrochemical, requiring a nearly continuous path of corrodible material for susceptibility. This path can be the precipitate phase in the ternary system or the more anodic denuded zone adjacent to precipitate in the binary (Al-Cu) system.

\* E. H. Dix, Trans AIME 137, 11 (1940).

It has been shown that  $MgZn_2$  is very active in both  $Cl^-$  and  $SO_4^{=2-}$ . It can be concluded from this that anodic polarization of aged ternary alloys will result in dissolution of the exposed  $MgZn_2$  at the fastest rate possible. Even at open circuit, the exposed  $MgZn_2$  should dissolve within a short time. In  $Cl^-$ , under conditions of anodic polarization, the Al under the  $MgZn_2$  particles should be more reactive than the exposed matrix Al since corrosion can occur on an initially unfilmed surface. The process of crack propagation may well involve a repetitive two-stage process such as this. In  $SO_4^{=2-}$ , on the other hand, there will be negligible dissolution of the aluminum under the corroded  $MgZn_2$  particles. As a result, crack propagation will not be likely. Thus, the great corrosivity of  $MgZn_2$  is not in itself sufficient to produce stress corrosion susceptibility. This can be understood to be the case from our observation that 7075 is more susceptible to SCC in  $Cl^-$  than in  $SO_4^{=2-}$ , whereas  $MgZn_2$  corrodes equally well in both. Also, in 7075-T6, small changes in potential cause large changes in the lifetime; yet they cannot be having a significant effect on  $MgZn_2$  dissolution. If a continuous line or zone of  $MgZn_2$  existed through an alloy, cracking would be expected to occur in both  $SO_4^{=2-}$  and  $Cl^-$ . However, such a continuous line of precipitate, over any significant distance, never occurs. The Dix theory cannot be maintained, then, for this alloy system.

The binary alloys offer a somewhat different situation. The required continuous anodic path is more readily achieved because the denuded zone is the more anodic region.  $CuAl_2$  particles will, of course, dissolve, but only at fairly anodic potentials. Of the two commercial 2219 alloys studied, the nonsusceptible -T851 temper gave no evidence of intergranular corrosion, whereas the susceptible -T37 was found to have undergone severe grain boundary corrosion. At high magnification, the corroded grain boundaries appear to be continuous, and the particulate  $CuAl_2$  is visible. On the basis of the Dix theory, the stress corrosion susceptibility of the binary system should tend to increase with the degree

of aging. The results on 2219 are not consistent with this; the T851, which is in a highly aged condition, is nonsusceptible, whereas less aged -T37 is susceptible. It appears that this theory is in accord with the facts in correlating intergranular corrosion with stress corrosion susceptibility.

There is a contradiction between the results of the visible examination of corrosive attack and those in the electron microscopic study. We noted in the latter that all tempers of Al-4Cu are susceptible to intergranular corrosion, although the rate of trenching increases with aging. The light microscope reveals only very deep trenches. These results may in a sense be more relevant, since it may be necessary to have a deep trench for the Dix theory to be relevant. We should point out, however, that stress corrosion in this system requires the continuous application of stress during the whole process. (It is difficult to see how susceptibility to pure intergranular corrosion can then be the dominant factor.)

## V. STRESS CORROSION

### A. Introduction

An annual summary report is given of the studies completed during the period June 1, 1967, to February 29, 1968, which include the first measurements on the precorrosion effect. A detailed report is also given of the work carried out during the quarter March 1, 1968, to May 31, 1968.

### B. Review of Previous Work

#### 1. Conditions

All tests have been carried out under galvanostatic (constant current) conditions on specimens cut in the short transverse direction from

a 1 1/2 inch thick plate of 7075-T6(51) material. The mechanical property data obtained for this material have been given in the first Annual Summary Report. As before, the test solution was 1 molar NaCl buffered to a pH of 4.7 with sodium acetate and acetic acid. This solution was purged with nitrogen and thermostated at 30°C. Constant strain conditions were used throughout with the initial load set at 90% of the 0.2% offset yield strength.

## 2. Charge Requirements for Failure

Initially, tests were carried out to determine the effect of galvanostatic current density on the charge (in coulombs/cm<sup>2</sup>) which had to be passed before failure occurred. Current densities of between 0.1 and 20 ma/cm<sup>2</sup> were used. Over this range, the charge per unit area which is necessary to cause failure increased from 1.5 to 5 coulombs/cm<sup>2</sup>. Hence, it may be concluded that at the higher currents the corrosion reactions cannot proceed fast enough in localized regions to accommodate all the currents, and a higher percentage of the current is involved in general uniform corrosion attack.

At the lower currents, however, it is more possible to localize the corrosion reaction to pits and to crevices. Thus each unit of charge has a greater effectiveness in causing failure. Such a curve showing coulombs/cm<sup>2</sup> to failure versus applied corrosion current must, of course, go through the origin since if no current at all were applied the specimen would still fail finally through free corrosion. However, when plotting current on a linear scale, it is very easy to extrapolate the linear part of the curve to a positive intercept. Our interpretation of the value of this intercept is that it must represent the minimum amount of mass loss which must occur for failure to occur. For 7075-T651, this value is 1.35 coulombs/cm<sup>2</sup> or about  $1.35 \times 10^{-4}$  g/cm<sup>2</sup>. If such a mass loss were evenly distributed, it would amount to the removal of only about 2500 monolayers.

It is suggested that this procedure and the values of coulombs/cm<sup>2</sup> which this procedure produces might provide useful parameters for sorting quickly different materials with respect to their stress corrosion susceptibility. For example, 2219-T851 in similar tests absorbs 1100 coulombs before failing while 7075-T6(51) absorbs less than 1.5 coulombs/cm<sup>2</sup> under the same conditions before failure occurs. These tests have the very great advantage that they can be carried out relatively quickly compared with normal environmental exposure tests. In addition, solutions of practical interest could be utilized, with the impressed current only accelerating the naturally occurring reaction.

## 3. Stirring Rate

The time to failure has also been shown to be dependent on the rate at which the corrosion solution is circulated around the test specimen. This effect is most reasonably attributed to the sweeping away of corrosion products from the surface of the specimen. In particular, localized pH changes might still occur, in spite of buffering, in regions such as pits or corrosion crevices, and it is precisely these areas which would have the greatest effect on the failure time. By circulating fresh solution, these effects would be expected to be reduced. Anodic dissolution of aluminum removes OH<sup>-</sup> from solution, hence making the solution more acidic. Failure times decrease as acid concentrations increase, and conversely. Hence, increasing the stirring rate would be expected to increase the failure time because with greater stirring the buffer would be supplied in order to keep the pH constant.

This expected result is in fact observed, as shown in Fig. C.10, we have found the time to failure at 0.1 ma/cm<sup>2</sup> to increase by more than a factor of two as the flow rate was increased from 100 to 600 ml/minute. This effect, while relatively straightforward in interpretation, has generally not been taken into account in general stress corrosion testing. This may be the reason for some part of the very large scatter which is associated with these tests. In our own testing program the

observation of the above results has lead to the adoption of a standard condition of stirring for all tests. This is 220  $\text{mI}/\text{min}$  unless otherwise stated.

#### 4. Relaxation Rate

Because the load is monitored continuously during our tests, measurement of the relaxation rate, that is the change in load with time at constant strain, is automatically made. In the absence of stress corrosion, aluminum alloys at room temperature would still be expected to show relaxation under load but the presence of anodic dissolution would be expected to accelerate this effect markedly, and the increased rate of relaxation should give a measure of the extent of damaging attack. This conclusion is confirmed by the experiment shown in Fig. C. 11, which shows the relaxation rate versus time for a specimen of 7075-T6 under either cathodic protection or anodic dissolution. This figure shows that under cathodic protection the initial high relaxation rate after loading rapidly decays to a low value but that when the current is reversed so that anodic dissolution is occurring, the relaxation rate begins to increase. This data is presented here in order to demonstrate a novel method for determining whether or not a cathodic protection treatment is indeed preventing metal dissolution. Since this method does not require a measurement of the time to failure, it is inherently a more rapid method than those which do require such a measurement. As such, it could be of value in an accelerated testing program.

#### 5. Failure Modes

Continuous monitoring of the load during testing has revealed a substantial difference in the mode of failure of 2219-T37 compared with 7075-T651. This difference occurred in experiments where the alloys were kept at constant strain under loads which were initially 90% of

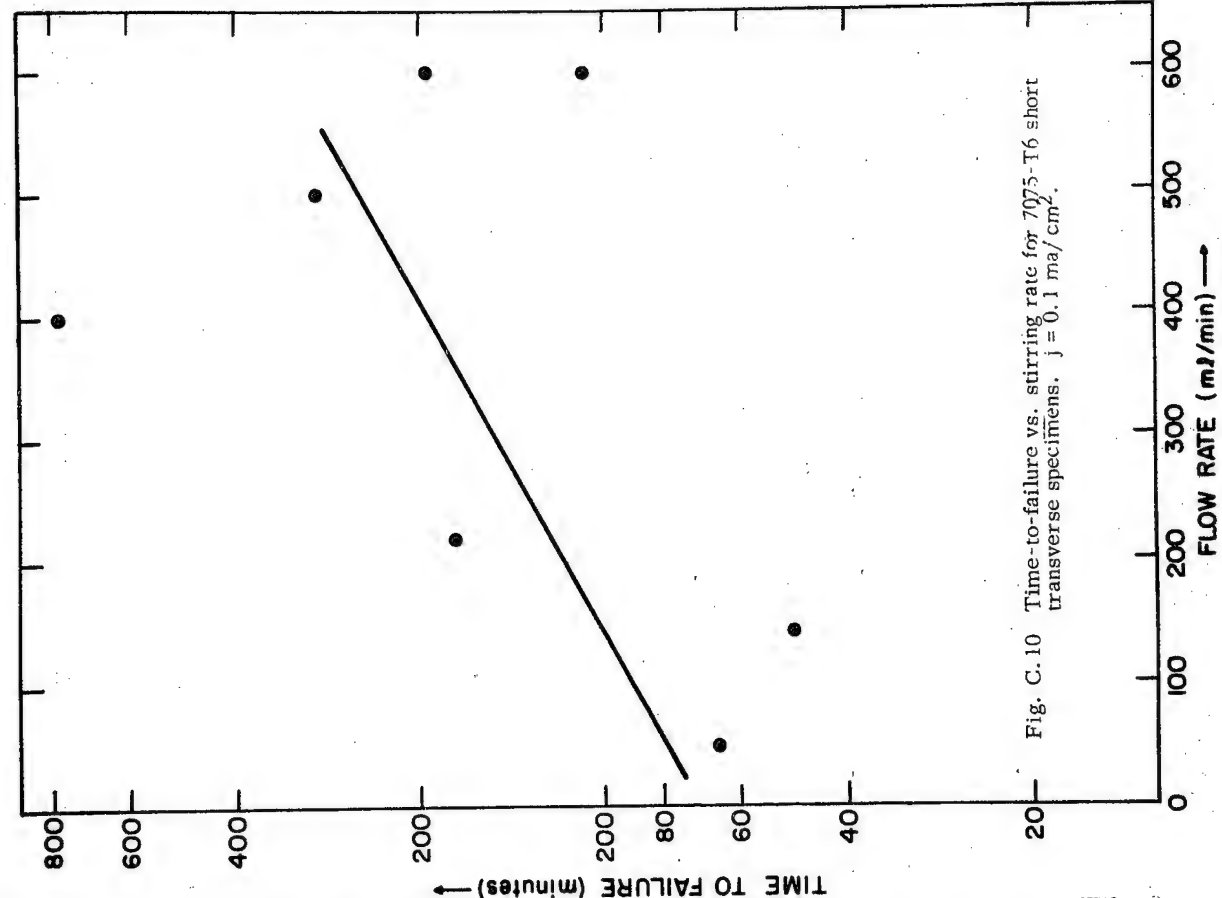


Fig. C.10 Time-to-failure vs. stirring rate for 7075-T6 short transverse specimens.  $j = 0.1 \text{ ma/cm}^2$

the 0.2% offset yield strength. In the case of 7075-T651, failure was catastrophic. That is, the load, after a period of only moderately changing with time, would drop suddenly to zero with the fracture propagating continuously across the specimen. These differences are shown in Fig. C. 12. This sudden failure is, in general, preceded only by a period amounting to 15-30 seconds during which the load would relax at an ever accelerating rate.

For 2219-T37 an entirely different behavior was observed. Instead of failing catastrophically, the specimens failed discontinuously in a step-wise manner. It is reasonable to associate that part of the step where the load does not fall off rapidly with the halting of crack advance at a grain boundary intersection.

This would be consistent with the observed microstructures of 7075-T651 and 2219-T37. In the case of 7075-T651, transverse sections show the grains to be severely elongated such that specimens strained in the short transverse direction will be stressed normal to these elongated grain boundaries. This will have the effect of providing very long regions of low cleavage energy (the grain boundaries) along which cracks can propagate. In the case of 2219-T37, however, the grain elongation is not as extreme as in the case of 7075-T651. Hence, even in the short transverse direction, the availability of grain boundaries oriented normal to the direction of stressing is not as large as in 7075-T651. In addition, the grain boundaries themselves are partly irregular due to the fact that the T37 temper is not a temper induced by precipitation heat-treatment. Rather it is a temper which is produced by mechanical treatment. Hence, a greater irregularity of grain boundaries is to be expected.

Furthermore, the grain boundaries in 2219 which are suitably oriented do not have as low a cleavage energy as those in 7075. This can be concluded from the fact that large grained samples of high purity Al-Mg-Zn fracture along grain boundaries while similar specimens at Al-Cu do not. In addition, since yield strength of 75,000 psi in 7075-T651, as opposed to 44,000 psi for 2219-T37, are found, the elastic energy

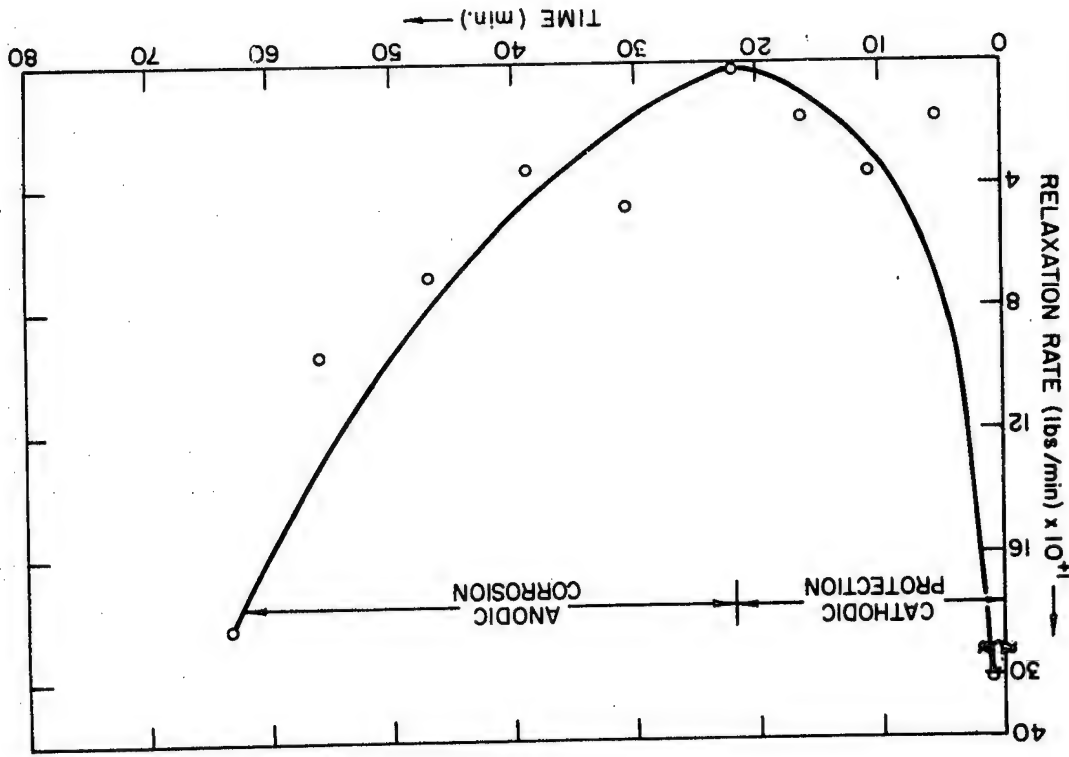


Fig. C. 11 Relaxation rate versus time during both cathodic protection and anodic corrosion for a specimen initially stressed in the same manner used for a stress corrosion test.

available for crack propagation is much greater in the former than in the latter. This fact, combined with the lower grain boundary cleavage energy and greater yield stress in the high strength alloys, serves to explain the differences in fracture modes satisfactorily.

Further proof that crack advance in the 2219-T37 alloys is associated with the halting of crack advance at grain boundary intersections was obtained by testing large grained specimens of Al-Cu. For these specimens, crack advance could be observed visually since the samples were in the form of strips 0.040" by 1/4" by 4" and the individual grains extended through the sample thickness. It was noted that load drop-offs coincided with sudden crack advance and that this periodic crack advance was associated identically with change in crack direction of a single crack as it advanced from grain boundary to grain boundary.

#### 6. Precorrosion Susceptibility Studies

It is always assumed that the phenomenon of stress corrosion means that the damage which occurs when stress and corrosion act together must exceed that which occurs when each acts separately. We have examined this requirement quantitatively and have found that under this definition a true stress corrosion process only operates for 20% of the time to failure of 7075-T6 as determined in a normal stress corrosion test. A "normal" stress corrosion test is one where both the corrosive environment and the stress are applied simultaneously. The type of test used to separate the effects of pure corrosion from stress corrosion represents, we believe, an entirely new form of corrosion testing procedure which could have wide application to a variety of materials other than aluminum alloys.

This procedure is as follows: First, the normal time to failure is determined by applying the load and the corrosive environment (or corrosion current) simultaneously. When this has been done, experiments are then carried out in which the specimen is corroded for varying lengths of time before the load is applied. The new time to failure is measured

Fig. C.12. Typical load vs. time graphs for 7075-T6 and 2219-T37 during stress corrosion load tests.

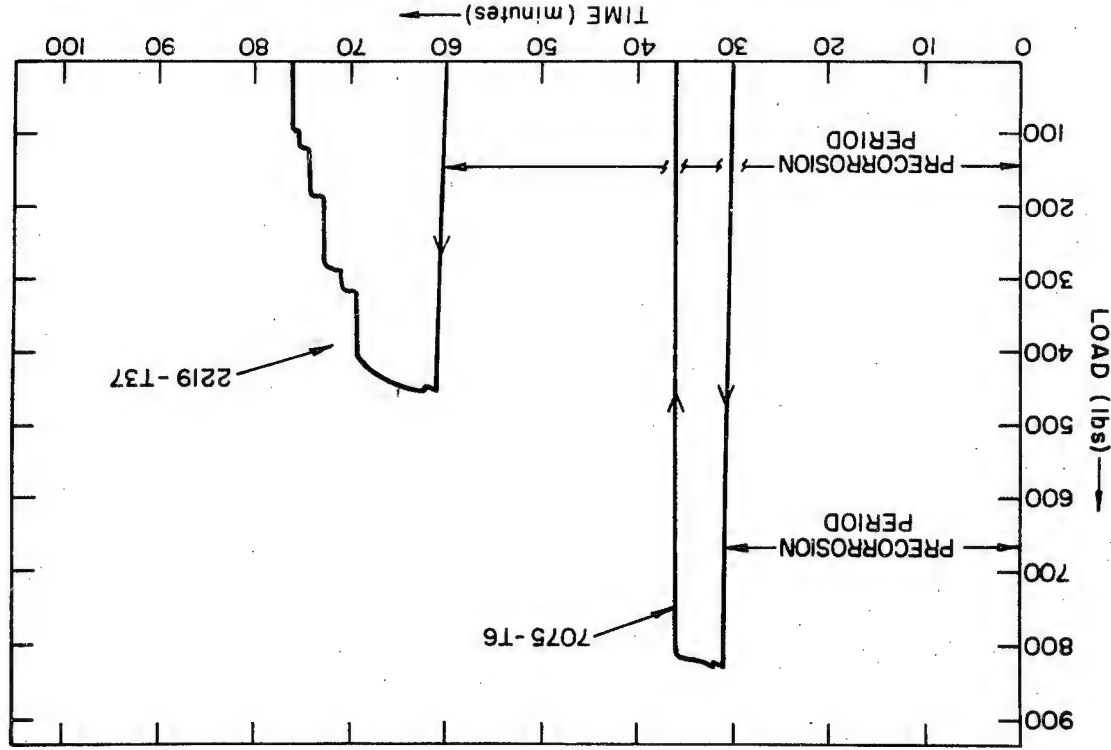
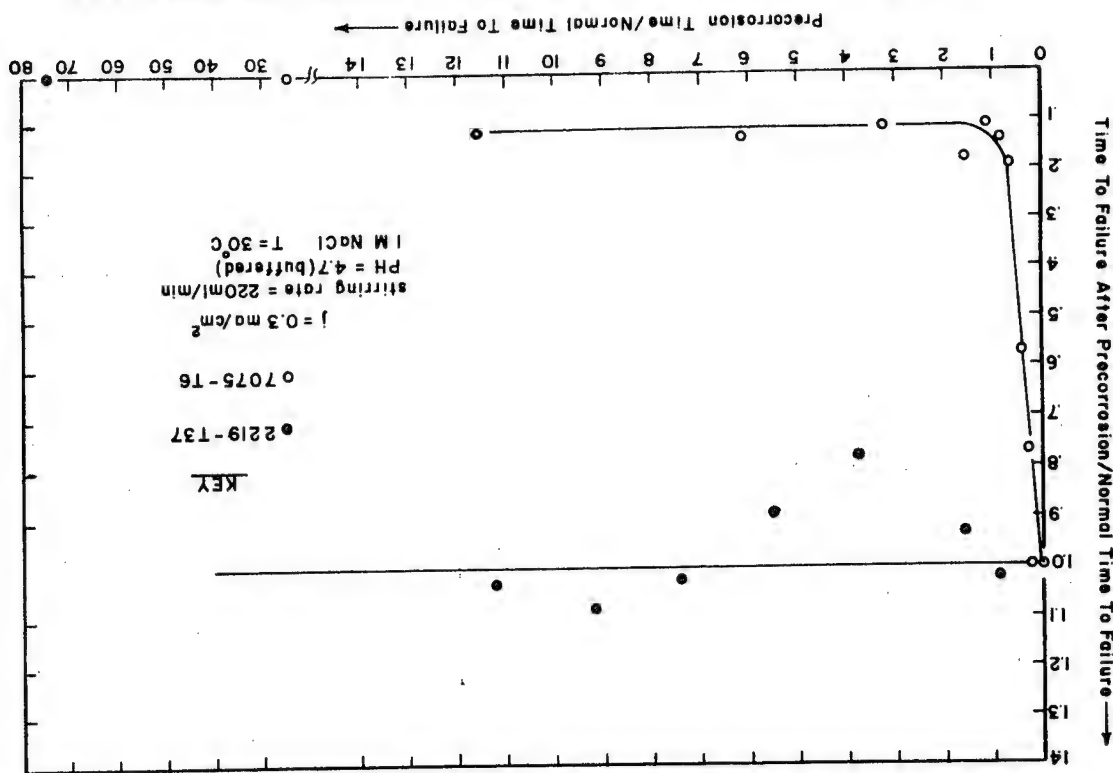


Fig. C.13 Normalized time-to-failure vs. precorrosion time for 7075-T6 and 2219-T37.

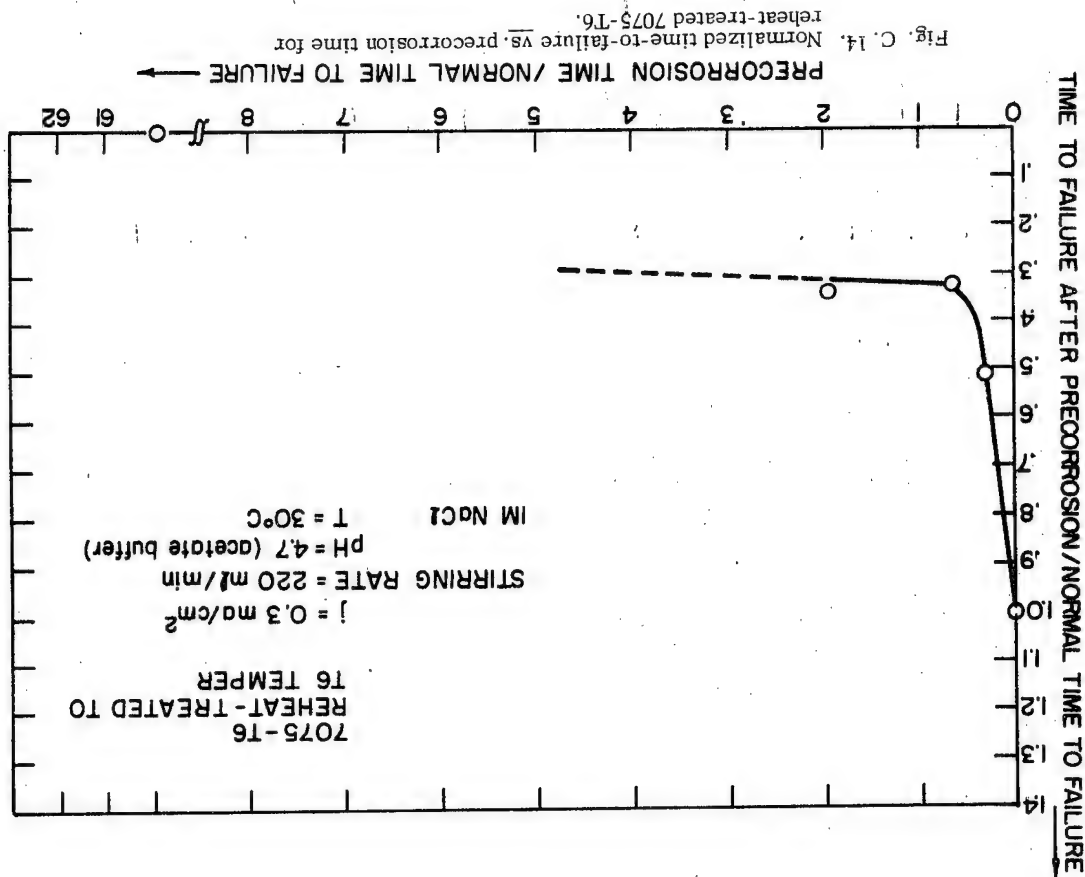


from the application of the load. The corrosion treatments which are carried out before loading are called precorrosion. By plotting the time to failure, measured from the time of load application, versus the pre-corrosion time, it is possible to determine which fraction of the total failure process represents true stress corrosion and which part represents either pure corrosion or some intermediate interaction between stress and corrosion. This can be done because if the corrosion without stress had no effect on the subsequent stress corrosion life, the resulting plot of time to failure versus precorrosion would consist simply of a horizontal line parallel to the precorrosion time axis and of a distance from that axis equal to the normal time to failure. If, on the other hand, the precorrosion were initially exactly as damaging as corrosion with stress, then the graph would have an initial slope of minus one. This is so because one unit of precorrosion time would then decrease the subsequent time to failure, measured from the time of application of the load, by one unit of time.

The above considerations have led to the definition of an index to give quantitative measure of the importance of stress. This index is called the precorrosion susceptibility index (PSI) and is defined as

$$\text{PSI} = \frac{d \text{ (time to failure after precorrosion)}}{d \text{ (time of precorrosion)}}$$

This index will then vary from zero for the case where precorrosion has no effect, to unity for the case where corrosion without stress (precorrosion) is just as effective in causing failure as is corrosion with stress. Tests on the two alloys 2219-T37 and 7075-T6(51) have shown that for the first alloy the PSI has a value of almost zero, while for the second alloy this index is initially unity. These results are shown in Fig. C.13. Furthermore, it has been found for 7075-T6(51) that after precorrosion for periods up to the normal time to failure this PSI value changes from unity to almost zero. That is additional precorrosion has no further diminishing effect on the subsequent time to failure. Hence, this region



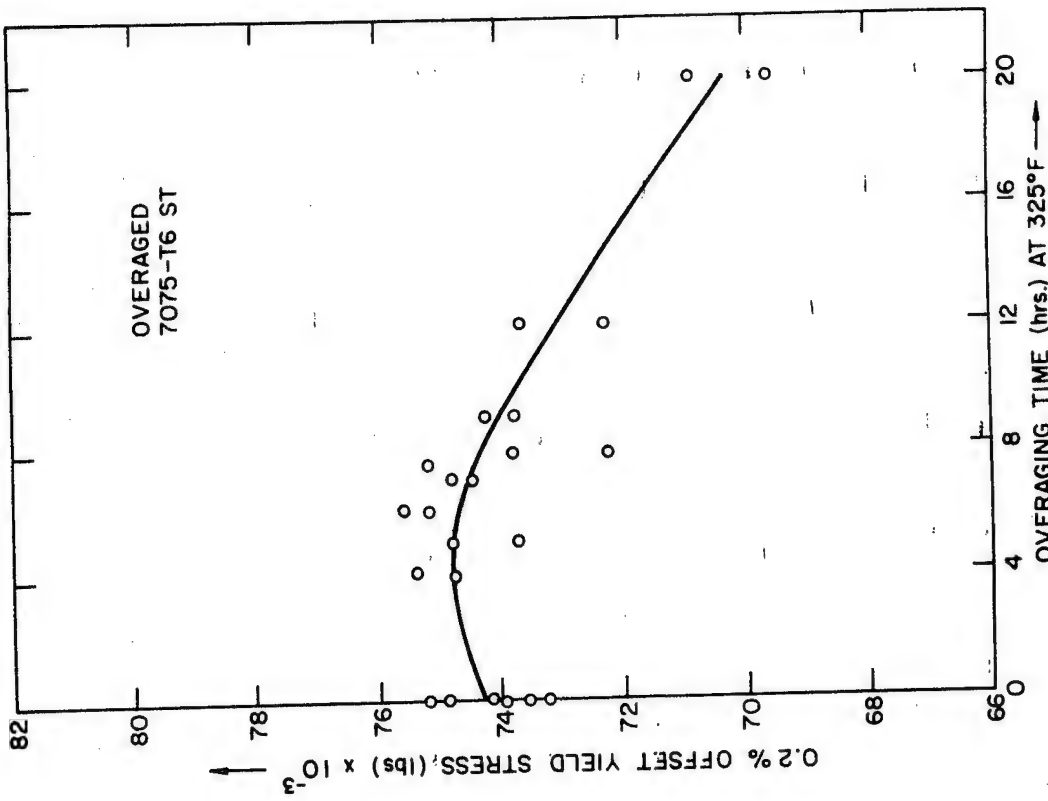
represents true stress corrosion according to the definition given above. This is generally true, namely a PSI of zero corresponds to a true stress corrosion process. Conversely, when the PSI is unity, a pure corrosion process, unaccelerated by stress, is occurring. In the case of 7075-T6(51) the period of true stress corrosion, as measured by the time to failure after precorrosion treatments of one or more times the normal time to failure, is found to amount to only 20% of the normal time to failure (the time to failure determined when load and corrosion are applied to the specimen simultaneously). Tests on reheat-treated specimens showed that this effect could not be due to residual stress (see Fig. C.14).

From the above results it can be seen that many of the heat-treatment procedures developed to increase the stress corrosion life of 7075 may not in fact increase its resistance to true stress corrosion. Rather, they may instead act in such a manner that only the period of precorrosion is increased. To test this hypothesis, specimens of 7075 were reheat-treated in such a manner as to bring them first to the T6 temper, followed by overaging at 325°F to carry them towards the T73 temper. This latter temper would be approached by overaging for 24 hours at 325°F. The normal times to failure for these overaged specimens as well as their true stress corrosion period were then determined.

These tests showed, as expected, that with overaging the normal time to failure increased by two orders of magnitude. Significantly, however, the period of stress corrosion was decreased almost to zero by the overaging treatment. In fact, for treatments of 18 hours at 325°F it was found that failure could not be prevented even by the application of cathodic currents, indicating that failure occurred by a purely mechanical process under these conditions.

#### 7. Effects of Heat-Treatment

To determine whether or not any of the above results could be due to the presence of residual stress, specimens were solutionized for 1 hour at 900°F to remove any possible residual stress. This was



followed by quenching into oil, preheated to the proper temperature (250°F) for aging to the -T6 temper. By quenching from the solutionization temperature into preheated oil, any quenching stresses would be minimized and essentially strain-free specimens would be produced. If any strain were produced, it would be expected to be compressive at the outer fiber of the specimen. This conclusion is reached because during quenching the outside cools first, contracts, and deforms the still hot and relatively soft interior. As the inside cools, it too contracts, placing the now cool outside in compression. The results of these tests, given in Fig. C. 14, show that the precorrosion test results could not be attributed to any residual stress mechanism and that the results obtained may be validly interpreted as has been previously described.

Finally, mechanical tests were run on the 7075 specimens which were reheat-treated to the -T6 temper in order to verify that this temper was indeed reproduced. Similarly, mechanical tests were also made on those specimens which were overaged at 350°F. The tests on these latter samples, given in Fig. C. 15, show that on initial overaging the yield stress actually increased slightly and that indeed in overaging for times of about 8 hours, the strength would be slightly above that for the -T6 condition. The normal time to failure is almost two orders of magnitude higher. Hence this heat-treatment procedure provides a means of increasing the resistance to failure without decreasing the strength. It has also the advantage that it can be applied to already fabricated parts. ]

### C. Present Work

In Fig. C. 12 of our previous quarterly report, we showed the effect of overaging at 325°F on both the normal time to failure and the period of true stress corrosion of 7075-T6. Figure C. 16 of the present report shows the normal time to failure data taken from the previous graph but augmented by additional data in the region of overaging from 6 to 16 hours. These additional data points confirm the increase of more than two orders of magnitude in normal time to failure (load and current applied simultaneously).

Fig. C. 15 Yield strength versus overaging treatment.

→ 60

neously) which occurs for overaging periods greater than 7 hours at 325°F. Since it was previously determined that the yield strength is not significantly decreased by these aging treatments, this treatment provides a no-loss method of improving resistance to failure.

In brief, this treatment consists of solutionizing for one hour at 900°F, followed by quenching directly into oil at 250°F. The specimen is then held in this oil bath for 24 hours and air cooled to room temperature. Final overaging is carried out, as noted above, by aging for varying times in an oil bath held at 325°F. The significant difference between this treatment and that normally employed to reach the -T73 temper is that of quenching from the solutionizing temperature into hot oil rather than into water at room-temperature. The advantage of this variation appears later on when, during overaging, the normal time of failure is increased without decreasing the yield strength.

Further tests on the effect of cathodic precorrosion have shown that this treatment has a small positive effect on subsequent time to failure measured after the current is made anodic. This result is shown in Fig. C. 17. In this figure, the horizontal dotted line shows the effect to be expected if the cathodization had no effect. The slight increase in subsequent time to failure indicated by the positions of the points above this line is understandable in terms of a small pH change of the sample surface such that the solution becomes locally more alkaline. That such pH changes can occur in spite of buffering was shown previously by the change in failure time with stirring. Hence this observation confirms the stirring rate effect.

In support of the nondestructive testing work of section D, tests were carried out in order to determine the time to failure of both 7075-T6(51) and 2219-T37 at 60% of their 0.2% offset yield strengths under the same conditions used to determine the failure time at the 90% stress level. These tests yielded normal failure times of 94.7 min. and 36.2 min. for 7075-T6 and 2219-T37, respectively. These values compare with 32 min. and 15 min. for 7075-T6 and 2219-T37, respectively, when tested at 90% of the

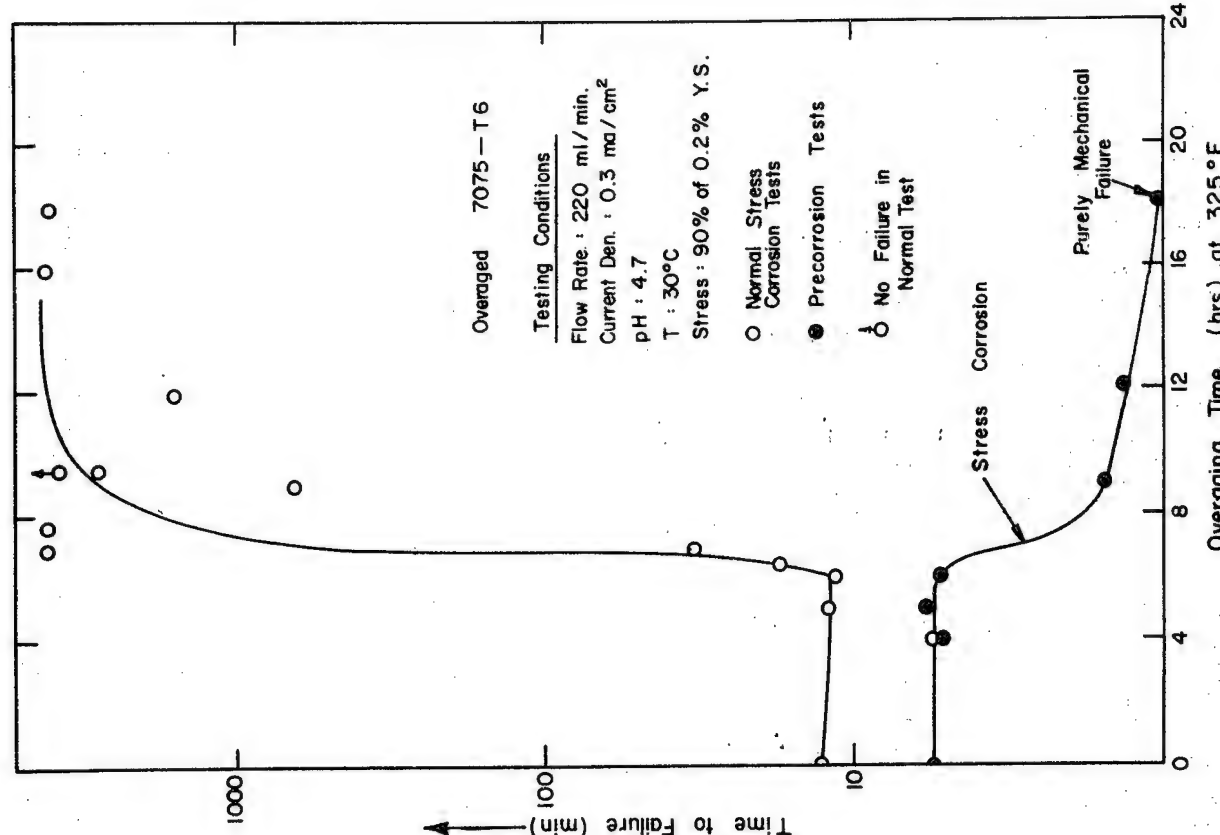


Fig. C. 16. Time to failure versus overaging time for 7075.

yield stress. The greater change of failure time of 7075-T6 with load over that of 2219-T37 is indicative of the greater sensitivity of the former alloy to mechanical conditions and is in agreement with our previous conclusion about the role played by a purely mechanical process in the failure of this alloy.

The continuing study of the effect of anodic precorrosion on the subsequent failure of 7075-T6(51) has been extended this quarter to include the effect of  $\text{Cl}^-$  concentration, anodic current density, and the effect of a second interruption of the loading cycle, as explained below.

First, Fig. C.18 shows the results of tests to determine the effect of  $\text{Cl}^-$  concentrations in solutions of 1M  $\text{Na}_2\text{SO}_4$  buffered to a pH of 4.7 with sodium acetate and acetic acid. From this figure, it is evident that  $\text{Cl}^-$  concentration exerts a critical influence. Below a concentration of  $10^{-3}\text{M Cl}^-$ , failure does not occur in more than 18 hours, while for a concentration of  $10^{-2}\text{M Cl}^-$ , failure occurs in slightly over three hours. It should also be noted that for a solution 1 molar in both  $\text{SO}_4^{2-}$  and  $\text{Cl}^-$  ion, failure occurs in 41 minutes, which is only slightly higher than the 32 minute normal time to failure determined in 1M NaCl alone.

Using the results of Fig. C. 18, precorrosion tests have been carried out in 1M  $\text{Na}_2\text{SO}_4$  containing  $10^{-2}\text{M}$   $\text{NaCl}$ , in order to determine the effect of reduced  $\text{Cl}^-$  concentration on the precorrosion and true stress corrosion processes. The results of these tests are shown in Fig. C. 19. This curve shows an initial almost level region (PSI near zero), followed by a steep region (PSI near unity). This result should be compared with that found for 1M  $\text{Cl}^-$  where there is no initial level region. Apparently the effect of the lower chloride concentration has been to introduce an incubation period during which the presence of stress is necessary for damage to occur.

The over-all scatter of the data is also substantially greater than that of the  $1\text{M Cl}^-$  case. This may be because, under less severe environmental conditions, specimen preparation and condition become more critical in determining time to failure. The point shown as the normal time

Fig. C.17. Normalized time-to-failure vs. precathectomy time.

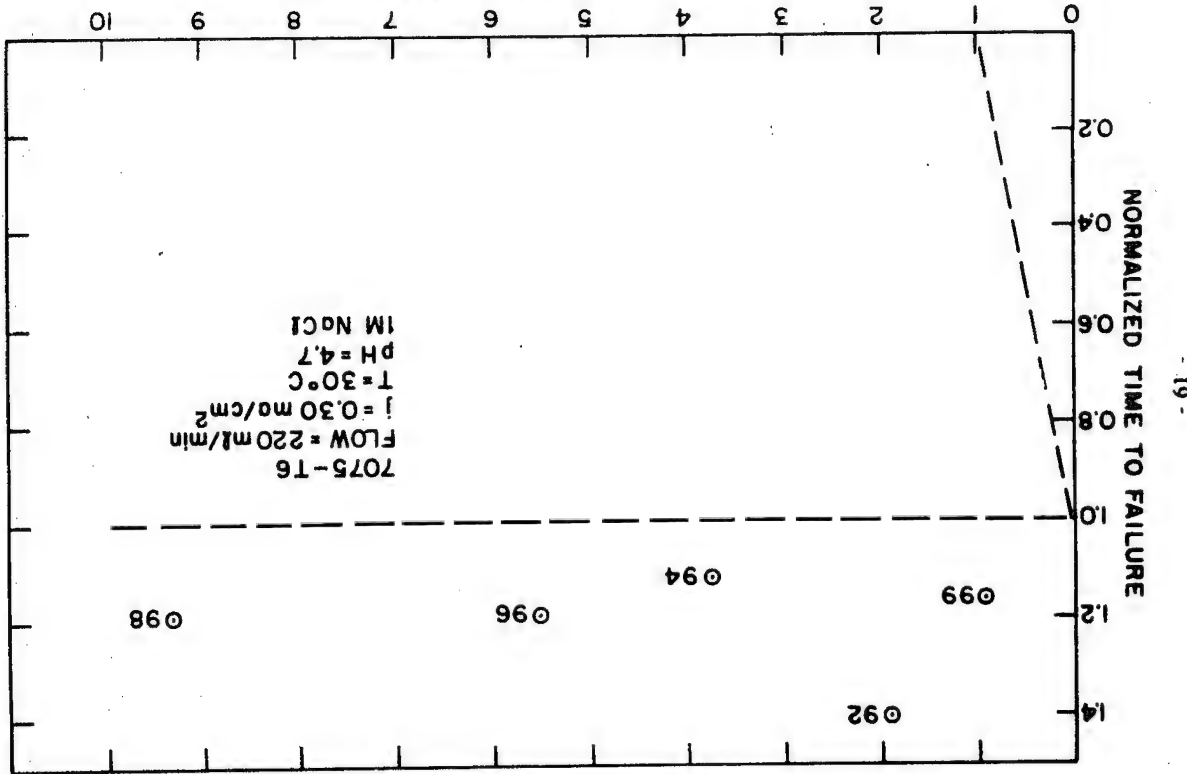


Fig. C. 19. Time-to-failure vs. precorrosion time for 7075-T6.

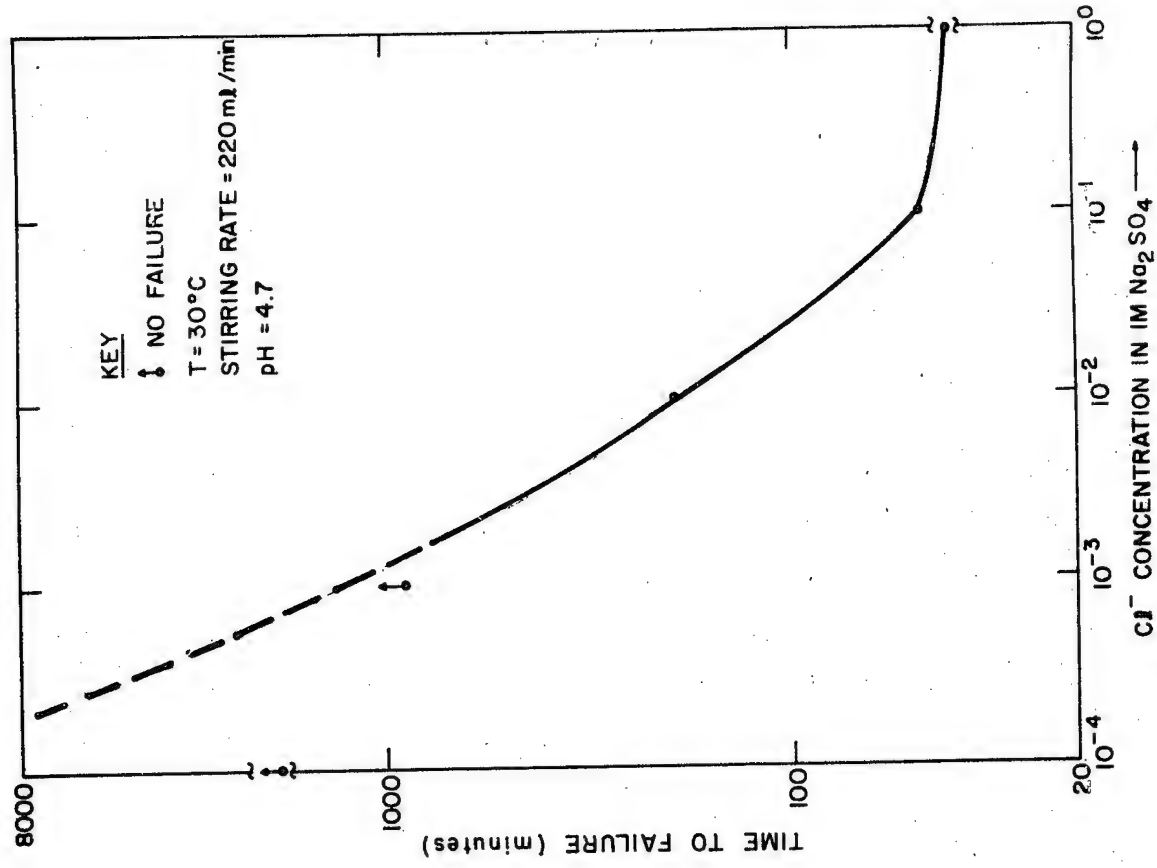
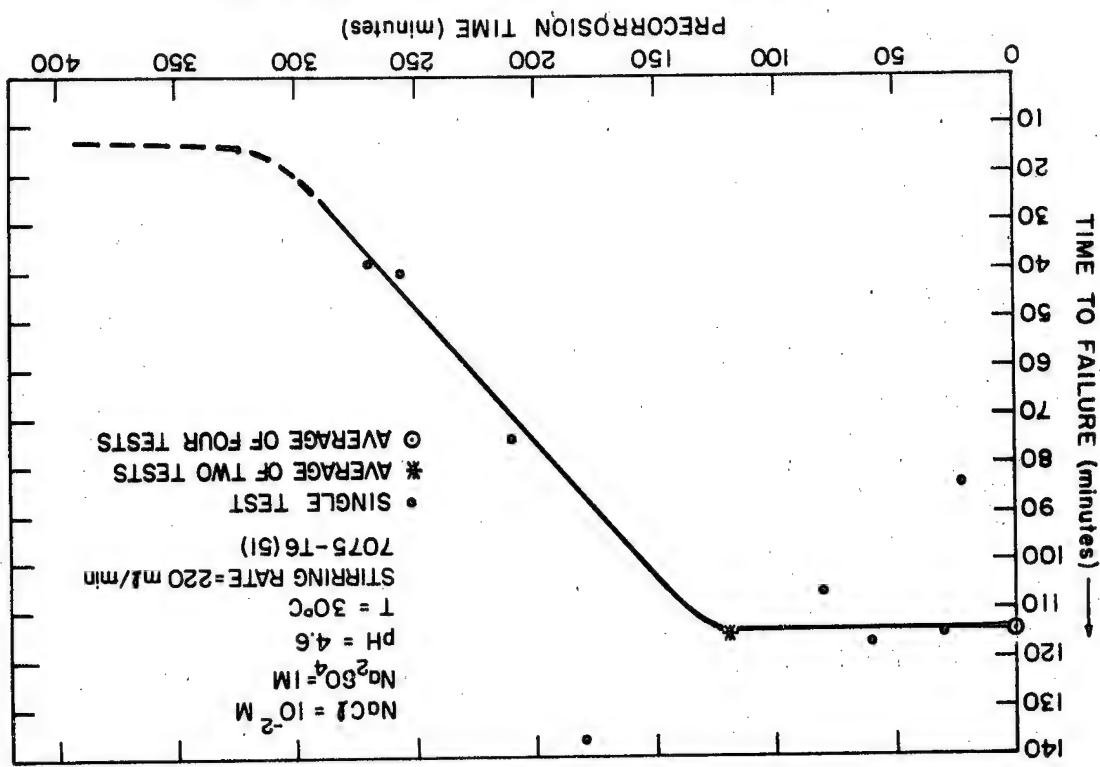


Fig. C. 18. Time-to-failure vs. Cl<sup>-</sup> concentration for 7075-T6.  
J = 0.3 ma/cm<sup>2</sup>, stress = 90% of yield stress,  
1M Na<sub>2</sub>SO<sub>4</sub>

## CURRENT CONSTANT THROUGHOUT TESTS

to failure, for example, is the average of four tests which gave values between 68 and 192 minutes. The reasons for this high degree of variation are being investigated, and it is expected that additional data points are required before Fig. C. 19 will be completely defined.

A new type of intermittent corrosion test has been carried out in order to try to clarify the mechanism of the processes which occur during the period of true stress corrosion. The description of this new testing procedure is made with reference to Fig. C. 20. This shows load versus time curves for both (a) a standard precorrosion test and (b) an intermittent corrosion test. In Fig. C. 20(a), as has been explained in a detailed fashion previously, it will be noted that the load is zero initially while the specimen is precorroding. The load is then applied and the time to failure measured from the time of application of the load. The anodic corrosion current is kept constant throughout the entire test.

Figure C. 20(b) shows the equivalent load versus time relationship for the interrupted load test. As before, the load is zero initially while the specimen is precorroding. The current is again kept constant throughout the entire test. Provided the precorrosion treatment is equal to a time at least as large as the normal time to failure, application of the load will bring the specimen into the true stress corrosion range. For our experiments, we have used a period of precorrosion equal to twice the normal time to failure. After precorrosion, the load is applied in exactly the same way described previously. Now, however, instead of allowing the specimen to remain under load until fracture, the load is only applied to the specimen for a time equal to one-half the period of true stress corrosion. The load is then lowered to zero and kept at zero for varying lengths of time, following which it is reapplied. The additional time under load is then measured and plotted versus the length of time (AB in Fig. C. 20(b)) during which the true stress corrosion period has been interrupted.

By means of this procedure it is possible to determine whether or not load is indeed necessary throughout the true stress corrosion

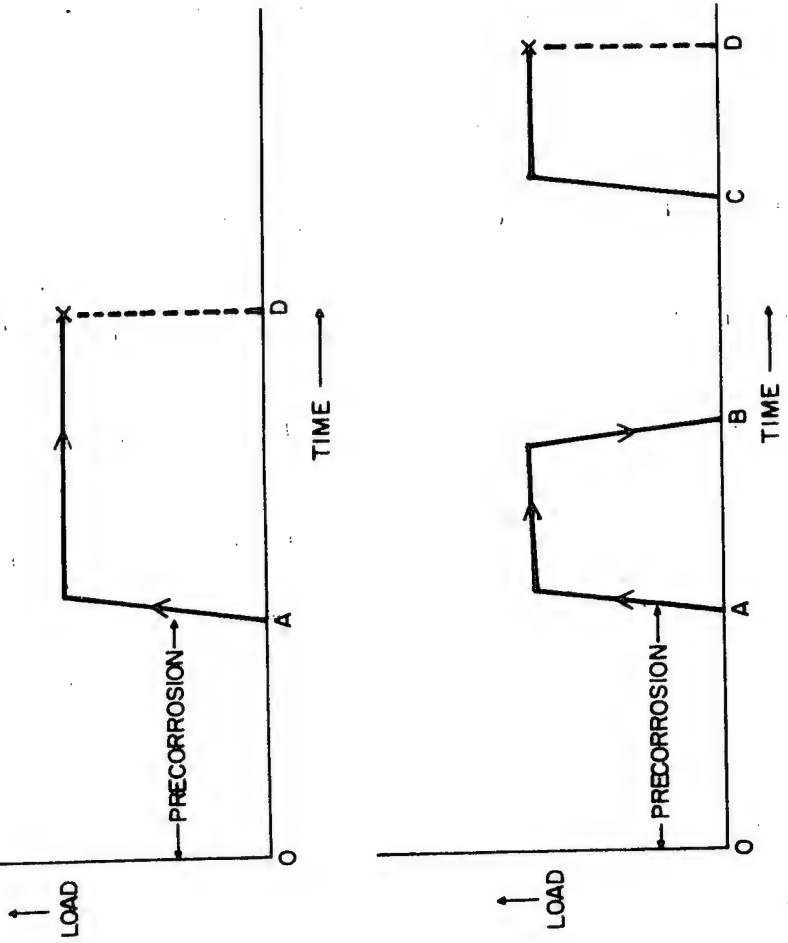


Fig. C. 20 Schematic load vs. time curves for (a) a standard precorrosion test and (b) an intermittent corrosion test.

period or whether, instead, for example, the function of the load is to reopen fissures which have become plugged with corrosion products.

In order to increase the accuracy of our results, both the normal time to failure and the period of true stress corrosion were redetermined using  $0.2 \text{ ma/cm}^2$  instead of  $0.3 \text{ ma/cm}^2$ . Replicates of three specimens were used for each determination. The lower current density was used in order to increase (1) the normal time to failure and (2) possibly also the period of true stress corrosion, relative to the values of 32 minutes and 6 minutes determined for each of these quantities, respectively, at  $0.3 \text{ ma/cm}^2$ . The normal time to failure under these new conditions was found to be 68.5 minutes while the period of true stress corrosion was found to be the same as before (6 min.).

However, at  $0.3 \text{ ma/cm}^2$ , the region of true stress corrosion was reached after a precorrosion treatment of only twice the normal time to failure. At  $0.2 \text{ ma/cm}^2$  it requires precorrosion for at least five times the normal time to failure before true stress corrosion starts. To investigate this effect further, the interrupted load tests described above were carried out using specimens precorroded for twice the normal time to failure and also for specimens precorroded for five times the normal time to failure. The results of these tests are given in Table C. II.

TABLE C. II

Intermittent Corrosion Test Data for 7075-T6.  
Table Headings Refer to Fig. C.20. Current  
Density,  $0.2 \text{ ma/cm}^2$ ; load 90% of 0.2%  
Offset Yield Stress, When Applied; Temperature,  
30°C; flow rate, 220 ma/min.

(a) Data for specimens precorroded for twice the normal time-to-failure. Under these conditions, the time-to-failure after load is applied is usually 14.2 minutes.

Result No.	AB (min)	BC (min)	CD (min)
1	7.1	7.1	9.5
2	7.1	15.2	< 1
3	7.1	14.2	< 1
4	3.7	7.1	5.8
5	3.6	14.4	9.7*

(b) Data for specimens precorroded for 5.4 times normal time-to-failure. Under these conditions, the time-to-failure after the load is applied is usually 6.8 minutes.

Result No.	AB (min)	BC (min)	CD (min)
6	3.9	3.4	3.2
7	3.9	6.8	3.1
8	3.9	13.6	1.3
9	3.9	27.2	4.5*

\* Further tests are needed to determine whether these data points are anomalous or not.

Table C. II shows the possibility of two types of processes. First, results 1, 2, and 3 show that corrosion without stress, subsequent to a stressing treatment can continue to cause damage.

This conclusion is shown by the observation that as the intermediate pure corrosion period, BC, is increased, subsequent stress corrosion life is decreased. This observation suggests that the function of load at this stage is to make the tips of corrosion crevices active sites for continued attack. This is the type of behavior which would be expected if oxide rupture or corrosion debris rupture controlled the corrosion rate at the crack tip.

For interrupted load tests which are started after one-quarter of the true stress corrosion period\*, however, (results 4 and 5) subsequent corrosion without stress does not have a strong effect. This is consistent with the former data, if creep at the crack tip is a necessity, since the time involved (about 3-4 minutes) may not be sufficient to allow a reasonable amount of flow. This view is compatible with results 6, 7, 8, and 9 for specimens precorroded for 5. 4 times the normal time to failure, since in this case the time to failure after pre-corrosion and after application of the load is short (6. 8 minutes).

Hence, interrupting the load after one-half the true stress corrosion period means that the load has again only been applied for 3. 9 minutes which, as before, might not allow sufficient creep to occur to cause the corrosion crevice tips to become active sites.

The above hypothesis would predict that if the only function of stress is the activation of corrosion crevice tips by creep, then such activation might occur if only load, but not corrosion, were applied. Therefore, tests in which the load, but not corrosion, were applied after pre-corrosion would be expected to show damage occurring subsequently under conditions of corrosion alone.

Second, however, it could be that experiments numbers 1, 2, and 3 give the results they do only because the specimen is not fully in the true stress corrosion region. In this case, results 6-9 would be interpreted as showing that when the true stress corrosion stage had been reached, corrosion without stress, even after intermediate stressing, would not cause damage. In this case the application of stress without corrosion after precorrosion would not change the subsequent stress corrosion behavior. This latter test is now being carried out to determine which process is pertinent.

These experiments are being pursued, and it is expected that they will yield additional insight into the nature of the interaction between stress and corrosion.

\* For specimens precorroded for only twice the normal time to failure, corrosion without stress still causes some damage. Therefore, this time should most properly be referred to as the time to failure after application of load.

SECTION D  
NONDESTRUCTIVE TESTING TECHNIQUES  
FOR THE DETECTION OF SURFACE FLAWS

I. INTRODUCTION

The work summarized in this section was devoted to the study and detection of stress corrosion cracking in the aluminum alloys 7075 (T651) and 2219 (T37) by ultrasonic Rayleigh surface waves (see part II), and to the investigation of simulated defects with Rayleigh waves (see part III).

Included in part II are results of studies of general galvanic corrosion (GGC), primarily made to help differentiate it from SCC. Also, the dispersive effects of the general surface conditions as exhibited by the attenuation were examined. Measurements of the anisotropy of the reflectivity of SCC to Rayleigh waves are reported, and practical means of detecting SCC in finished parts are considered.

Part IV is a summary of the principal observations.

II. SCC INVESTIGATION

A. General

In the investigation of SCC, U-bend specimens are corroded galvanostatically at different levels of stress, current density, and time of exposure. The last two parameters can be combined to obtain the total charge producing the corrosion (coul/cm<sup>2</sup>). The SCC samples for study by ultrasonics were prepared by keeping the stress and current density constant and by varying the time of exposure or total charge.

A few of the problems associated with the SCC tests are the following:

(1) One difficulty is associated with controlling the varying conditions in the stress corrosion cell, e. g. temperature, stirring, bubbles formed on the sample during corrosion, etc. The SCC cell is in a nitrogen atmosphere with nitrogen constantly being bubbled through the solution (NaCl) to remove any dissolved oxygen. The counter electrode is a ring at the bottom of the cell to insure a symmetrical current distribution. Although it was not possible to control the conditions completely in the cell, we do not believe that much variability arose from this cause.

(2) Another problem may be that different samples probably have different metallographic characteristics. We have found differences in tensile strengths of samples cut from different parts of the same plate. It was not possible to measure the strength of every U-bend, and significant variation seems likely.

(3) Stress calibration and sample geometry are crucial parameters in the SCC tests. The maximum stress,  $\sigma_m$ , in the outer fiber at the bend of the U-bend samples can be calculated from the formula

$$\sigma_m = \frac{3 L P}{2 W d^2} \quad (1)$$

where  $P$  is the applied load; and  $L$ ,  $W$ , and  $2d$  are the length, width, and thickness of the U-bend samples, respectively. Values of the stress were found by elastically deforming the U-bend specimen using known loads and measuring the resulting deflection of the legs.

An example of the variability depending on source of the material is illustrated in Fig. D. 1 which is a stress-calibration curve for the U-bend specimens. The abscissa of this plot is the change in  $D$  (separation between the legs of the U-bend sample) and is given in terms of mils and, also, as a percentage of the original separation at zero load. The ordinate is given in terms of applied load, stress in the outer fiber, and percentage of yield strength. The three U-bend specimens tested for this plot came from three different plates of 7075 designated as series A, B, and C. The thickness of these samples at the bend was the same and equal to the nominal value of 0.250 inches. The graph indicates that even though the samples were geometrically identical, their stress-calibration curves were not. For instances, at 99% of the yield strength the corresponding deflections for U-bend specimen series A, B, and C are 0.507", 0.525", and 0.493". Thus if a series C sample is to be stressed to 90% of the yield strength using the calibration curve for series B, the actual stress of the specimen will be about 96% of the yield strength, and its SCC life will be drastically shortened.

Stress-calibration curves were also prepared for 2219 (T37). The 0.2% offset yield strength was taken as 44,000 psi. The load deflection curves for this alloy are shown in Fig. D. 2. Three of the curves correspond to U-bend specimens no. 6D, 18D, and 42D, which originated from the same plate, but with thicknesses at the bend of 0.248, 0.250, and 0.252 inches, respectively. The fourth curve is for a sample coming from a different plate with a thickness at the bend of 0.251 inches. The dashed line in this graph, included for comparison, is the average for series A, B, and C of the 7075 U-bend specimens.

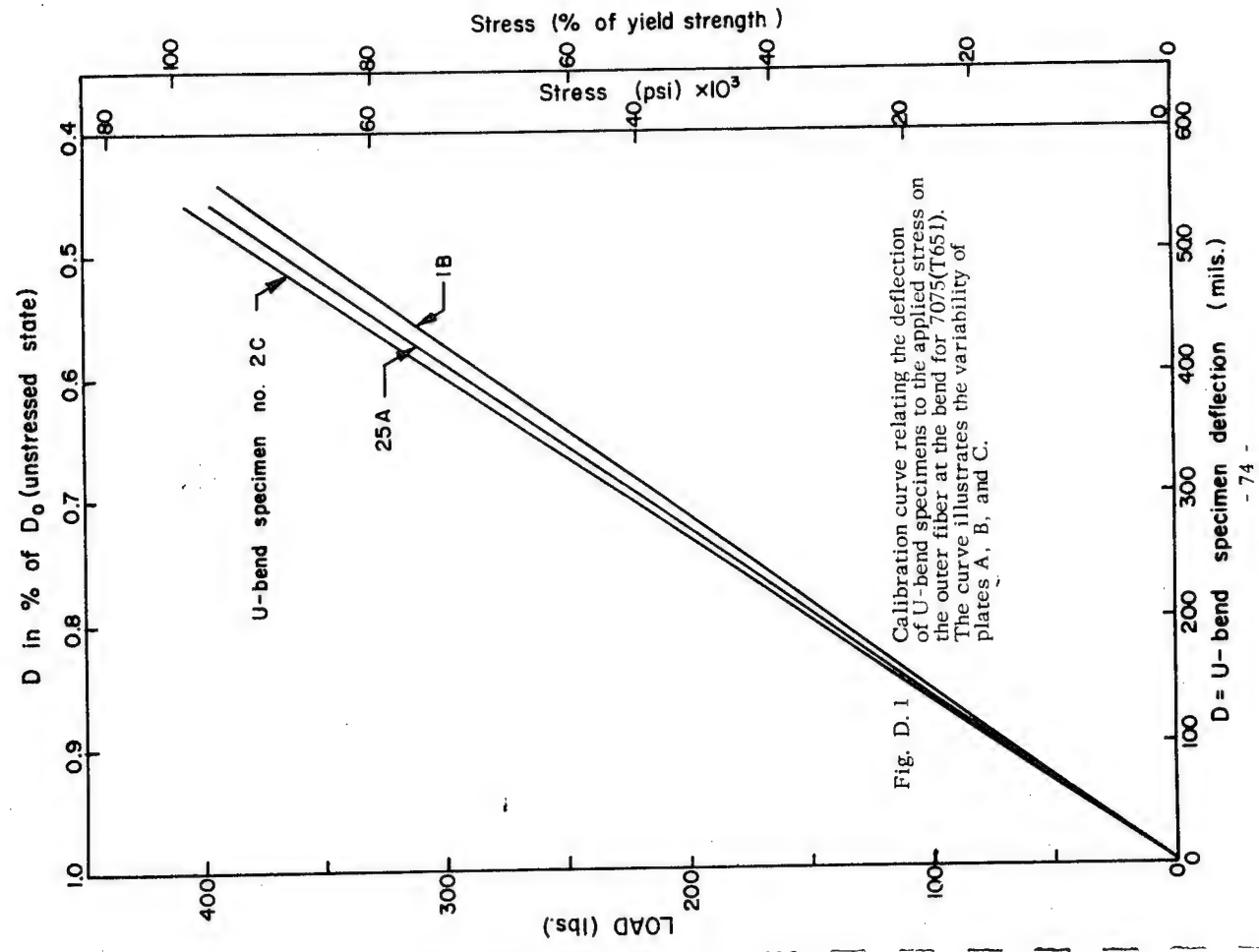


Fig. D. 1 Calibration curve relating the deflection of U-bend specimens to the applied stress on the outer fiber at the bend for 7075(T651). The curve illustrates the variability of plates A, B, and C.

The graph illustrates the effect of the different origins of the samples and the shifting of the load-deflection curves due to differences in specimen thickness at the bend. The deflection of the legs,  $D$ , is proportional to  $\sigma_m$  (assuming  $d \ll L$ )

$$D = \alpha \frac{L}{d} \sigma_m \quad (2)$$

where  $\alpha$  to first order is a numerical constant depending only on the elastic properties of the material. Note that  $\sigma_m$  is only linearly dependent on  $d$  instead of quadratically as in eq. (1); thus, the best way to stress the U-bends is to use a predetermined deflection rather than load. As a general practice the thickness of the U-bend specimens was  $0.250^\circ \pm 0.002^\circ$ , which would produce not more than a  $\pm 1\%$  variation in stress.

In the work with artificial defects discussed in previous quarterly reports, the actual SCC damage was simulated by defects of known geometry, and their reflectivities and their attenuation of Rayleigh waves were measured.

The general nature of SCC involves closely spaced microcracks which, depending upon their relative separation, can produce either single or distinct echoes. Ideally, two isolated parallel grooves have to be a finite distance apart before they can produce two distinct signals on the screen of the ultrasonic flaw detector. This is the "resolving power" of the instrument and may be defined as the ability to distinguish between two closely spaced grooves. This depends, among other things, on the pulse width of the emitted wave, on the bandwidth of the detection system, and on the oscillator frequency.

To determine the actual resolving power of the instrument used in this investigation (Krautkrämer, type USIP 10W, 4 MHz probe), two 1.5 mil-wide parallel grooves with varying separations were cut on a flat surface of 7075, and the corresponding oscillosograms observed. From the results it was determined that the resolving power of the instrument is roughly 1.5 mm and is about the same as for similar

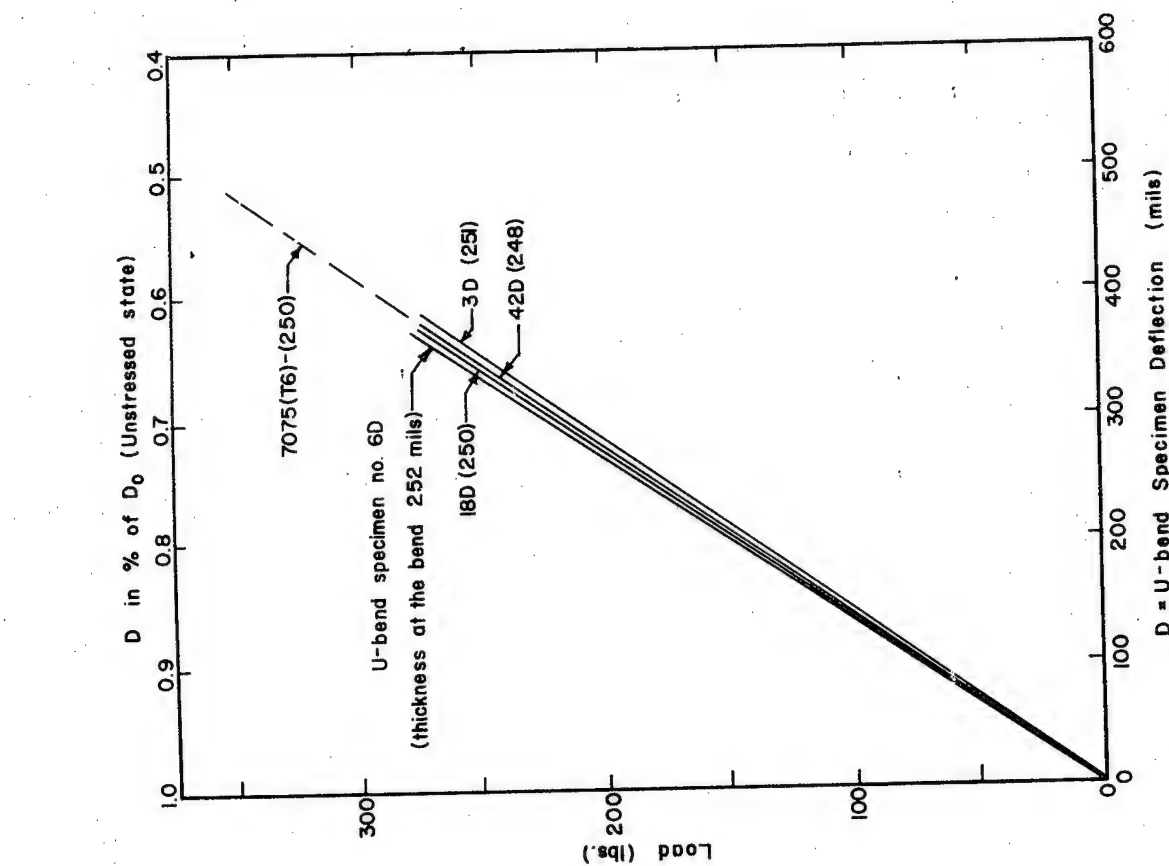


Fig. D. 2 Calibration curve relating the deflection of the U-bend specimens to the applied stress on the outer fiber at the bend for 2219(T37).

instruments reported by other experimenters.\* Since similar settings were used in the SCC investigation, echoes from microcracks were not necessarily completely resolved. A single echo from the corroded area then could easily correspond to several closely spaced microcracks or pits.

B. Surface Attenuation

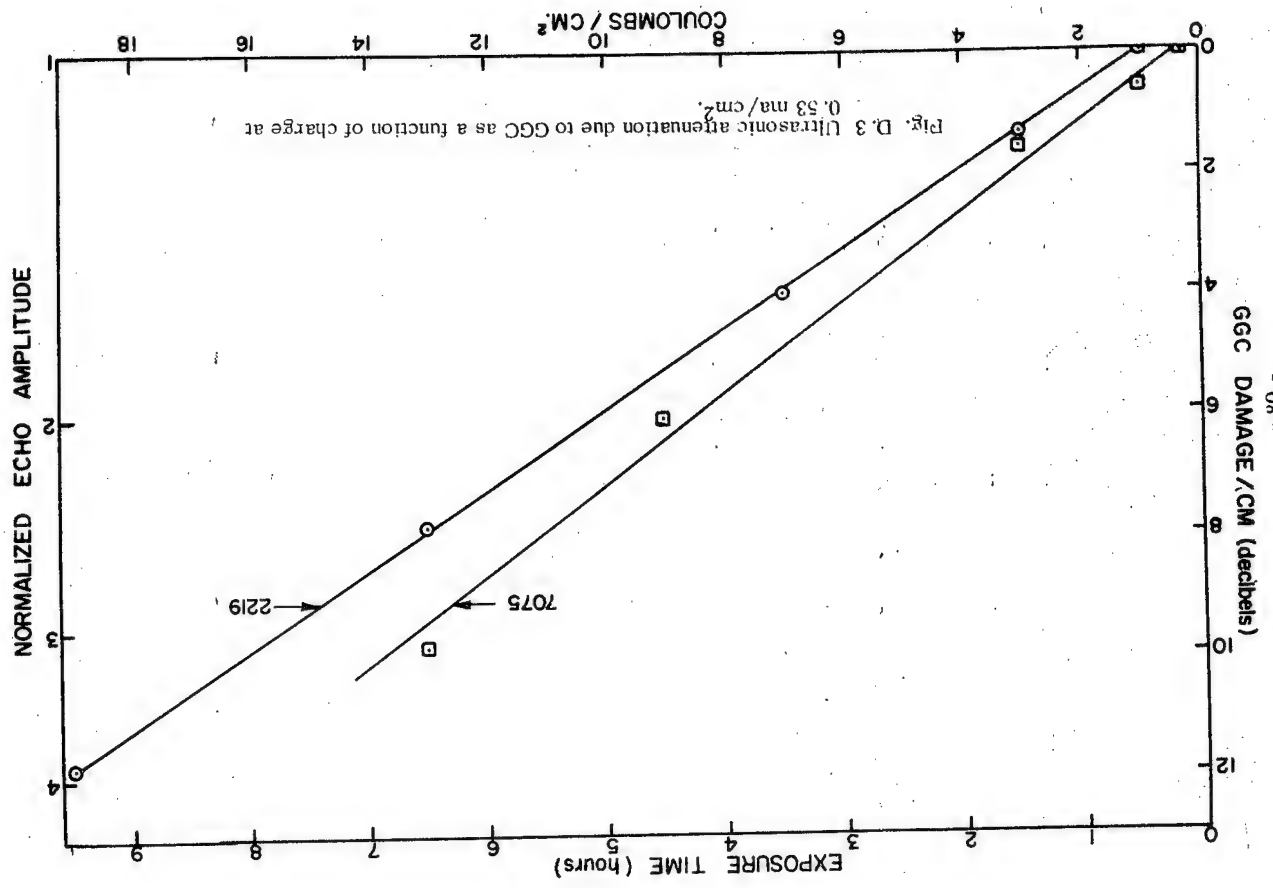
One of the most important parameters in ultrasonic testing is the attenuation of the Rayleigh wave as it propagates over the surface. The attenuation in general is caused either by the divergence of the ultrasonic beam or by the interaction the wave undergoes as it propagates through or over the medium. The measurements included data on surface finish ranging from that produced by No. 36 grit paper to that produced by No. 2 polishing alumina (aluminum oxide-particle size 0.3 microns) over distances up to 22". Results were obtained in both the long transverse and the rolling directions, and also include painted surfaces. In addition, data were obtained when the direction of propagation of Rayleigh waves was perpendicular or parallel to the direction in which the abrasive paper was moved to produce the surface finish.

A synopsis of all our attenuation data for 7075 and 2219 is given in Table D.1. From this table it is seen that the value of attenuation in the rolling direction for both alloys is about the same—0.15 db/cm for 7075 and 0.14 db/cm for 2219. We also see that for 2219 the attenuation is greater in the rolling direction than in the long transverse, as expected, but the difference (0.03 db/cm) is smaller than the corresponding difference (0.09 db/cm) for 7075. A possible explanation is in the grain structure of these alloys. In the case of 7075 the grains are somewhat elongated, thus resulting in more grain boundaries per unit distance in the long transverse direction. This would increase the scattering in this direction.

TABLE D.1  
Attenuation of Rayleigh Waves on Plane Surfaces of Aluminum Alloys at 4 MHz

Aluminum Alloy	Propagation Direction	Surface Finish	Attenuation db/cm	Remarks	
				7075(T651)	7075(T651)
7075(T651)	Rolling	no. 36 grit paper and finer and "as rolled"	0.15		
7075(T651)	Rolling	no 36 to no. 80 grit paper	0.30	Rayleigh waves perpendicular to lay of finish	
7075(T651)	Long Transverse	no. 36 grit paper and finer and "as rolled"	0.24		
7075(T651)	Long Transverse	2-mil paint coat	0.45		
2219(T37)	Rolling	no. 180 grit paper and "as rolled"	0.14		
2219(T37)	Long Transverse	no. 150 to no. 180 grit paper and "as rolled"			

\* Binczewski, G. J., "Standardization and Application of Surface-Wave Inspection," Nondestructive Testing, January-February 1957, pp. 36-40.



Several important conclusions may be drawn. The surface finish has a remarkably small effect on the attenuation, especially if the direction of finish is parallel to the propagation direction. Even with a very rough grit (No. 36), attenuations of only 0.3 db/cm were obtained. This is small compared with that produced by SCC; (see Fig. D.6, D.7, and D.8 for typical SCC attenuation data). The painted surfaces used here introduced an increase in attenuation of approximately two-fold this is fairly small when compared with SCC. To summarize, we can say that for most reasonably finished surfaces the exact character will not be too important in observing SCC effects. Even if the surface finish of parts to be tested is unknown or rougher than surface conditions investigated here, an attenuation curve can readily be obtained before actual testing begins.

#### C. General Galvanic Corrosion (GGC)

In order to help differentiate between the effects of general corrosion (GGC) and stress corrosion (SCC), tests were performed using the same procedure as in the SCC case, except for the removal of stress.

Details of the GGC tests for 7075 were discussed in previous quarters. The investigation for GGC of 2219 was completed during the last quarterly period. The results of ultrasonic measurements for 2219, along with the results for 7075, are plotted in Fig. D.3. This figure shows the GGC damage, as measured by ultrasonic attenuation, vs. the amount of corrosion in coulombs/cm<sup>2</sup>. The graph indicates that the data for 2219 falls on a straight line and is even more consistent than the data for 7075 which also shows a linear dependence on corrosion. No data could be obtained for 7075 after an exposure of 13 coul/cm<sup>2</sup> (or 6.5 hours) because the reflection from the second reference groove was totally attenuated. The data for both 2219 and 7075 have approximately the same slope (0.67 db/cm per coul/cm<sup>2</sup>), but the 7075 has a slightly small x-axis intercept (0.3 coul/cm<sup>2</sup>). This

implies that appreciable surface disturbance from GGC results from less attack in 7075 than in 2219. The x-axis intercepts are about 0.3 and 1.0 coul/cm<sup>2</sup> for 7075 and 2219, respectively.

This x-axis intercept should not be interpreted as the period that the alloy is not attacked by corrosion (incubation period), but rather as the threshold of ultrasonic detectability. This is illustrated by photomicrograph (a) of Fig. D. 4, which shows the surface condition on the corroded area after an exposure of 1.0 coul/cm<sup>2</sup> or 30 min (x-axis intercept) at a current density of 0.53 ma/cm<sup>2</sup>. This picture clearly demonstrates the existence of corrosion damage (pits) even though it could not be detected ultrasonically. Part (b) of Fig. D. 4 shows the surface condition after an exposure of 19 coul/cm<sup>2</sup> or 9.5 hours. The dark areas in this photomicrograph are deep pits that produced definite echoes and drastically attenuated the second reference echo.

Fig. D. 5 is a typical series of GGC oscillosograms for 2219 showing the attenuation of the Rayleigh waves with increasing corrosion. Part (a) of this figure is the reference oscillosogram showing the un-attenuated echo from the reference groove (the tall echo to the far right) and parts (b) and (c) correspond to exposures of 7 and 13 coul/cm<sup>2</sup> or 3.5 and 6.5 hours respectively. Note the decrease in echo from the reference groove.

#### D. SCC Tests at 90% and 60% of The Yield Strength

Investigations of SCC using ultrasonic surface waves have been made of U-bend specimens stressed to 90% and 60% of their 0.2% yield strengths, for both 7075 and 2219 alloys. The results for 7075 are summarized in Fig. D. 6, and for 2219 in Figs. D. 7 and D. 8. Also included are the results of GGC tests, for which the current density was the same. The GGC curves are an expansion of the lower left hand corner of Fig. D. 3. In these figures the increase in attenuation per unit distance is plotted as a function of the amount of corrosion.



(a)



(b)

Fig. D. 4 Photomicrographs (300 X) of the surface condition of a 2219(T37) U-bend specimen illustrating the effect of GGC at 0.53 ma/cm<sup>2</sup> after an exposure of (a) 1.0 coul/cm<sup>2</sup> or 30 min and (b) 19.0 coul/cm<sup>2</sup> or 9.5 hours.

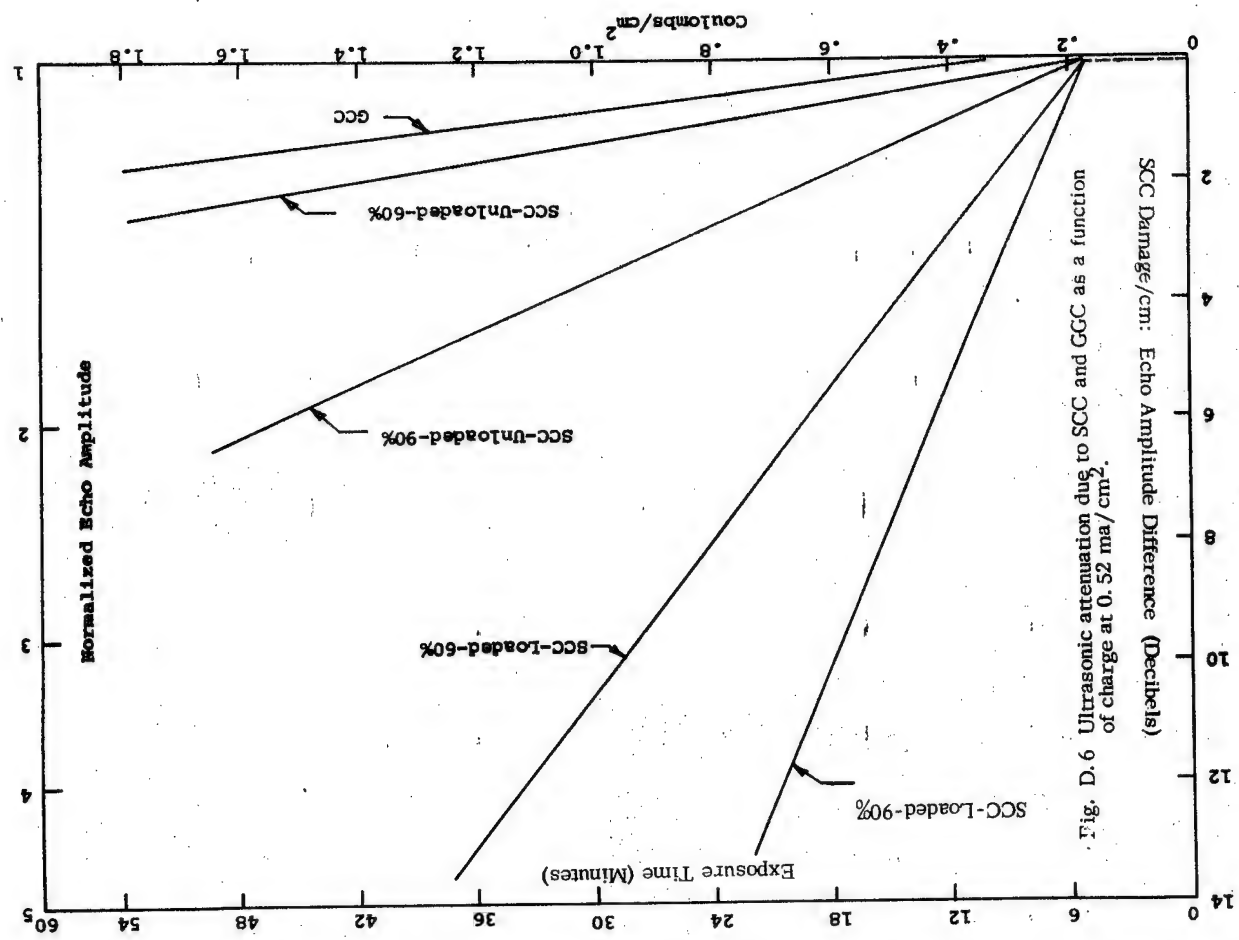


Fig. D.5 Oscillograms illustrating the effect of GGC for 2219(T37) at 0.53 ma/cm<sup>2</sup>.  
 (a) Reference oscillogram  
 (b) After 3.5 hours or 7.0 coulcmhs/cm<sup>2</sup>  
 (c) After 6.5 hours or 13.0 coulombs/cm<sup>2</sup>

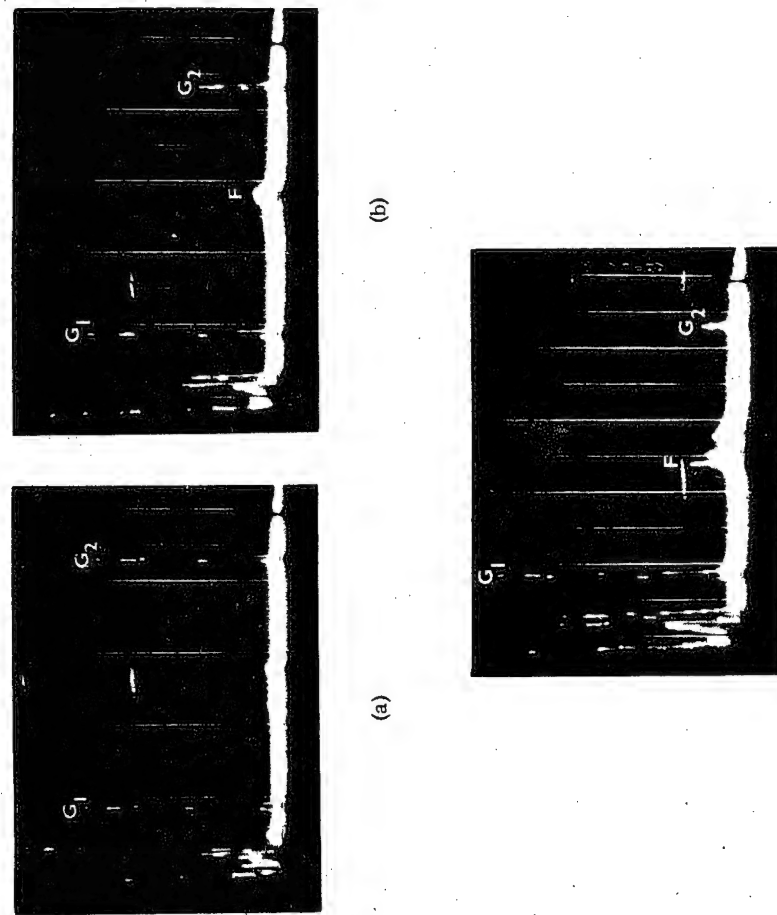


Fig. D.6 Ultrasonic attenuation due to SCC and GGC as a function of charge at 0.52 ma/cm<sup>2</sup>.

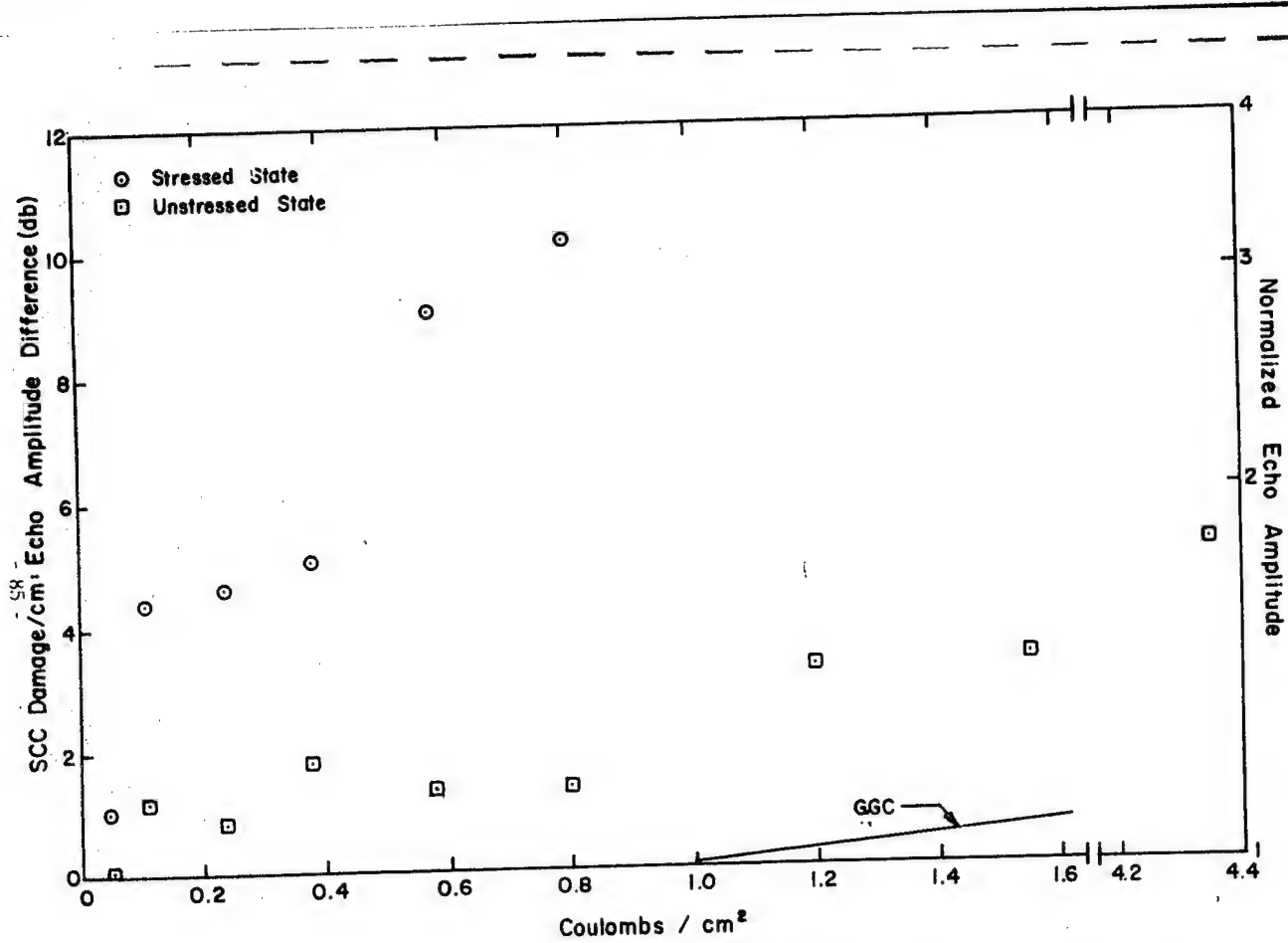


Fig. D. 7 Ultrasonic attenuation due to SCC damage for 2219(T37) as a function of corrosion charge at 0.62 ma/cm<sup>2</sup> and 90% of the yield strength.

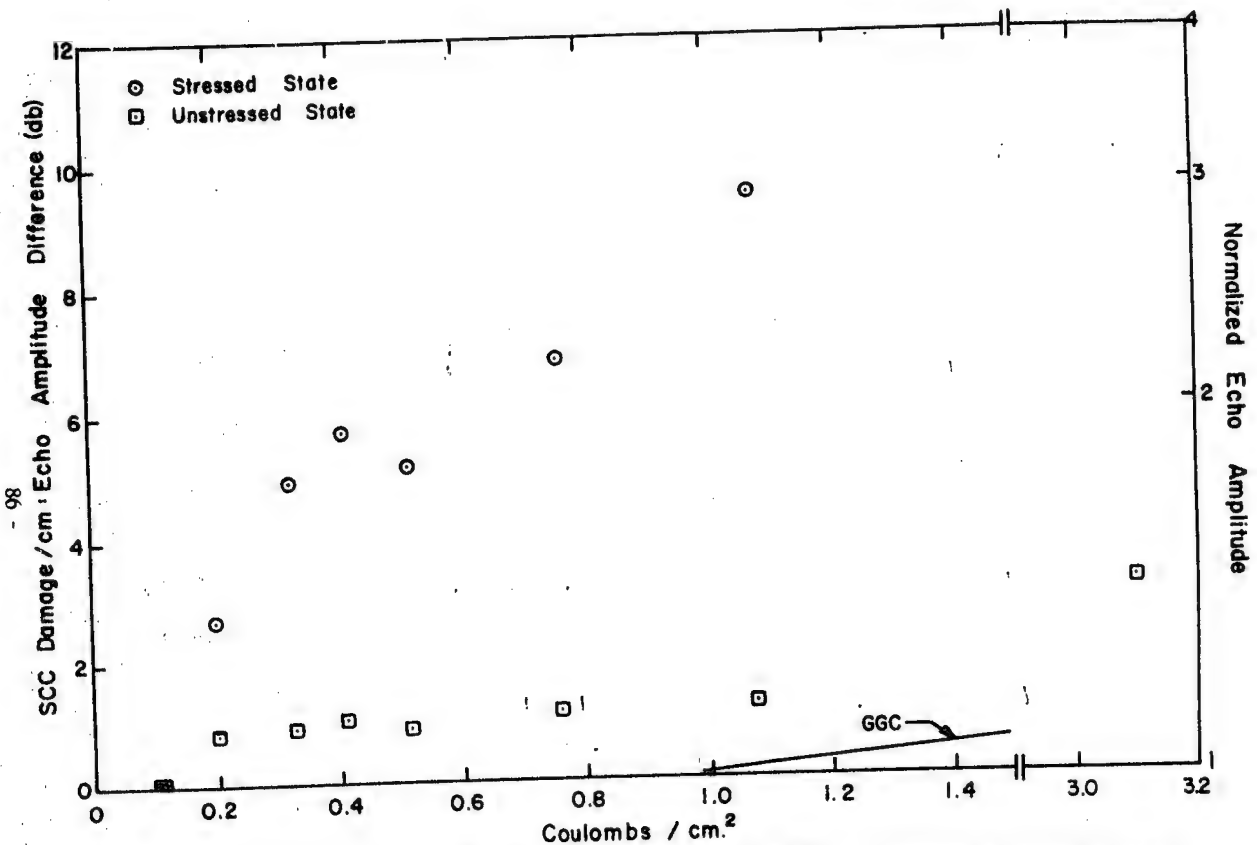


Fig. D. 8 Ultrasonic attenuation due to SCC damage for 2219(T37) as a function of corrosion charge at 0.57 ma/cm<sup>2</sup> and 60% of the yield strength.

The results indicate that for equal amounts of corrosion the attenuation was largest for the sample stressed to 90%, probably because of the more rapid development of the microcracks. The attenuation in both the 90% and 60% cases, while still under stress, is approximately a factor of five higher than when the stress is released. Even when the U-bend is not under stress, the attenuation is substantially higher than that produced on samples subjected to general galvanic corrosion.

The line for the GGC data has a much smaller slope. For example, the ratios of slopes for SCC-loaded-90%, and GGC are 23:4:1, respectively. All three lines have a nonzero intercept and tend to converge to the same value of  $0.2 \text{ coulombs/cm}^2$ . The distance between 0 and  $0.2 \text{ coulombs/cm}^2$ , indicated in the graph by the dashed line, can then be interpreted as an incubation period for ultrasonic detectability. This is verified by the fact that the data obtained after  $0.185 \text{ coulombs/cm}^2$  exposure showed no measurable attenuation.

The ultrasonic analysis showed some differences between 2219 and 7075. These are as follow:

(1) Relation of damage to exposure. The data for 2219 shows more scatter and seems to indicate a stepwise increase in the SCC damage with increasing exposure. This was not observed in the case of 7075 which rather showed a smooth monotonic increase.

(2) Incubation period. There does not appear to be any incubation period for 2219 stressed to 90% of the yield strength except for possibly a small ( $\sim 0.04 \text{ coul/cm}^2$ ) ultrasonic detectability threshold in the unstressed state. The corresponding incubation period or threshold for 7075 is about  $0.2 \text{ coul/cm}^2$ .

For 2219 stressed to 60% of the yield strength, analysis of small echoes from microcracks indicated that the incubation period is less than  $0.1 \text{ coul/cm}^2$ . This is shown in Fig. D. 9. Part (a) of this figure is the reference oscillosogram and part (b) is the oscillosogram

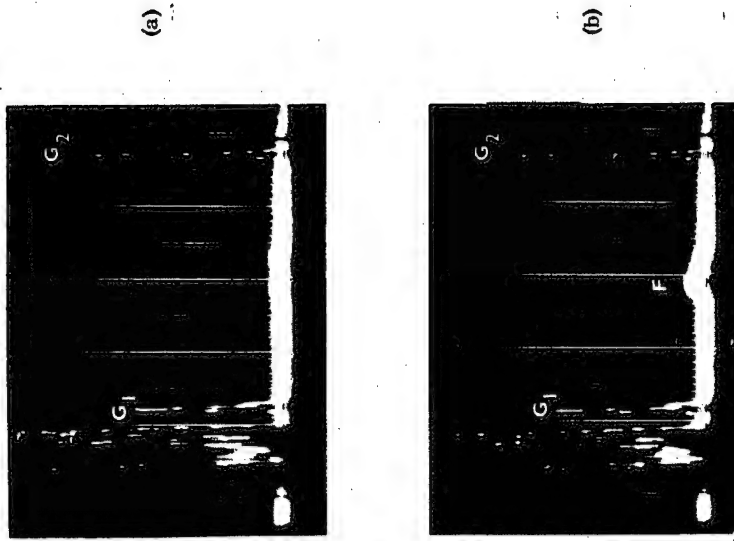


Fig. D. 9 Oscilloscopes illustrating the effect of SCC for 2219(T37) at 60% of the yield strength and  $0.53 \text{ ma/cm}^2$ .  
 (a) Reference oscillosogram  
 (b) After  $0.1 \text{ coulombs/cm}^2$  at the stressed state.

obtained in the stressed state after an exposure of  $0.1 \text{ coul}/\text{cm}^2$ . The small echoes are clearly shown in part (b), even though they did not contribute much to the attenuation of the echo from the reference groove.

The microscopic examination of the specimens of 2219(T37) also show a mode of cracking different from that of 7075(T651). These differences are as follows:

(1) Nature of microcracks. The photomicrographs of 2219 indicate that the microcracks for this alloy are of a zig-zag nature compared with the relatively straight cracks of 7075. A possible explanation may be in the shorter and somewhat rounded grain boundaries of 2219 compared with the elongated grain boundaries of 7075. A discussion of the grain boundary structure of these alloys was given in section C of the Fifth Quarterly Report.

(2) Density of microcracks. For 2219 the microcracks appeared to be uniformly distributed on the corroded area, whereas for the 7075 most of the microcracks were located at the edges of the rectangularly corroded area with only a few scattered in the central region.

(3) General galvanic corrosion (GGC). There was more GGC attack for 7075 than 2219.

#### E. Determination of SCC Life (Time-to-Failure)

One of the important parameters in SCC investigation is the time-to-failure or SCC life. In this study we would like to measure the failure time in order to express the first detectable SCC damage as a fraction of this time. Usually, this lifetime was determined in separate test—not with the actual samples used for the SCC measurements. Unfortunately, considerable variability is observed in this time-to-failure, and this introduces uncertainty as to when SCC damage can first be detected in terms of lifetime.

A possible method to avoid this variability would be to obtain the SCC life for the particular U-bend used in an NDT study. This could be done in principle by continuing its corrosion until failure after the appropriate ultrasonic measurements had been made, thus eliminating any variability of the U-bend geometry. Since the measurements can not be carried out *in situ*, the U-bend must first be removed and cleaned. Restarting the corrosion could then lead to erroneous results.

The results of the tests of the U-bend specimens used for this investigation are given in Fig. D.10. For this study the stress was 90% of the yield strength. Figure D.10 is a plot of corrosion charge per unit area ( $\text{coulombs}/\text{cm}^2$ ) as an ordinate vs. the current density ( $\text{ma}/\text{cm}^2$ ) as abscissa. Most tests described in the following sections were performed at a current density of about  $0.53 \text{ ma}/\text{cm}^2$  where the average value of the SCC life at this current density is  $1.6 \text{ coulombs}/\text{cm}^2$ . This value is slightly less than the corresponding point on the straight line ( $2.0 \text{ coulombs}/\text{cm}^2$ ) in Fig. D.10 but is in best agreement with the data at that particular current density. Using  $1.6 \text{ coulombs}/\text{cm}^2$  as SCC life at 90% of the yield strength of 7075, the threshold for ultrasonic detection (incubation period  $\sim 0.2 \text{ coul}/\text{cm}^2$ ) is about 13% of the SCC life.

For the 7075 case at 60% of the yield strength preliminary tests indicated SCC life in the vicinity of  $14 \text{ coul}/\text{cm}^2$ . Assuming this value, the threshold is about 1.5% of the SCC life. However, more sophisticated mechanical tests reported in section C with cylindrical tensile specimens (at a slightly smaller current density,  $0.3 \text{ coul}/\text{cm}^2$ ) indicate a SCC life for 7075 at 60% of the yield strength twice as long. This value would give an ultrasonic threshold of about 0.7% of the SCC life. However, both values (i. e. the one obtained with the U-bend specimen and the one obtained with the cylindrical specimen) are only a small fraction of the SCC life. Thus, we could say that for the 7075 case at 60% of the yield strength the SCC damage is effectively detected (in terms of SCC life) right from the onset.

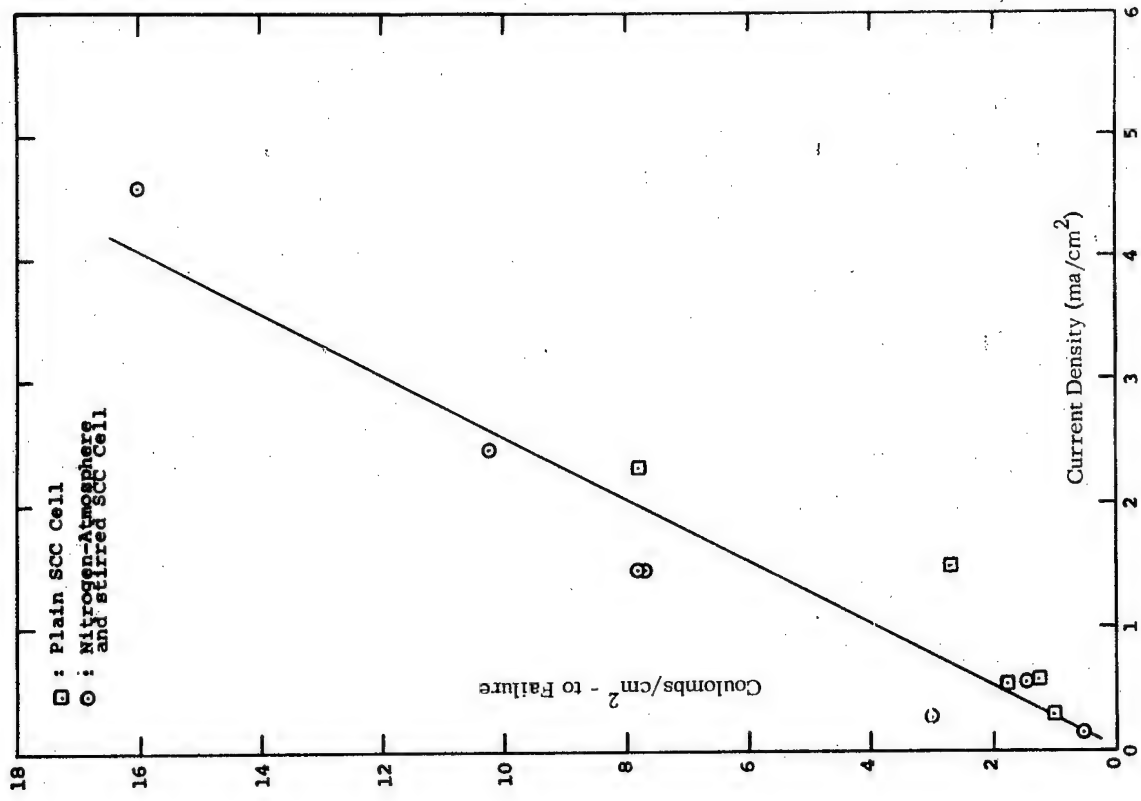


Fig. D. 10 Determination of SCC life. Graph indicates the number of coulombs/cm<sup>2</sup> required for fracture of U-bend specimens as a function of current density.

The tests of SCC life of 2219 showed that the time-to-failure for U-bend specimens is longer than for 7075. Also, the samples do not fail in the same catastrophic way as the 7075, but rather fail in a stepwise manner. Catastrophic failure of 2219 U-bend specimen (i. e. fracture into two pieces) did not occur even for very long exposures (up to 3 days); however, lifetime tests on 2219 at 60% of the yield strength performed on cylindrical tensile specimens in the main SCC cell showed that the time for the load to drop to 80% of the initial value is only 37 min. These tests were carried out at a current density of 0.3 ma/cm<sup>2</sup>, thus giving a total charge of 1.1 coul./cm<sup>2</sup> for the stress to drop to 80% of its original value. The total charge, though, for catastrophic failure is much longer. On the other hand, there is practically no incubation period for 2219 and thus the threshold for ultrasonic detection is very small.

The failure behavior of 2219(T37) was discussed in section C of the Fifth Quarterly Report and was shown in Fig. C. 32 which was a typical load versus time relationship. We pointed out that the discontinuous failure of 2219 possibly results from the halting of crack propagation when a crack comes to the end of a suitably oriented grain boundary. An additional incubation time is then required to nucleate a crack in the new grain boundary. In 7075, once a crack has begun to propagate it continues until the failure is complete. This periodic behavior of 2219 is a possible explanation for the stepwise scatter of the data of the SCC attenuation shown in Fig. D. 7. Another implication of the periodic behavior of this alloy is the definition of the SCC life. In the experiments of section C of the Fifth Quarterly, the time-to-failure for 2219 was taken as the time for the applied load to drop to 80% of its original value, rather than the time to complete failure.

#### F. Anisotropy of Rayleigh Wave Echoes from SCC

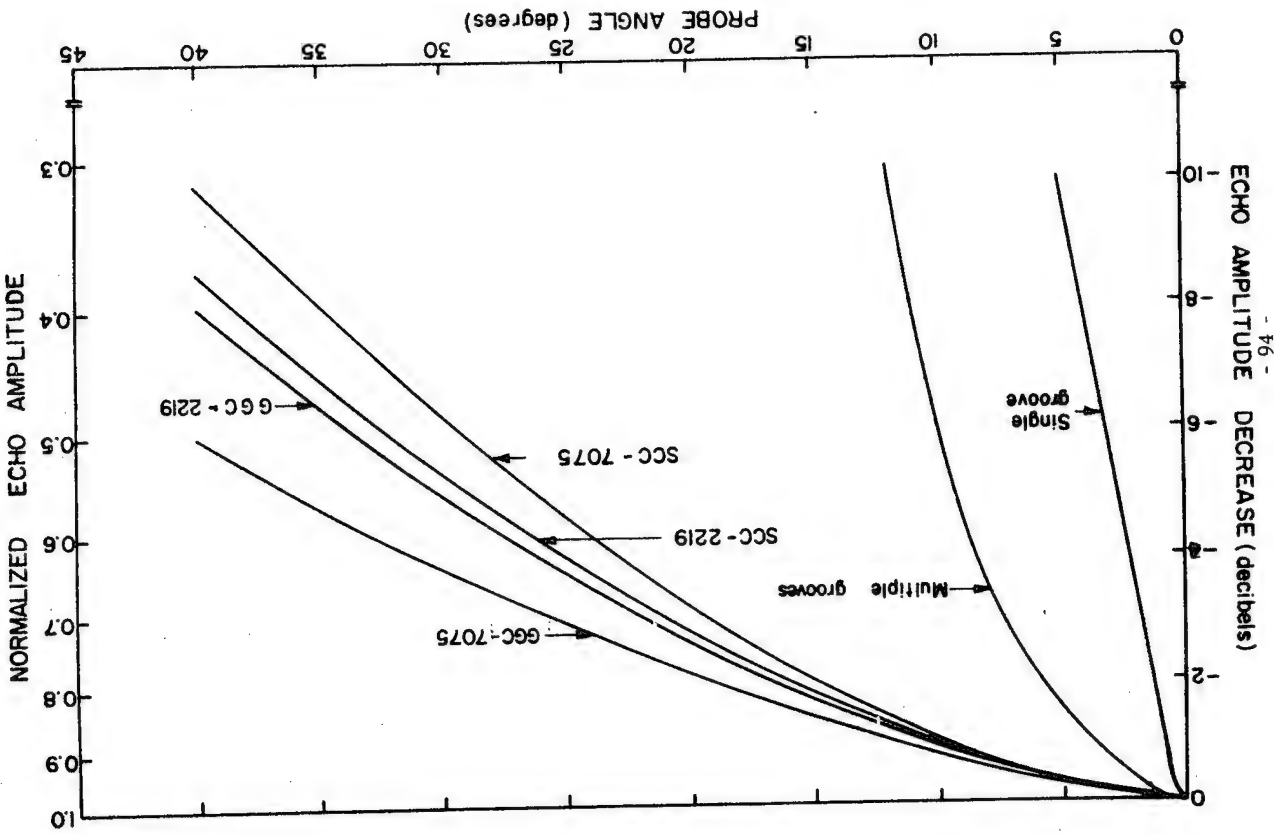
For the SCC study, a rectangular area on the U-bend tensile specimens at the bend was exposed to the corrosive environment, and the cracks that were formed were approximately perpendicular to the stress direction. Of course, the stress corrosion cracks themselves are not perfectly straight but make small angles and steps along the transverse direction.

In this investigation the anisotropy of reflections from stress corrosion cracks was studied as a function of the angular rotation of the probe. This measures the sensitivity of the Rayleigh waves to defects on a corroded area not perpendicular to the ultrasonic beam. In the final quarter, the investigation was completed. The tests included both 7075 and 2219 alloys, SCC and GGC, stressed and un-stressed states, 60% and 90% of the yield strength stress levels, and different amounts of exposure in the corrosive environment. The maximum angular rotation the U-bend specimens allowed was about 40°. Figure D.11 shows the results. The amplitude of the highest echo originating from the corroded area was measured with respect to the corresponding echo at normal incidence; that is, the echo at normal incidence is taken as zero db and all other echoes were referenced to it.

Figure D.11 also includes the results for a single artificial, straight reflector and multiple short parallel grooves. The principal observations of this investigation and some appropriate explanations are listed below.

- (1) The scatter between points of different specimens is of the order of that observed between points of the same sample. Most of the data points are correct within 2 db.
- (2) SCC and GGC are detectable over wider angular limits than a set of multiple short parallel grooves or a single isolated groove.

Fig. D.11 Anisotropy of Rayleigh wave echoes from SCC, GGC, and artificial defects as a function of probe angle.



This, for the case of SCC, is possibly due to the fact that some cracks or segments of cracks make an angle with the transverse direction and are thus favorably oriented to the particular probe angle. Fortunately, this increases the angular sensitivity of the probe and makes possible the detection of stress corrosion cracks from wide angular limits. For the GGC case, the pits offer reflectors at all possible angles, and this, in principle, makes GGC easier to detect than SCC. However, SCC is almost always accompanied by plain corrosion. The best approximation of isolated SCC would be the short exposures of 2219 specimens where the GGC attack is minimum.

(3) GGC has a smaller variation of reflectivity with angle than SCC. The fact that there is any angular dependence of reflectivity with GGC probably arises through interaction of pit formation and the anisotropy of the aluminum produced by rolling in the fabrication process.

(4) The angular dependence is independent of the amount of corrosion of the specimens for both GGC and SCC.

(5) For the case of GGC, the relative reflectivity at any angle is less for 2219 than for 7075.

(6) The results did not depend on whether or not the specimens were stressed or unstressed during ultrasonic investigation.

(7) For SCC, the angular dependence of reflectivity was independent of the stress level (60% or 90% of the yield strength).

(8) The greater decrease in reflectivity for 7075 than for 2219 at a given angle was possibly due to the zig-zag nature of the 2219 stress corrosion cracks.

#### G. Reflectors and Detection of SCC in Finished Parts

In order to use Rayleigh waves for the detection of SCC, it is necessary either to observe reflections from the cracks or to measure the associated increase in attenuation. For reflection measurements, a transducer attached to the surface of the part is all that is necessary.

We have found that commercial "rubber" cement gives a reproducible bond with a high coupling coefficient. Variations of less than one or two db are generally obtained. We can take advantage of the ability of Rayleigh waves to propagate around rounded corners to detect cracks over a large area of surface. By making use of the different anisotropy of the reflection from SCC and GGC, it is possible to differentiate between SCC and the more general attack of GGC.

The determination of SCC damage by attenuation is slightly more complicated, but this method is more sensitive to SCC. As was discussed earlier, it is necessary that a known discontinuity be present to reflect part of the ultrasonic energy back to the transducer. The reflection coefficient of the discontinuity must be known. Several means of introducing an artificial reflector were tried, including liquids on the surface, a razor blade, and a brass block attached with rubber cement. Of these, the latter is by far the most reproducible and also gives the largest reflection coefficient. Preliminary studies of externally attached reflectors indicate that the reflectivity is strongly influenced by the coupling medium, but the amplitude of the return signal could be reproducible within two db. With this type of sensitivity, it is possible to detect SCC on one or two centimeters of materials. Since the surface wave passes over the corroded region twice, the sensitivity is twice as great. Of course, it is assumed that the attenuation per unit distance is known for the unaffected surface. Another possibility would be to use separate sending and receiving transducers to measure the surface attenuation. Since Rayleigh waves are not extremely sensitive to surface finish, compared with SCC effects, it appears that this technique of measuring surface attenuation is very promising for routine detection of SCC damage.

However, the reproducible coupling of reflectors and transducers to sample surfaces must be studied further, along with the effects of coupling medium, coupling pressure, and the state of the sample surface to be examined.

### III. INVESTIGATION OF SIMULATED DEFECTS WITH SURFACE RAYLEIGH WAVES

When surface defects occur in the path of propagation of Rayleigh surface waves, a scattered Rayleigh wave is produced, as well as bulk waves (longitudinal and shear) which propagate into the medium. One result of this scattering is the attenuation of the main Rayleigh wave beam.

To determine the effect of surface defects on the propagation of Rayleigh waves, real defects such as cracks and pits may be approximated as isolated artificial defects of known geometry. Cracks are simulated by grooves, and pits by semispherical indentations or cylindrical holes with their axes perpendicular to the surface. The results of the investigation with simulated defects, for which the measuring frequency was 4 MHz, are presented in the following paragraphs.

(1) The reflectivity from a single artificial groove increases with increasing depth until it approaches a limiting value at a depth of about one wavelength (27 mils or 0.7 mm at 4 MHz). Total reflection was not observed even for grooves which were several wavelengths deep (Fig. D. 12).

(2) The Rayleigh wave reflection coefficient is proportional to  $\exp [-\alpha \lambda / D]$  where D is depth of the groove, and  $\alpha \sim 0.5$  (Fig. D. 13). Grooves as shallow as 20 microns can be detected at a probe distance of about 7 cm and on a surface finish as rough as that produced by a 240-grit paper.

(3) Angular rotation of the probe from normal incidence sharply decreased the echo amplitude from a groove or parallel grooves. For example, an echo decreases to half its normal incidence value at an angle of 3°. (Fig. D. 11).

(4) Multiple parallel, short grooves give an angular distribution in between the SCC case and single groove case (Fig. D. 11).

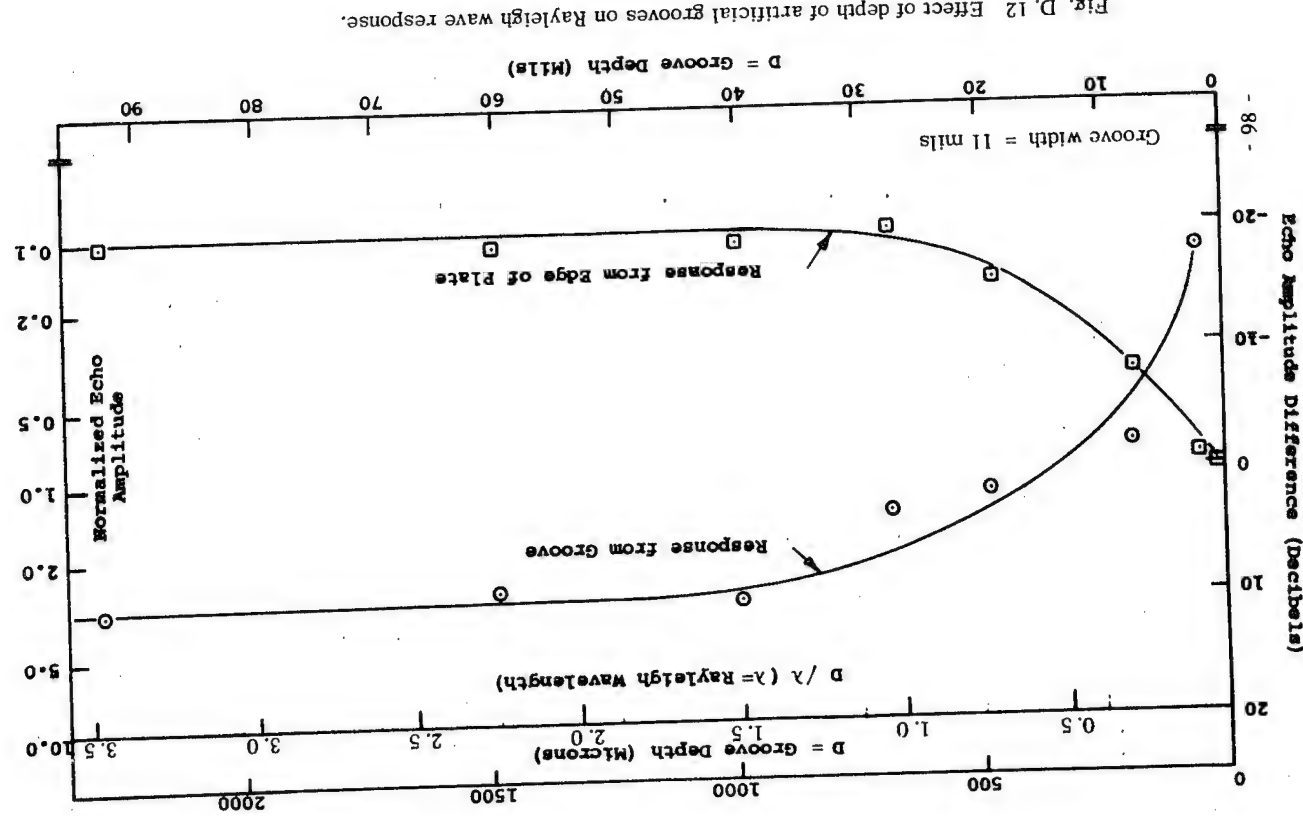


Fig. D. 12 Effect of depth of artificial grooves on Rayleigh wave response.

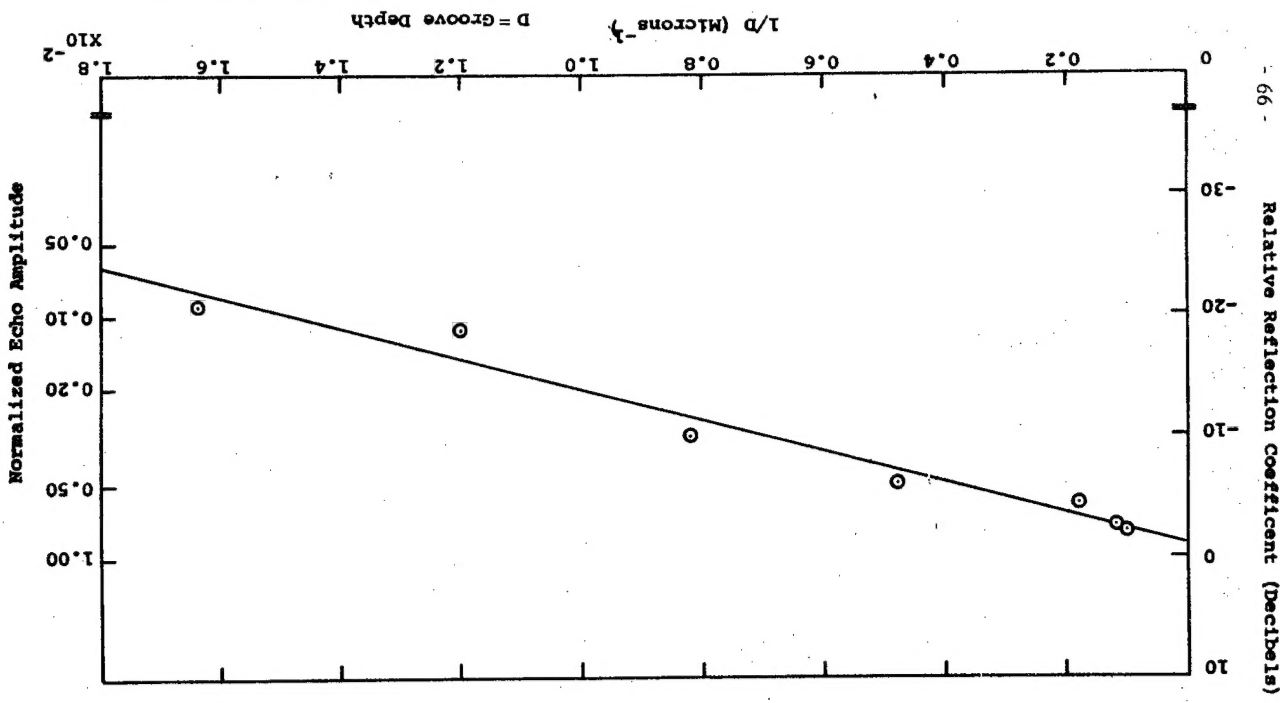
(5) A defect that does not intercept the surface can readily be detectable at an effective depth below the surface of one wavelength or less. Figure D.14 shows how the tests were performed and the results.

(6) The reflectivity from cylindrical holes with axes perpendicular to the surface increases with increasing hole diameter to about 175 mils or 7 wavelengths, after which it becomes constant (Fig. D.15). Also, the reflectivity from cylindrical holes increases with increasing hole depth to 40 mils or 1.5 wavelengths. Deeper than 40 mils, the echo remains roughly constant (Fig. D.16).

(7) The reflection coefficient of a sharp corner decreases with increasing angle between the two planes from 90° to 180° where there are no reflections at all (Fig. D.17). These investigations were made on "sharp" edges. Of course, by rounding them the reflection coefficient would be drastically reduced.

Summarizing, we can say that if the dimension of a defect is of the order of a few tenths of a wavelength, reflections are readily visible along with an effective increase in attenuation. Defects located deeper below the surface than one wavelength are not detectable. The most general conclusion that can be drawn is that Rayleigh waves are very sensitive to defects, but only in surface layers not more than one or two wavelengths thick.

Fig. D.13 Reflection of Rayleigh waves from a groove as a function of the reciprocal of the depth.



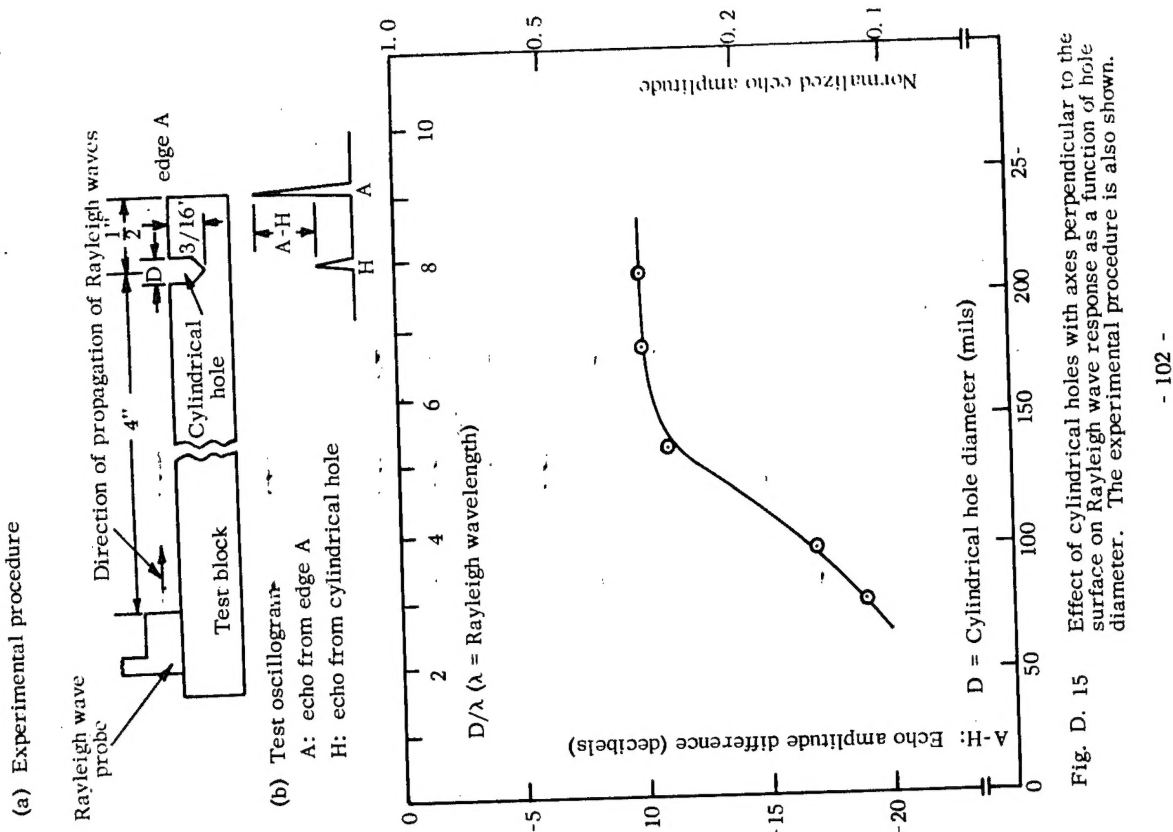
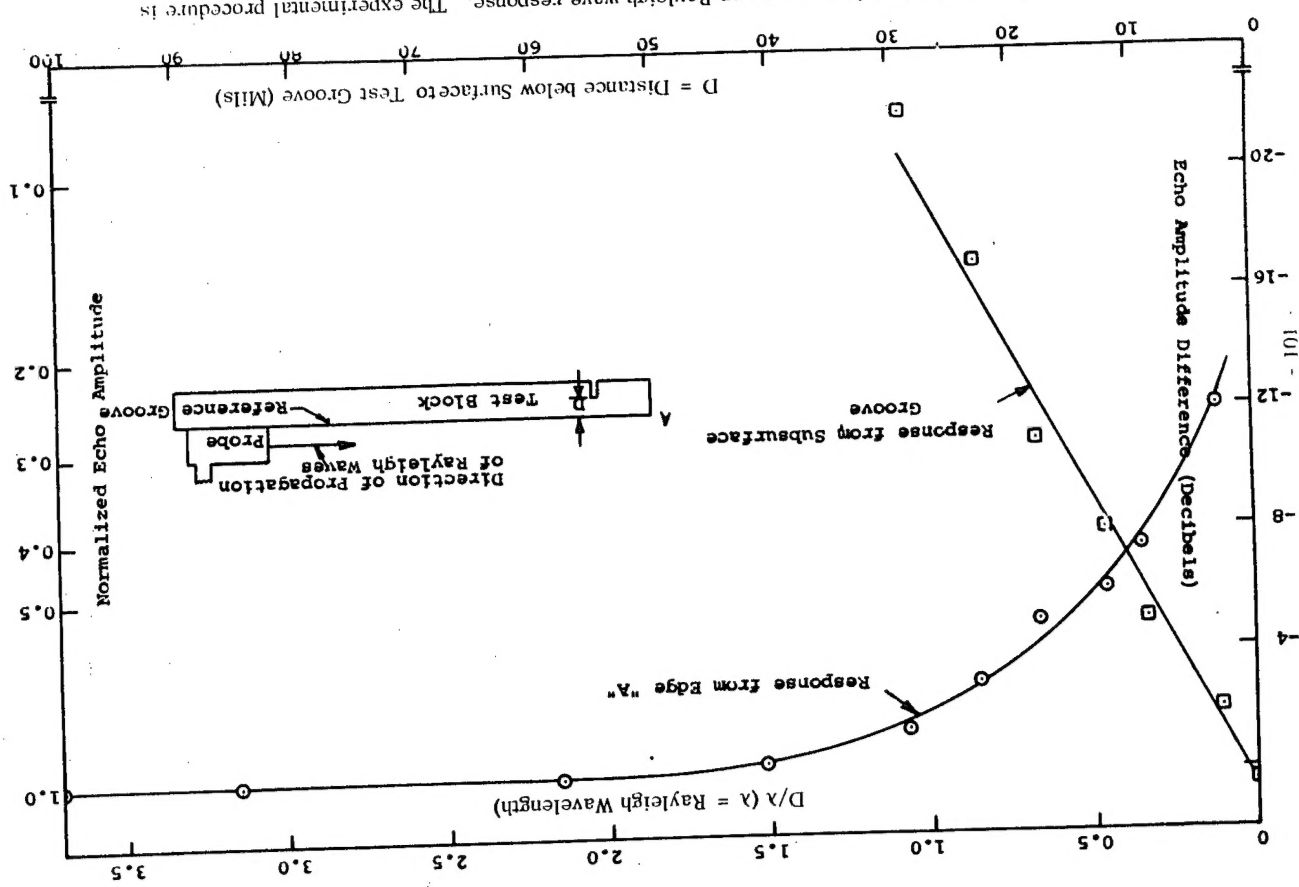


Fig. D. 15 Effect of cylindrical holes with axes perpendicular to the surface on Rayleigh wave response as a function of hole diameter. The experimental procedure is also shown.



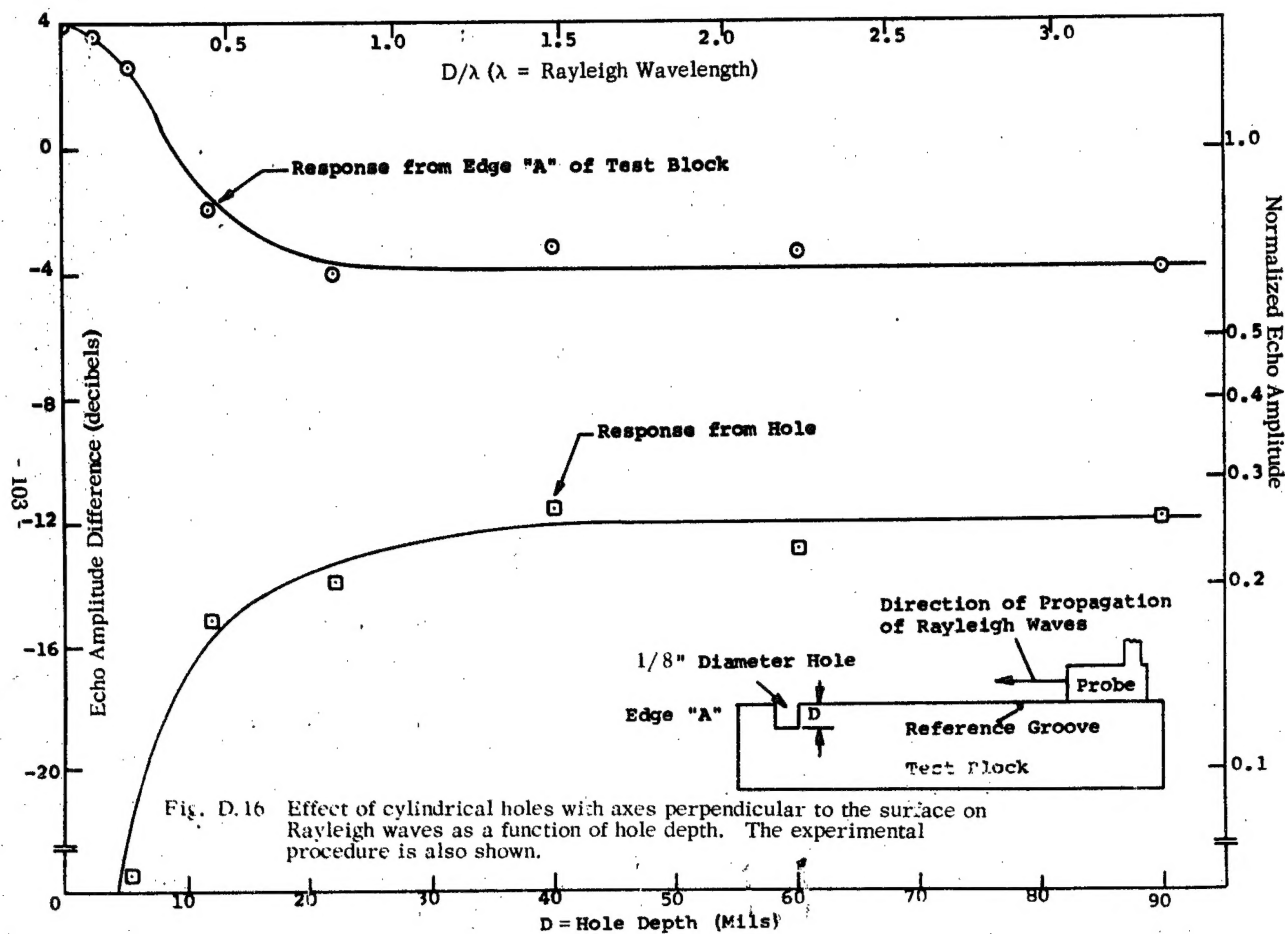


Fig. D.16 Effect of cylindrical holes with axes perpendicular to the surface on Rayleigh waves as a function of hole depth. The experimental procedure is also shown.

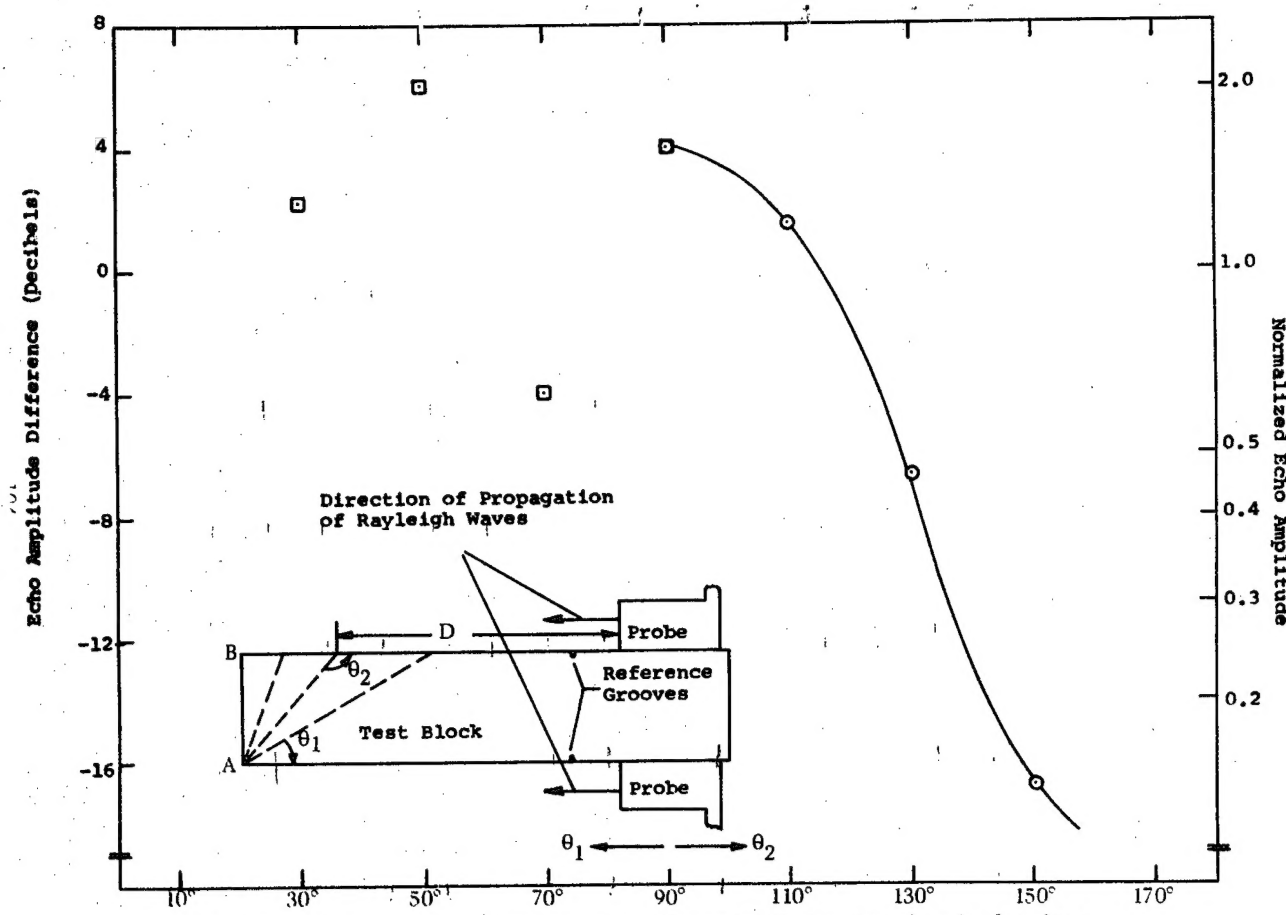


Fig. D.17 Effect of edge angle on Rayleigh waves. The experimental procedure is also shown.

#### IV. SUMMARY

Since all of this report is in the nature of a summary, only the principal observations will be indicated here.

- (1) Initially, SCC is detected ultrasonically in 7075(T651) after approximately a  $0.2 \text{ coul/cm}^2$  incubation period at 90% and 60% of the yield strength. In 2219(T37) under similar conditions, there is little if any incubation period for the detection of cracking. The ultrasonic threshold is determined by the reflections from grain boundaries.
- (2) The ultrasonic attenuation and reflectivity is substantially greater for SCC after a given amount of corrosion than for GGC samples, even after the stress has been released. The attenuation is much larger (a factor of 4 or 5 for the 90% level) in the stressed state compared with the unstressed state.
- (3) After onset of SCC, the attenuation increases approximately linearly with further corrosion for 2219 and 7075 both in the stressed and unstressed cases and also for the 60% and 90% stress levels. The increase in attenuation in 2219 is not as smooth as 7075. This is probably related to the more zig-zag nature of cracks in 2219.
- (4) The reflectivity from SCC is anisotropic with the largest coefficient in a direction parallel to the stress (i. e. perpendicular to the cracking). GGC also exhibits some anisotropy.
- (5) SCC can be detected either by observing reflections from the cracked area or measuring the associated attenuation. Either technique would be useful for examination of finished parts.
- (6) Rayleigh waves are sensitive to detect defects of the order of few tenths of a wavelength in size and located not more than one or two wavelengths below the surface. Artificial defects of known geometry, such as grooves and cylindrical holes, have been used to show this.